

Scale Prediction of Crush Rock Shovel Pad Stability

by

Enjia Shi

A thesis submitted in partial fulfillment of the requirements for the degree of

Master of Science

in

Mining Engineering

Department of Civil and Environmental Engineering

University of Alberta

© Enjia Shi, 2015

Abstract

Adverse mining equipment motions give rise to ground deterioration and poor ground conditions will in turn aggravate equipment structural damage as a result of enhanced detrimental motions of the equipment. Costs for correcting equipment fatigue failures are tremendous. Consideration of a suitable mining or operating surface material to improve ground conditions through knowledge of material performance under equipment cyclic loading leads to better mine operating surface designs, lower maintenance costs and more reasonable operational strategies.

In investigating the performance of crushed limestone as a potential enhancing ground material under shovel tracks during shovel duty cycles, a shovel-ground equilibrium has been analysed to determine ground pressures under shovel tracks. Cyclic plate load tests were conducted to develop an overall view of crushed limestone behavior under cyclic loading. A relationship between pressure stiffness and plate shape was discerned with respect to initial loading, which provides a reference for tracked-equipment manufactures for track design. For cyclic loading conditions during excavating operations, resilient stiffness was shown to be consistent with the stress-deformation response displayed by the more conventional CBR test. Therefore, CBR may be applied to approximate the

resilient stiffness of crushed limestone. A correlation between total deformation and the number of cycles was established for different plate aspect ratios and stress levels.

The last stage of this study combined the shovel loading cycles and material performance together to estimate the ground deformation as duty cycles increase to optimize a shovel operational duration in a single location.

The CBR test was performed to verify the applicability of the crushed limestone as a cap material in a multi-layer haul road on weak in-situ material.

Acknowledgement

I would like to express my very great appreciation to my supervisor Dr. Joseph for his professional guidance and extraordinary support in this thesis process and throughout my study in University of Alberta. He is always willing to give his time, patience and valuable suggestions so generously to help me overcome difficulties. Without his persistent help the thesis would have been impossible.

I also wish to offer my special thanks to our technician Lucas Duerksen for helping me prepare the laboratory material and apparatus and for his technical assistance in running the test program.

I would like to thank the Hammerstone Corporation for providing limestone crush for the laboratory tests, and also thank the P&H Joy Global Inc. for offering the shovel field operational data for equilibrium analysis.

I would also like to extend my particular thanks to my friends Sujith Sundararajan, Zhihan Lin, Chaoshi Hu, Enzu Zheng, Ebrahim Azimi and all office mates for help and company. I will treasure the precious friendship with them forever.

I acknowledge the financial support provided by NSERC and the University of Alberta. I offer my thanks to the Department of Civil and Environmental Engineering for employing me at research/teaching assistant positions during my graduate studies.

Finally, I wish to thank my parents for their support and encouragement throughout my life.

Table of Contents

Abstract	ii
Acknowledgement	iv
List of Figures	viii
List of Tables	xiii
1 Introduction.....	1
1.1 Statement of the problem	1
1.2 Objective and Scope of the study.....	2
1.3 Methodology and Context.....	3
2 Literature Review.....	6
2.1 Shovel performance and causes of cyclic loading.....	6
2.2 Material performance under cyclic loading.....	9
2.2.1 Rock	10
2.2.2 Sand.....	12
2.2.3 Other soils	15
2.2.4 Crushed rock with fines	18
2.3 Two methods in haul road design	23
2.3.1 Boussinesq Method.....	24
2.3.2 California Bearing Ratio (CBR)	28
3 Shovel equilibrium and Ground pressure	32
3.1 Shovel equilibrium	32

3.1.1	Equilibrium of hoist and crowd system	35
3.1.2	Equilibrium of dipper and digging-face system.....	36
3.2	Ground pressure	38
3.3	Results	41
4	California Bearing Ratio (CBR) Test	45
4.1	Apparatus and Procedure	45
4.2	Results	46
4.3	Haul road design.....	48
5	Cyclic Plate Load Tests	53
5.1	Specimens.....	53
5.2	Scaling	54
5.3	Apparatus	55
5.3.1	MTS	55
5.3.2	Box	56
5.3.3	Plates dimensions.....	57
5.4	Set up and Procedure.....	58
5.5	Results	59
6	Discussion.....	64
6.1	Initial loading	64
6.2	Cyclic loading	67
6.2.1	Stress-deformation response	67
6.2.2	Deformation	73

6.2.3	FLAC3D Simulation.....	78
6.3	Material surface conditions after loading cycles.....	85
6.4	Application to shovel loading conditions.....	86
7	Conclusion	90
7.1	Results summary	90
7.2	Contributions to knowledge and industry	92
8	Future work.....	94
	References.....	95
	<i>Appendix I-Geometric approach for shovel hoist and crowd system equilibrium</i>	101
	<i>Appendix II-Geometric approach for the shovel dipper and digging-face system equilibrium</i>	105
	<i>Appendix III-Matlab code for Figure 3-11</i>	106
	<i>Appendix IV-Matlab code for Figure 3-13</i>	108
	<i>Appendix V-Matlab code for data screening in cyclic plate load tests</i>	110
	<i>Appendix VI-Estimation of coefficients in Equation (6-2) and confidence intervals in Matlab</i>	111
	<i>Appendix VII-FLAC 3D language for simulation</i>	112
	<i>Appendix VIII-Matlab code for Figure 6-24</i>	113

List of Figures

Figure 1-1 Research methodology and process flow chart.....	5
Figure 2-1 Cable shovel power draw of hoist and swing motor one duty cycle (after Joseph & Hansen, 2002).....	7
Figure 2-2 Ground pressure under shovel for one entire duty cycle (after Sharif-Abadi & Joseph, 2010)	8
Figure 2-3 Simplified dipper-handle free body diagram (after Shi, 2007).....	9
Figure 2-4 Post-peak stress-strain curve with confining stress (after Joseph et al., 2003).....	10
Figure 2-5 Modulus with increasing number of cycles for a given confinement stress σ_3 (after Joseph et al., 2003)	11
Figure 2-6 Composition of pseudo-elastic deformation during post-peak unload-reload (after Joseph et al., 2003).....	12
Figure 2-7 Soil deformation process of plate sinkage tests for sandy loam (after Earl & Alexandrou, 2001).....	13
Figure 2-8 Schematic of a cyclic compaction test (after Sawicki & Swidzinski, 1995).....	13
Figure 2-9 Hyperbolic model of soil shear stress-strain curve	15
Figure 2-10 Skeleton curve and hysteresis relationship based on Masing's rule (after Ishihara, 1996).....	16
Figure 2-11 Three loading phases: initial loading, constant loading and cyclic loading (after Sharif-Abadi, 2006).....	18
Figure 2-12 Fines content in crushed stone (after Thom & Brown, 1988).....	19
Figure 2-13 Specimen Response during axial load-unload (after Brown, 1996)..	19

Figure 2-14 Unbound granular material stress-strain curve from cyclic tri-axial test (after Thompson & Brown, 1988).....	20
Figure 2-15 Simulation results (a) stress-strain curve (b) strain incurred for (a) (after Yohannes et al., 2014).....	23
Figure 2-16 Geometry of a rectangular area	25
Figure 2-17 Boussinesq bulb under a circle area (after Perloff, 1976).....	27
Figure 2-18 Boussinesq bulb under square and continuous area.....	27
Figure 2-19 Haul road categories (after Thompson & Visser, 1997)	29
Figure 2-20 Ultra-class truck USBM CBR design chart (after Thompson, 2011) 30	
Figure 2-21 Approximate CBR values of various soils types accommodate with AASHTO and Unified Soil Classification (USCS) (after Thompson, 2011)	31
Figure 3-1 A simplified schematic of mining cable shovel	32
Figure 3-2 Free body diagram of a simplified shovel dipper system.....	34
Figure 3-3 Moment of hoist force within one digging duty cycle	36
Figure 3-4 Moment of handle weight within one digging duty cycle.....	36
Figure 3-5 Shovel digging trajectory from field data	37
Figure 3-6 Moment of resistance from digging-face	38
Figure 3-7 Schematic of shovel track side view	39
Figure 3-8 Schematic of triangular distribution.....	40
Figure 3-9 Schematic of trapezoidal distribution.....	40
Figure 3-10 Digging trajectory with eight critical positions.....	42
Figure 3-11 Ground pressure distribution along the shovel track for eight critical positions (units kPa).....	43
Figure 3-12 Shovel track allocation	43
Figure 3-13 Pressure versus time for 6 specific track portions during excavating	44
Figure 4-1 Crushed limestone used in laboratory tests.....	45

Figure 4-2 CBR loading apparatus	46
Figure 4-3 Vertical stress-deformation curve from limestone CBR test	48
Figure 4-4 Multiple-layer haul road overview	48
Figure 4-5 Stress versus depth below load footprint	50
Figure 5-1 Size distribution curve for the limestone material	54
Figure 5-2 Diagram of MTS	56
Figure 5-3 Configuration of steel box.....	57
Figure 5-4 Force versus time during ramp-up, hold and 4 cycles for plate 3 at 800 kPa and 0.016 Hz	59
Figure 5-5 F-D curve for plate 3 at 800 kPa and 0.016 Hz.....	60
Figure 5-6 F-D curve for the first few cycles.....	61
Figure 5-7 F-D curve for the last few cycles	62
Figure 5-8 D-T curve of plate 3 for 800 kPa and 250 cycles.....	63
Figure 5-9 D-T curve of Figure 5-8 after screening points.....	63
Figure 6-1 Force-deformation curve for plate 3 under 200, 400, 600, 800 kPa cyclic load	65
Figure 6-2 Force-deformation curve for plate 2 under 200, 400, 600, 800 kPa cyclic load	65
Figure 6-3 Force-deformation curve for plate 1 under 200, 400, 600, 800 kPa cyclic load	66
Figure 6-4 Pressure stiffness versus width over length ratio for three plates displayed as a function of loading rate.....	67
Figure 6-5 Global stiffness versus number of cycles for plate 2 at 200, 400, 600 and 800 kPa and 0.016 Hz frequency	69
Figure 6-6 Global stiffness versus number of cycles for 4 load levels and 3 frequencies of plate 2	70

Figure 6-7 Stress-deformation curve approximated by resilient stiffness at different load level	72
Figure 6-8 Deformation versus number of cycles for plate 3, 0.066 Hz under different load levels.....	73
Figure 6-9 Deformation versus number of cycles for plate 3, 800 kPa at different frequencies	74
Figure 6-10 Plastic deformation per cycle versus number of cycles for plate 1 at different load and frequency conditions within an envelope of response.....	75
Figure 6-11 Deformation versus number of cycles for plate 3	76
Figure 6-12 Deformation versus number of cycles for plate 2	77
Figure 6-13 Deformation versus number of cycles for plate 1	77
Figure 6-14 System profile in FLAC3D for plate 3 under 800 kPa.....	80
Figure 6-15 Maximum unbalance force history in FLAC3D for plate 3 under 800 kPa.....	81
Figure 6-16 Contours of vertical stress distribution under plate load.....	82
Figure 6-17 Contours of Confining stress.....	83
Figure 6-18 Contours of Z-displacement	83
Figure 6-19 Contours of X-displacement magnitude.....	84
Figure 6-20 Contours of Y-displacement magnitude.....	84
Figure 6-21 Material surface condition after cyclic loading by strip plate.....	85
Figure 6-22 Particle breakage after unload-reload.....	86
Figure 6-23 Determination of pressure stiffness during initial loading for shovel track.....	87
Figure 6-24 Ground deformation under shovel track with increasing number of cycles.....	89
Figure 1 Geometric schematic of shovel hoist system (after Lin, 2014)	101

Figure 2 Geometric schematic of shovel boom system (after Lin, 2014)..... 103

Figure 3 Geometric schematic of shovel bucket and digging-face system (after Lin, 2014) 105

List of Tables

Table 3-1 Nomenclature in shovel balance analysis.....	33
Table 3-2 Dimensions and weights for P&H 4100C BOSS mining shovel.....	33
Table 3-3 Nomenclature in dipper system balance analysis	34
Table 3-4 Example of results for hoist and crowd system.....	35
Table 3-5 Example of results for dipper and digging-face system	38
Table 3-6 Example of calculated ground pressure.....	41
Table 4-1 Results of limestone CBR test.....	47
Table 4-2 Vertical stress with depth influence under long footing area	49
Table 4-3 Values of the critical parameters in the haul road construction design	51
Table 5-1 Plates dimensions for cyclic plate load tests	57
Table 6-1 Pressure stiffness and width over length ratio of three plates	66
Table 6-2 Filtered data series during cyclic loading.....	68
Table 6-3 Resilient stiffness determination for three plates	71
Table 6-4 Load condition of six track portions during one shovel digging cycle	86
Table 6-5 Values of parameters and coefficients in determining total deformation of ground under a shovel track.....	88
Table 1 P&H 4100C BOSS mining shovel specification (1).....	102
Table 2 P&H 4100C BOSS mining shovel specification (2).....	103

1 Introduction

1.1 Statement of the problem

The purchase of an ultra-class mining equipment such as P&H 4100C BOSS shovel with gross vehicle weight (GVW) of over 1500 tonnes requires a major investment of about \$40 million for an open pit mining operation. However, the structural life of large mobile equipment is usually half that expected as a result of ground stability issues. High maintenance costs from components' fatigue failure dominate daily operational and maintenance expenses.

Circumstances are especially severe in Northern Alberta where surface mining operations are extreme due to harsh ground conditions due to climate and geological characteristics. In summer oil sand ground conditions will become as soft as clay after a few cycles, where ground will become undulating and result in high rolling resistances for trucks (Joseph, Sharif-Abadi & Shi, 2003). Conversely in winter oil sand is very firm over soft material. Cyclic motion of equipment will have an adverse impact on ground stability which will in turn lead to machine structural damage. Establishing and /or constructing a suitable bearing surface for mining equipment operation is essential to sustaining the longevity of mining equipment. This thesis investigates the response of such a constructed bearing "pad" surface made of limestone crushed material.

For the above situation, adding stabilizing material on top of oil sand may improve soil conditions. Crushed limestone, with a consistent and reliable supply in the Athabasca region for more than 50 years, has unique properties of a stabilizing material. A global view of crushed limestone behavior under cyclic

loading and bearing strength (via the California Bearing Ratio, CBR value) has been developed in this thesis to evaluate the applicability of crushed limestone as a stabilizing ground material under shovel tracks and as a cap for a multi-layer haul road on weak in-situ base. This has the potential of improving mining operating surface designs and provides for a ground maintenance strategy to enhance shovel digging operational guidelines.

1.2 Objective and Scope of the study

The objective of this study is to (1) investigate the performance of crushed limestone as a ground material under cyclic loading by a shovel track systems in addition to (2) predict the ground deformation beneath a shovel track after several duty cycles with respect to a) the stability of equipment and b) structural damage, and to (3) verify limestone serving as a cap material of a multi-layer haul road on a weak in-situ base.

The research analysis performed here for shovel balance and pressure distribution under a shovel track is performed through a knowledge of machine geometry and mechanics. A full shovel duty cycle is normally evaluated including dipper-face interactions when a dipper excavates an ore face and shovel-truck interactions when the shovel swings to dump. In this thesis, only the dipper-face interactions are considered. Field data has been utilized to estimate ground pressure distribution via P&H 4100C BOSS on-board power usage measurement systems. Other parameters related to the shovel specification were learned from the manufacture's P&H 4100C BOSS specification sheets.

For a better understanding of crushed limestone behavior, the CBR test and cyclic plate load tests were conducted. The material used in the laboratory tests was

evaluated under dry conditions. Course material is usually free drained. If it doesn't retain water, the sole impact of water would be to lower the effective strength via frictional resistance between particles. To simplify the analysis performed here, the influence of water content was excluded from this research.

1.3 Methodology and Context

This thesis concentrates on the response of crushed limestone due to cyclic loading via shovel face excavating activities. In the literature review, shovel digging activity and the impact of cyclic loading are reviewed. This is followed by the description of the limestone and other material properties (not only crushed limestone but also overburden rock, sand, oil sand and clay) under unload-reload conditions. Two methods commonly applied for haul road design are studied in Chapter 2.

In chapter 5, cyclic plate load tests devised for the purpose of this work were used to mimic shovel track motions while loading broken limestone. Experimental parameters such as cyclic load level, frequency and plate dimensions were determined at an appropriate scale. Force and moment equilibrium equations were established via geometric and weight relationships related to the shovel body and dipper system explored in Chapter 3 to estimate the ground reaction forces and pressure distribution along a shovel track, providing the essential parameters for the scale cyclic tests.

California Bearing Ratio tests on crushed limestone have been performed in Chapter 4. Based on the discussed CBR values and using a mechanistic approach after the work of Thompson, assessment of limestone as a haul road construction material has been made.

In order to obtain broken limestone performance under cyclic loading conditions and the influencing factors, three plates of different dimensions were subjected to

four cyclic loads at three frequencies. The plate shapes are variations on shovel track pad-ground contact surface. The experiment details and results are present in chapter 5.

Results from the cyclic plate load tests are discussed in Chapter 6. Relationships between deformation, stress variation, frequency, number of cycles and plate shape are established. The slope of the stress-deformation curve in cyclic loading phase is compared with that of the conventional CBR test to build a correlation. FLAC3D has been applied to model the stress and deformation distribution in the target material using pseudo-elastic model. By visual inspection, the tests showed the flow of the particles, which has been verified by FLAC 3D simulation. A combination of shovel loading field data scaled to a laboratory test level and broken limestone performance under cyclic loading measured in the lab allows an estimation of ground deformation development with increasing number of duty cycles to be discerned using Matlab.

Chapter 7 and 8 provide the conclusions of the research and suggestions for future work.

An overview of the research methodology in a process flow chart is illustrated in Figure 1-1 .

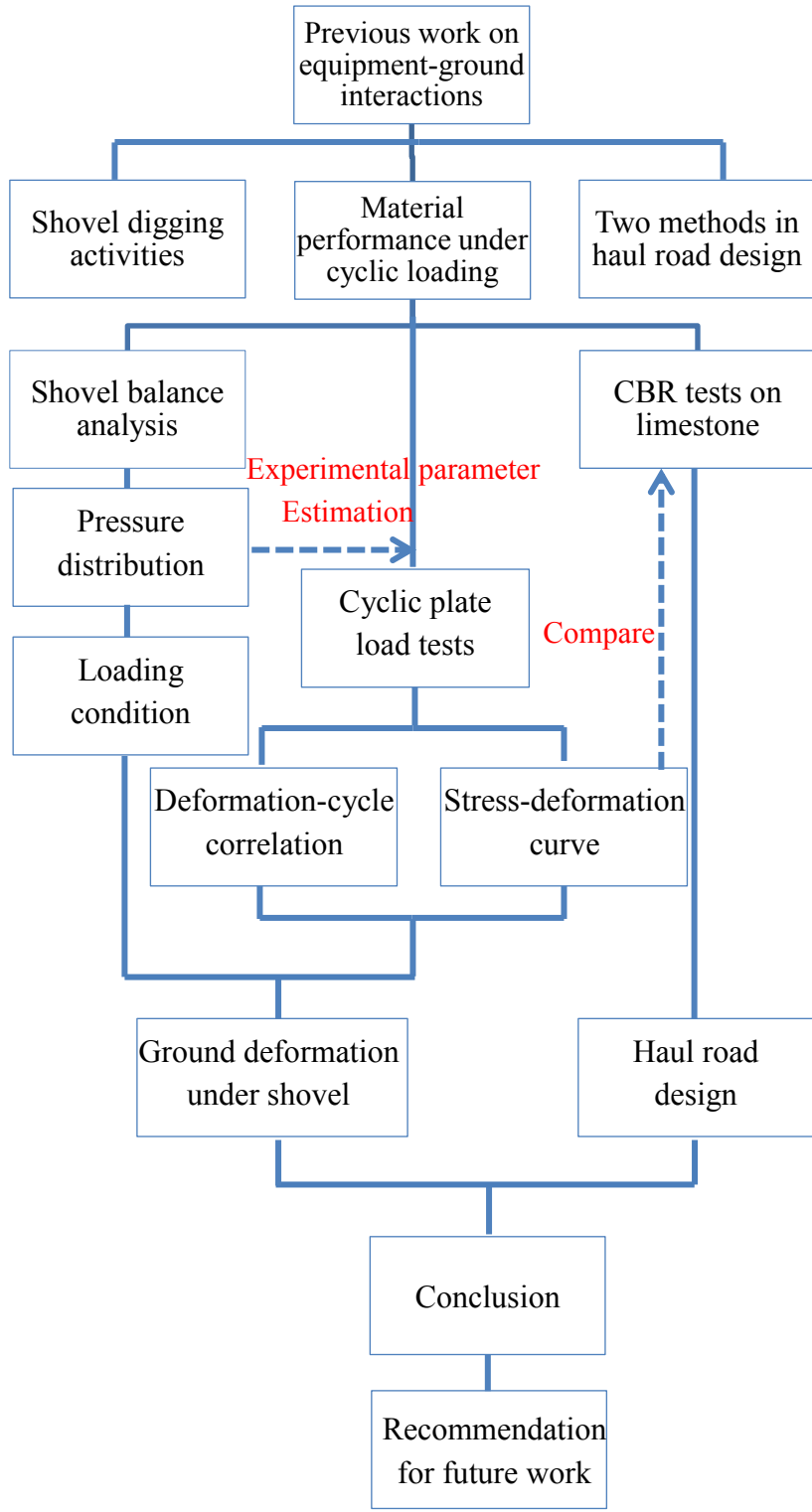


Figure 1-1 Research methodology and process flow chart

2 Literature Review

With a shovel rocking back and forth during face loading activity, the ground under a shovel track is subject to cyclic loading up to 120 psi (Joseph, 2002). In poor ground conditions, after a few cycles, the ground will become undulated and result in equipment instability (Joseph, Sharif-Abadi & Shi, 2003). In this chapter, shovel performance during face activity and the causes of cyclic loading are reviewed. In an attempt to understand the behavior of the target pad construction material (crushed limestone) under cyclic loading, the response of materials including overburden rock, sand, oil sand, clay and crushed limestone to unload-reload activities are reviewed. Crushed limestone is extensively used as a cap in the road construction. This chapter also covers two essential approaches to current haul road design.

2.1 Shovel performance and causes of cyclic loading

Focusing on detecting cable (“rope”) shovel operating activity, there are nine idealized key positions for the dipper (bucket) during a duty cycle including:

1. Tucked and engaging the face (just about to dig)
2. Half face height digging
3. Full face height digging
4. Full face height extracted
5. Swinging to dump at a diagonal corner position
6. Raised and full over the waiting haul truck
7. Raised and empty over the waiting haul truck having dumped a load
8. Empty swing back of diagonal corner position
9. Half face empty

Cable shovel power draw from hoist and swing motors for one duty cycle is illustrated in Figure 2-1. The time period of one duty cycle differs from 30 to 45 seconds. That is to say the frequency is about 0.033 Hz ~ 0.022 Hz. With respect to the digging portion of the duty cycle, the corresponding time and frequency are 15 s and 0.066 Hz respectively.

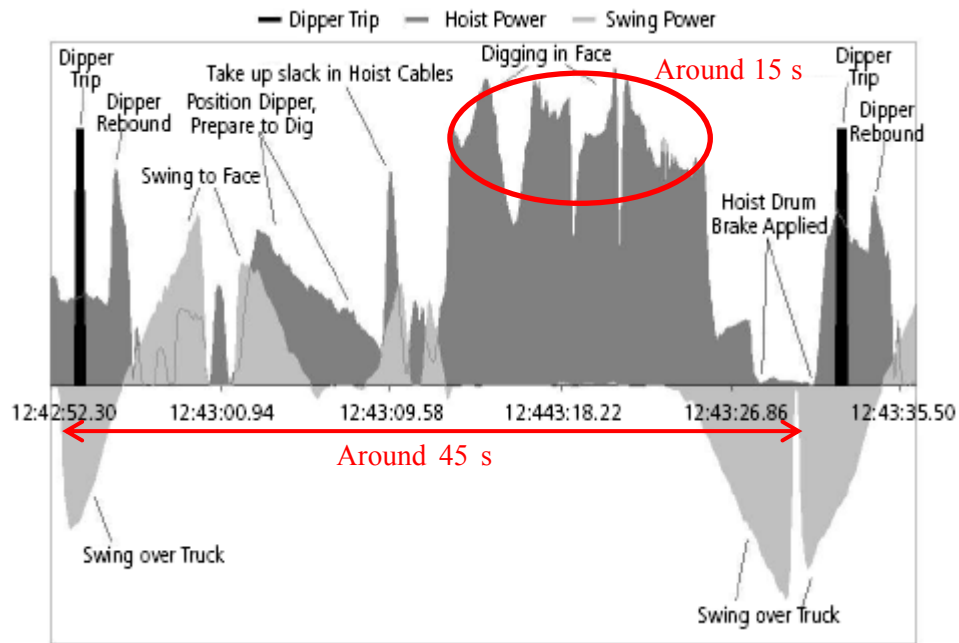


Figure 2-1 Cable shovel power draw of hoist and swing motor one duty cycle (after Joseph & Hansen, 2002)

Large mobile mining trucks (hauler) typically have 327 tonnes capacity and shovels have 45 cubic meter dipper capacity (1500 tonnes GVW for P&H 4100C BOSS shovel). Such units often have a structural life less than half that expected; Wohlgemuth (1997), Joseph (2001), Trombley (2001) and Joseph (2003) proposed three critical motions causing adverse impacts on trucks and shovels also causing unstable hazard and cyclic loading to the ground. Only rack represents the dominant cause of equipment structural failure. These are defined as

$$Rack = \{(LF + RR) - (RF + LR)\} \quad (2-1)$$

$$Pitch = \{(LF + RF) - (RR + LR)\} \quad (2-2)$$

$$Roll = \{(LF + LR) - (RF + RR)\} \quad (2-3)$$

where LF, RF, RR and LR are the left front, right front, right rear and left rear suspension (truck) or track-ground contact zone (shovel) loads respectively. Such loads may be evaluated in force or g-level units.

Sharif-Abadi & Joseph (2010) measured the ground pressure at the front and rear track portion of a shovel using plate pressure transducer and passive seismic instrumentation leading to the three idealized duty cycles (Figure 2-2). Numbers 1 to 9 on the x axis represent the nine key positions for the dipper.

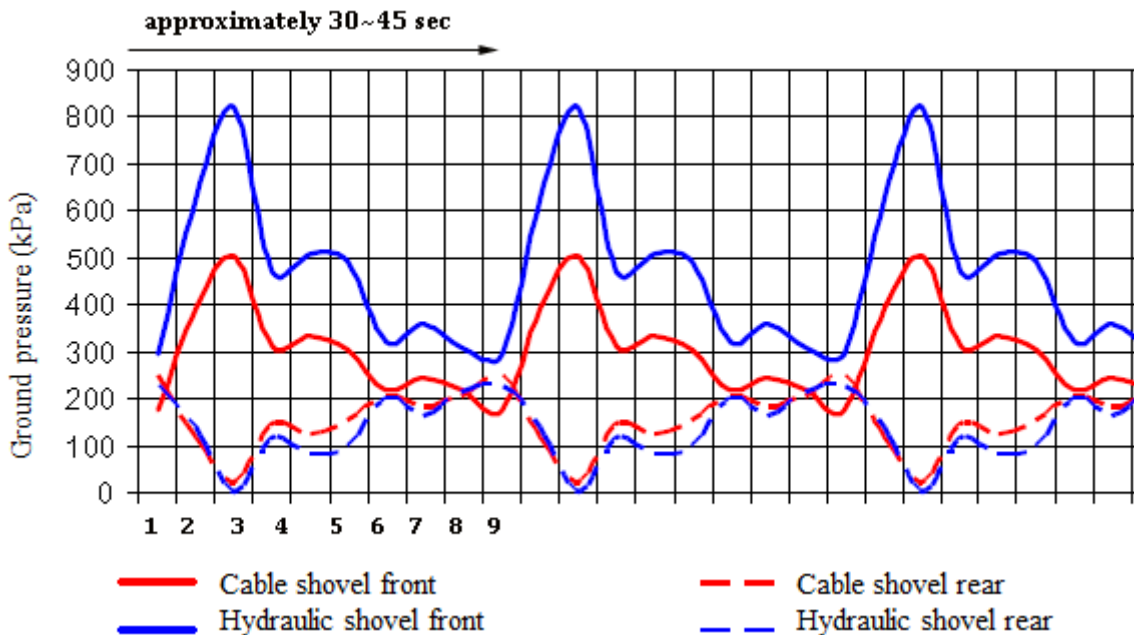


Figure 2-2 Ground pressure under shovel for one entire duty cycle (after Sharif-Abadi & Joseph, 2010)

In the field, ground reactions underneath dynamic shovel actually are very difficult to measure due to safety concerns. The ground pressure is also affected

by many factors such as properties of the digging material, volume and trajectory, digging velocity and machine condition. This research is primarily concerned with the ground material properties. A cable shovel on-board system power data download from the field was used to calculate the actual digging forces and reaction and resolved to give the ground pressures. Using a knowledge of machine geometry and mechanics equilibria, the ground pressure under the shovel track was determined. The most difficult evaluation is the digging resistance at the excavating face. Shi (2007) simplified a dipper-face interaction system as shown in Figure 2-3. This model only includes the hoist force F_h , crowd force F_l , handle support force F_s , gravity G , and digging resistance R . The geometric relations will be discussed in later chapters.

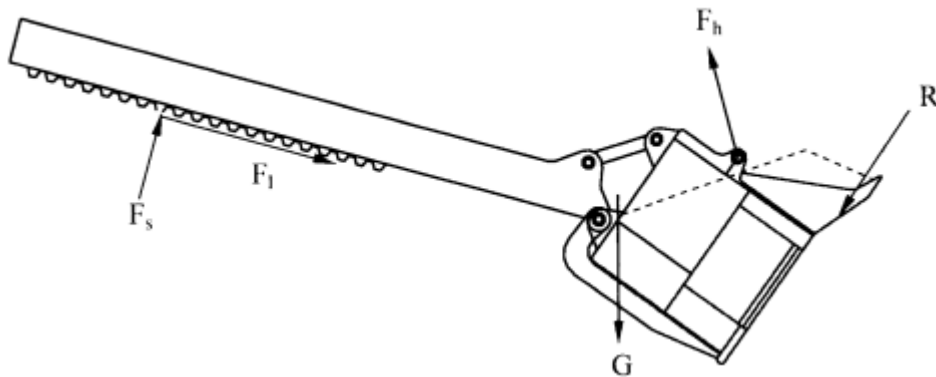


Figure 2-3 Simplified dipper-handle free body diagram (after Shi, 2007)

2.2 Material performance under cyclic loading

The material discussed in the thesis is one of unconsolidated limestone fragments including fines. Generally, soil can be classified into gravel, sand, silt and clay via the Unified Soil Classification System (USCS) by texture and grain size. The limestone crush material is more akin to gravel. The tests and analytical methods used to investigate the properties of crushed limestone are somewhat unique. Although this project doesn't deal with intact rock or finer soil, properties of such

materials under cyclic loading are well known and reviewed here for a better understanding of the chosen limestone crush material they span through comparison and contrast.

2.2.1 Rock

The elastic properties of intact rock are defined by an elastic modulus, E , (Young's Modulus) and Poisson's ratio ν . The elastic modulus can be obtained from the slope of the stress-strain curve from tri-axial compression tests. However there is no obvious linear portion on the curve for broken rock. Joseph et al. (2003) studied post-peak stress-strain curves for intact and broken rock and found that they follow the same trend at any given confinement (Joseph & Barron, 2003). Thus, intact rock can be used to predict post-peak behavior commensurate with the same broken rock. Figure 2-4 depicts the post-peak slope, E_{pp} of the post-failure stress-strain curve for rock with various confining stress, where the post-peak region represents broken or crushed rock.

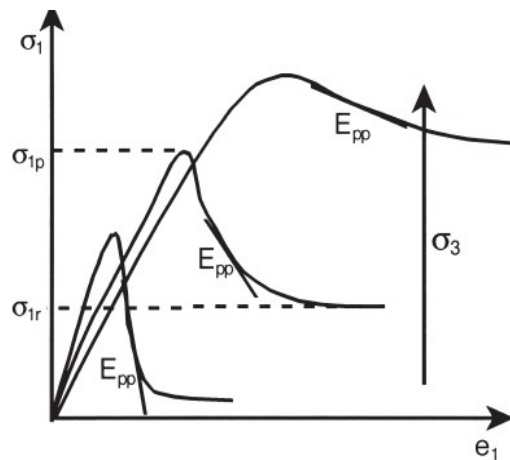


Figure 2-4 Post-peak stress-strain curve with confining stress (after Joseph et al., 2003)

For wider application, E_{pp} is replaced by a pseudo-elastic modulus (E_{ps}) as shown in Figure 2-5, which may be used more readily with current modeling software.

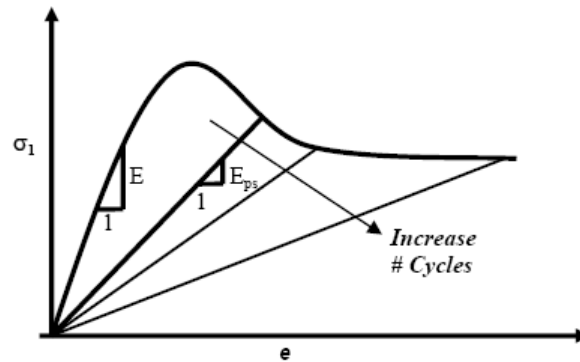


Figure 2-5 Modulus with increasing number of cycles for a given confinement stress σ_3 (after Joseph et al., 2003)

For a given confining stress (σ_3), the pseudo-elastic modulus decreases with the increasing number of cycles. With respect to deformation, a rebound phenomenon exists for broken stone during unloading (Brown, 1996). Joseph et al. (2003) proposed a pseudo-elastic deformation (δ_{ps}) consisting of an elastic deformation component (recoverable δ_e) and a plastic deformation component (irreversible δ_p) (Figure 2-6), as expressed in Equation (2-4). This pseudo-elastic model will be applied to analyse behavior of chosen limestone crush material in later chapters in the work.

$$\delta_{ps} = \delta_p + \delta_e \quad (2-4)$$

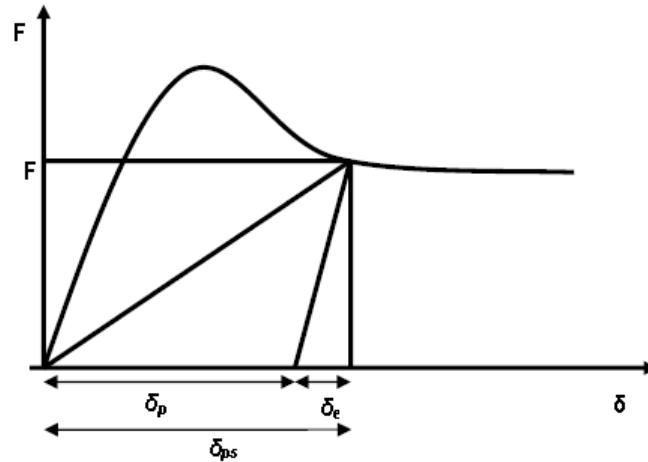


Figure 2-6 Composition of pseudo-elastic deformation during post-peak unload-reload (after Joseph et al., 2003)

2.2.2 Sand

2.2.2.1 Monotonic loading on sandy loam soil

Before reviewing cyclic plate load tests on sand, monotonic single cycle loading was reviewed to understand particle flow mechanics

Earl (2001) suggested that the behavior of a sandy loam soil during compression under a plate is directed by three phases:

1. Compaction below the plate with constant lateral stress
2. Compaction with increasing lateral stress
3. Displacement and compaction of the soil laterally

Deformation processes corresponding to lateral stress development are illustrated in Figure 2-7. During initial compaction, disturbance of soil extended to shallow surface depths of around a few millimetres disproportionately and was cylindrical in form. As sinkage developed, the deformation process underwent a transitional stage before reaching a more widely recognised form of an inverted cone caused by soil movement and compaction laterally (Earl & Alexandrou, 2001).

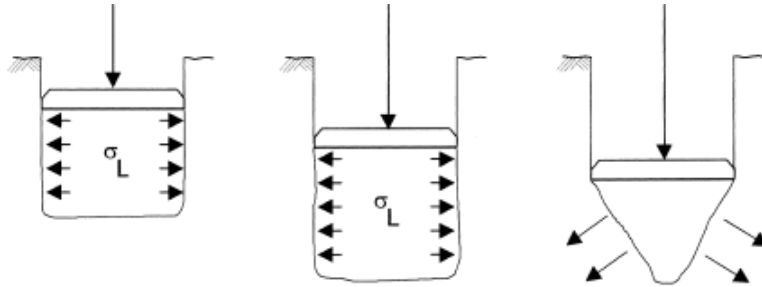


Figure 2-7 Soil deformation process of plate sinkage tests for sandy loam (after Earl & Alexandrou, 2001)

2.2.2.2 Cyclic compaction tests

Cyclic compaction tests have been conducted by Sawicki et al. (1995) aiming at studying the behaviour of various particulate materials including sands, grains and powders during cyclic compaction accounting for the induced lateral stress. A schematic arrangement of the apparatus that was used by Sawicki is shown in Figure 2-8.

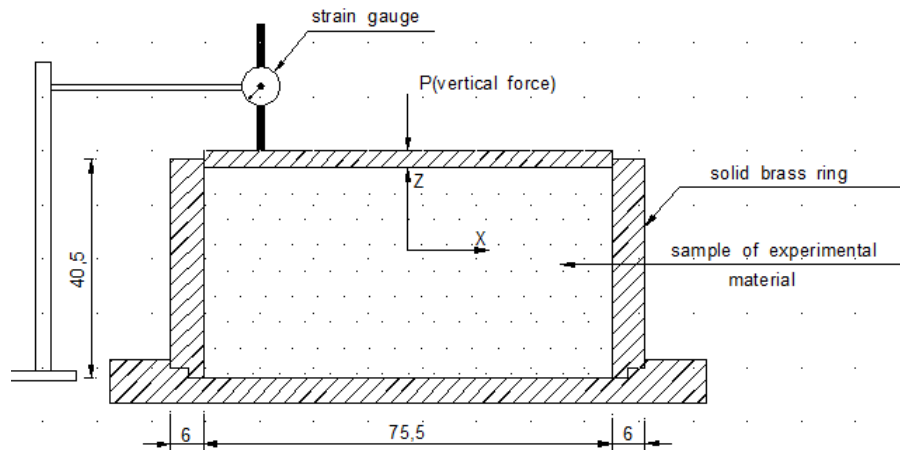


Figure 2-8 Schematic of a cyclic compaction test (after Sawicki & Swidzinski, 1995)

The following observations were made by Sawicki:

1. Rate of compaction decreases with increasing number of cycles;
2. The compaction level depends on the maximum vertical stress; The larger the stress, the higher the compaction level;

3. The residual confining stress generally increases with incremental number of cycles while the rate of lateral stress generation decreases;
4. The value of the residual lateral stress relies on the maximum vertical stress;
5. The influence of the first cycle is predominant in the process (Sawicki & Swidzinski, 1995) .

A general theoretical equation explaining the evolution of vertical strain versus number of cycles was developed by Sawicki in Equation (2-5).

$$\frac{d\varepsilon^p}{dN} = D_1(\sigma_z - \sigma_x)^m \exp(-D_2\varepsilon^p) \quad (2-5)$$

where ε^p is the irreversible vertical strain, N is the number of cycles, D_1 , D_2 and m are model constants, σ_z and σ_x are vertical and lateral stresses respectively.

As for the induced lateral stresses, a correlation with residual strain is linear where A is model constant dependent on the materials tested (Equation (2-6)).

$$\sigma_x^{res} = A\varepsilon^p \quad (2-6)$$

2.2.2.3 Cyclic plate load tests

Agarwal (2010) conducted cyclic plate load tests on dry sands, and defined a local stiffness as the ratio of load to deformation between two consecutive points on a force-deformation curve, and global stiffness as the slope of a linear fit of the curve. He mentioned that

1. Sand particles slip relative to each other to overcome frictional forces acting between them;
2. The sand mass under a plate tends to move out of the developed pressure bulb (Boussinesq theory) and effectively causes lateral deformation;
3. On initial loading, the stiffness of the material varied from low to high then decreased gradually.

4. The local stiffness in the loading and unloading portions of the cycle was wide spread regardless of the applied load and frequency;
5. As the number of cycles increases, a loading global stiffness increases while unloading global stiffness decreases. There was no good correlation established by Agarwal between global stiffness and number of cycles.

2.2.3 Other soils

2.2.3.1 Shear stress-strain characteristics of clay soil

It is acknowledged that shear stress-strain characteristics of soil are not linear due to probable strain-softening or work-hardening occurring under cyclic loading, which makes behavior of soil under cyclic loading very complicated to decipher.

Over the past several decades, researchers have dedicated efforts to constituting “skeleton curves” (Figure 2-9) to describe nonlinear behavior (Hardin & Drnevich, 1972; Matasovic & Vucetic, 1993; Nakagawa & Soga, 1995; Ni, Siddharthan, & Anderson, 1997). Among them, there are two widely used models: A Hyperbolic model (Kondner, 1963), as shown in Equation (2-7) and the Ramberg—Osgood model (Ramberg & Osgood, 1943), as indicated in Equation (2-8).

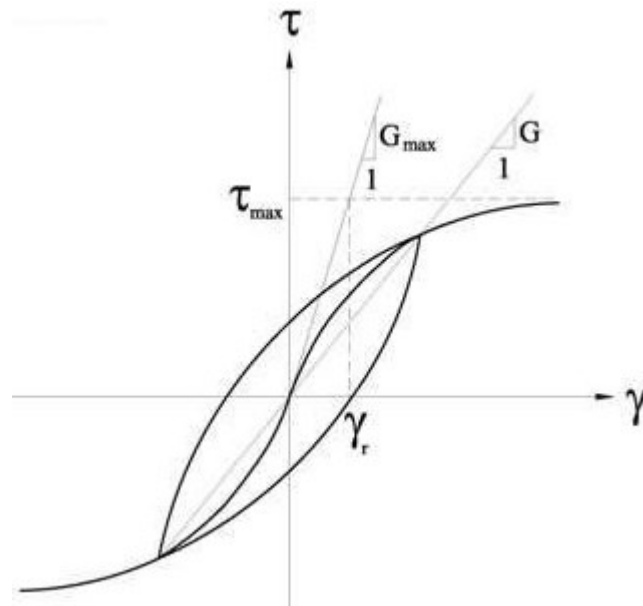


Figure 2-9 Hyperbolic model of soil shear stress-strain curve

$$\frac{d\tau}{d\gamma} = G_{\max} \left(1 - \frac{\tau}{\tau_{\max}}\right)^n \quad (2-7)$$

where τ_{\max} is the horizontal asymptote on τ -axis and G_{\max} is tangent slope of stress-strain curve when τ equals to zero, and n is a constant.

$$\gamma = \frac{1}{G_{\max}} \tau \left(1 + \alpha \left(\frac{\tau}{\tau_{\max}}\right)^{r-1}\right) \quad (2-8)$$

where α and r are constants.

Masing (1926) assumed that when unloading and reloading commenced, the shear modulus would remain the same. After passing through “x-axis”, the stress-strain curve followed a “mirror” skeleton curve in reverse. As per the two assumptions, he proposed “Masing’s rule” to build a “hysteresis loop” on a basis of the skeleton curve, as exhibited in Figure 2-10.

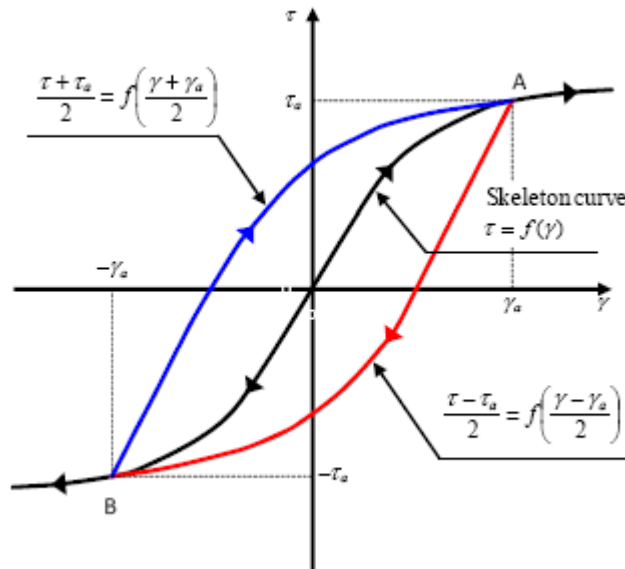


Figure 2-10 Skeleton curve and hysteresis relationship based on Masing’s rule (after Ishihara, 1996)

If the load reversed at point A, where shear strain is equal to γ_a and shear stress is τ_a , then the unloading function may be expressed by Equation (2-9).

$$\frac{\tau - \tau_a}{2} = f\left(\frac{\gamma - \gamma_a}{2}\right) \quad (2-9)$$

If reloading occurred at point B, the stress-strain curve for the reloading is given by Equation (2-10).

$$\frac{\tau + \tau_a}{2} = f\left(\frac{\gamma + \gamma_a}{2}\right) \quad (2-10)$$

For such a “hysteresis loop”, the area of the loop (ΔW) represents the strain energy dissipation within one cycle. Strain energy at $(\tau_\alpha, \gamma_\alpha)$, where according to Figure 2-10, is equal to

$$W = \frac{1}{2} f(\gamma_\alpha) \gamma_\alpha \quad (2-11)$$

If the damping ratio, D , is defined as Equation (2-12),

$$D = \frac{1}{4\pi} \frac{\Delta W}{W} \quad (2-12)$$

Then a strain softening or hardening index may be predicted based on the damping ratio.

In the case of saturated soft clay, strain softening (degradations of stiffness) will take place under cyclic loading. Jjan & Xiaonan (2000) performed a tri-axial cyclic test on saturated soft clay and demonstrated that the increment of cycles and cyclic stress ratio would accelerate strain softening.

2.2.3.2 Oil sand behavior under cyclic plate loading

Sharif-Abadi (2006) carried out laboratory cyclic plate load tests on oil sand with 8% and 11% bitumen content respectively. Figure 2-11 shows three loading phases in his tests. He proposed a pseudo-elastic model to describe oil sand behavior under cyclic loading and observed that with increasing number of cycles, stiffness of oil sand increased and converged to a relative constant value. The total

deformation of initial, constant held and cyclic loading can be predicted by Equation (2-13).

$$\delta_T(mm) = [\sigma(KPa) / At^B] + [\sigma(KPa) / \sum_{i=1}^{NC} 106.7 \times (NC)^{0.3}] \quad (2-13)$$

where NC is number of cycle and t is time in seconds. A and B are constants.

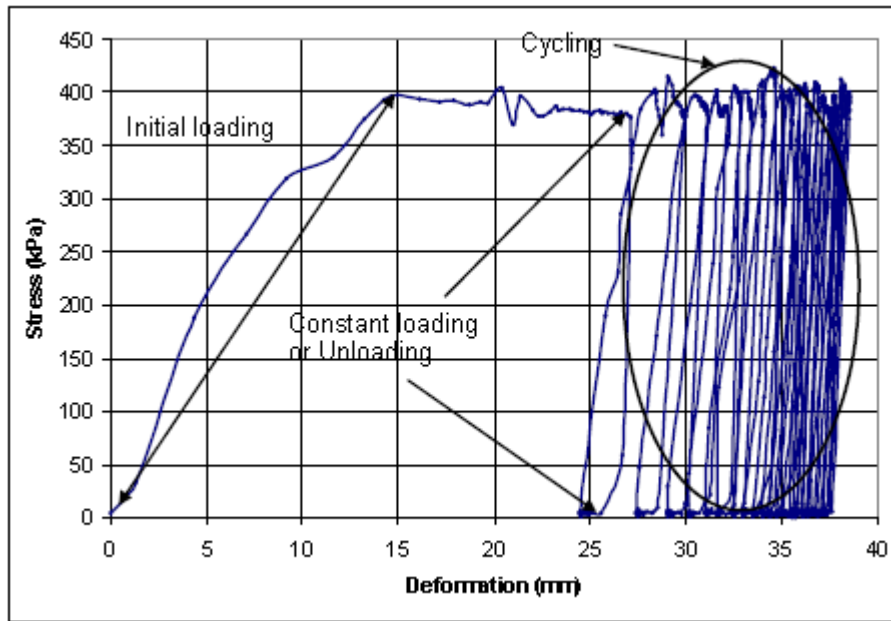


Figure 2-11 Three loading phases: initial loading, constant loading and cyclic loading (after Sharif-Abadi, 2006)

2.2.4 Crushed rock with fines

Crushed rock classified as one type of gravel is graded by screens then mixed to a blend of crushed rock and fines (referred as one of the unbound granular materials in this section).

2.2.4.1 Gradation

Given that unbound granular material is a mixture of different size particles, grain gradation becomes very important. Thom & Brown (1988) evaluated the grading effect on the stiffness and resistance to permanent deformation of crushed dolomitic limestone and concluded that with increasing fines content, interlock

particles reduced contact, and frictional forces at contact faces decreased (Figure 2-12). Consequently, stiffness and resistance decreased. It is the same type of material that has been used in this thesis work.

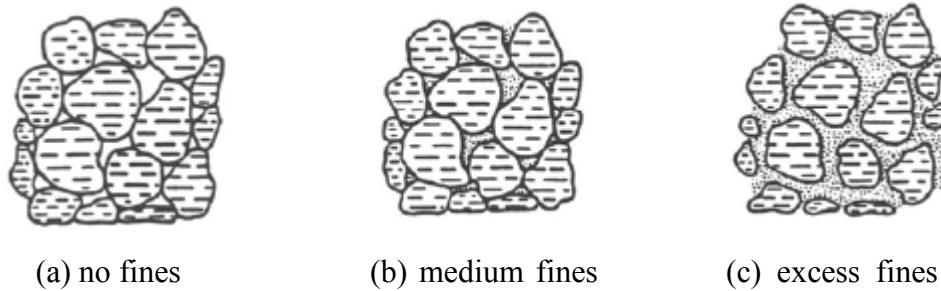


Figure 2-12 Fines content in crushed stone (after Thom & Brown, 1988)

2.2.4.2 Resilient modulus (M_r)

Previous research on mechanical behaviour of unbound granular materials under cyclic loading considered resilient modulus and permanent deformation behavior.

Resilient modulus is defined as the ratio of applied deviatoric stress to the corresponding recoverable axial strain (Luzia, Picado-Santos & Pereira, 2008).

Equation (2-14) and Figure 2-13 show the resilient modulus.

$$M_r = \frac{\sigma_{deviator}}{\epsilon_r} = \frac{\sigma_1 - \sigma_3}{\epsilon_r} \quad (2-14)$$

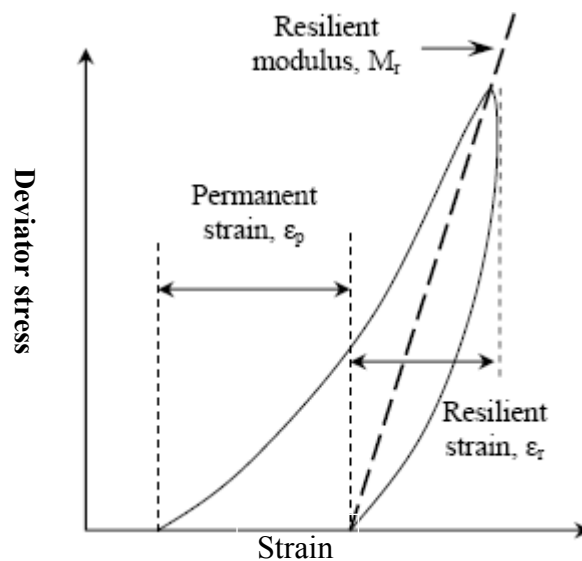


Figure 2-13 Specimen Response during axial load-unload (after Brown, 1996)

In order to establish the resilient modulus of different materials, several tests have been developed over the past several decades, such as: (1) the tri-axial test, (2) the torsional shear test, (3) the simple shear test, (4) the hollow cylinder test, (5) the falling weight deflectometer (FWD) test and (6) the cyclic plate load test, etc. Of them, the cyclic plate load test is the most appropriate to determine the overall resilient modulus of a pavement material when the material is not easily sampled, is layered and may be a composite with other materials (Qian, Han, Pokharel & Parsons, 2011).

The most common laboratory tests to determine resilient modulus for unbound granular materials under cyclic loading are cyclic tri-axial tests. Thom & Brown (1988) conducted the tests on unbound gravel materials and plotted stress-strain curve (Figure 2-14). It can be seen that the rate of incremental unrecoverable deformation per cycle decreases with increasing number of cycles. In another words, the plastic deformation occurs primarily in the first few cycles (Barksdale, 1972; Huurman, 1997; Sweere, 1990).

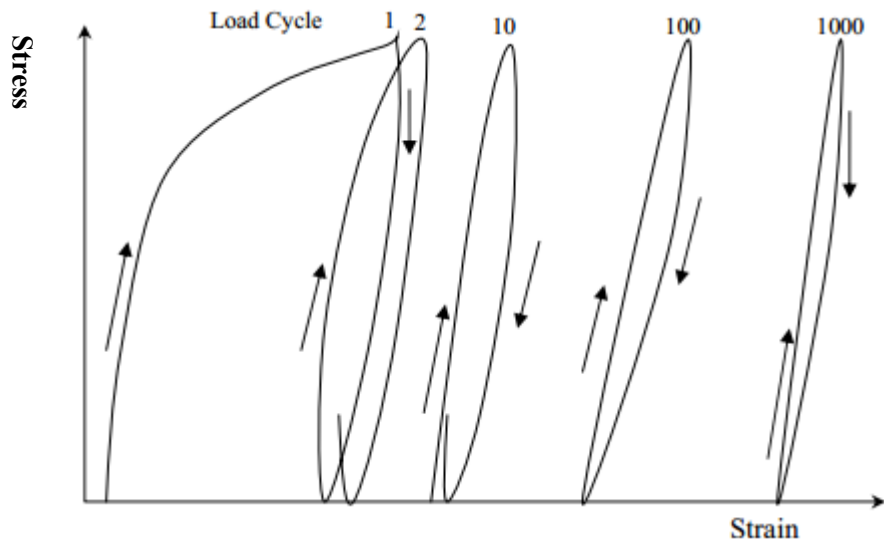


Figure 2-14 Unbound granular material stress-strain curve from cyclic tri-axial test (after Thompson & Brown, 1988)

Resilient modulus is not a constant stiffness property but depends upon various factors like stress state, which includes the deviatoric and confining stress, soil type and structure. These primarily rely on compaction methods and compaction effort (Li & Selig, 1994). Resilient modulus increases with a decrease in moisture content and an increase in density. There is a critical degree of saturation near 80-85 percent, above which granular material becomes unstable and goes through degradation rapidly under cyclic loadings (Farrar & Turner, 1991). LeKarp, Isaacsson & Dawson (2000) noted, and other researchers concurred that resilient modulus of unbound granular soils increased with increasing confining stress and the sum of the principal stresses (known as the bulk stress (θ)), increases with deviatoric stress. However the deviatoric stress is more significant than confining stress for fine-grain soils. Higher deviatoric stress leads to lower resilient modulus.

With time, researchers have taken effort to build models to predict the dependency of applied force. Among them there are two common models. They are the M_r - θ model and the Uzan model.

$$M_r = k_1 \theta^{k_2} \quad (2-15)$$

$$\theta = \sigma_1 + \sigma_2 + \sigma_3 \quad (2-16)$$

where k_1 and k_2 are empirical constants which depend on the type of material. θ is the bulk stress (Hicks & Monismith, 1971).

$$M_r = k_{u1} p_a \left(\frac{\theta}{p_a} \right)^{k_{u2}} \left(\frac{\tau_{oct}}{p_a} + 1 \right)^{k_{u3}} \quad (2-17)$$

where k_{u1} k_{u2} k_{u3} are empirical constants depending on the type of granular material. τ_{oct} is the octahedral shear stress and p_a is the atmospheric pressure (Uzan et al.,1985).

Laboratory resilient modulus determinations usually take great time and effort. Therefore, several correlations were developed such as the California Bearing Ratio (CBR) and Dynamic Cone Penetration (DCP) tests to estimate the resilient modulus. AASHTO (Transportation Officials, 1993) suggested one common equation in terms of California Bearing Ratio (CBR) to predict the resilient modulus shown in Equation (2-18) (Heukelom & Klomp, 1962).

$$M_r = 1500(CBR) \text{ psi} \quad (2-18)$$

Another empirical equation was recommended by Thompson & Visser (1996), as shown in Equation (2-19). It is more applicable for a haul road design when a multi-layered elastic construction is developed using layered CBR value to represent resilient modulus.

$$M_r = 17.63 CBR^{0.64} \text{ MPa} \quad (2-19)$$

Gudishala (2004) gave a M_r value which varies from 150 MPa for sand to 250 MPa for crushed limestone.

2.2.4.3 Permanent deformation

Barksdale (1972) utilized lognormal methods to establish the relationship between permanent strain, ϵ_p , and the number of load repetitions, N , from laboratory cyclic tri-axial tests (Equation (2-20)).

$$\epsilon_p = a + b \log(N) \quad (2-20)$$

Yohannes, Hill & Khazanovich (2014) showed materials with lower stiffness have larger strain during both loading and unloading, with the help of discrete element

method (DEM) simulations based on a mechanistic contact models. They also identified that resilient modulus was sensitive to the applied force and increased with increasing confining stress. The simulation results are adapted in Figure 2-15. The sample illustrated has 1500 particles of diameter $10 \pm 1mm$, $\rho = 2650kg / m^3$, $\nu = 0.5$ and particle moduli of elasticity of 29 GPa. This shows a very clear view of the deformation development process and stress-strain impact under cyclic loading. After 170 cycles, the permanent deformation approaches a constant value.

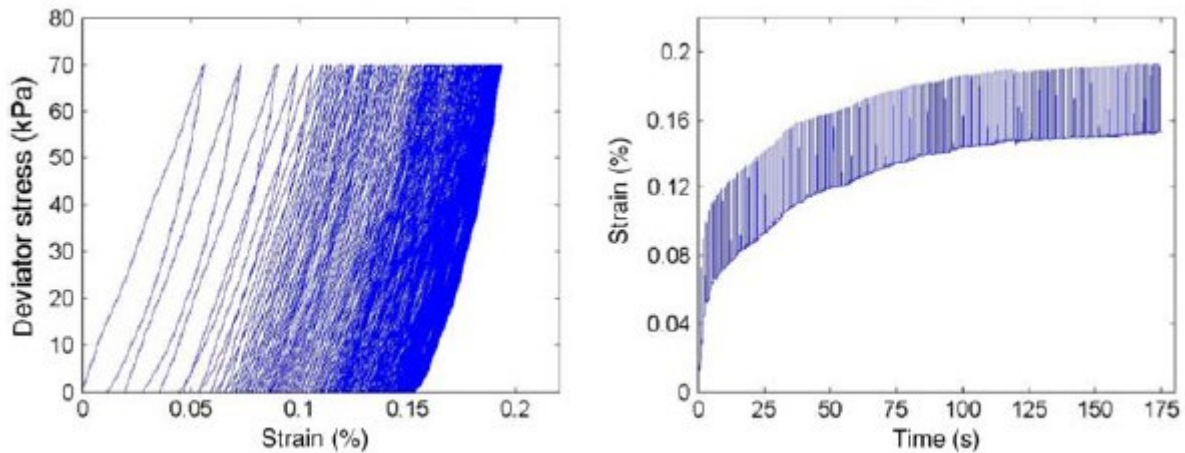


Figure 2-15 Simulation results (a) stress-strain curve (b) strain incurred for (a) (after Yohannes et al., 2014)

2.3 Two methods in haul road design

A road can be built on almost any in-situ material, while if the material is particularly weak (deforms easily when a load is applied) or a hauler is especially heavy, then a thicker covering cap layer would be required to protect the in-situ material from the loading by mining equipment. Similarly, if the material used to build the covering cap layer were weak, a thicker series of progressively stronger layers would be required (Thompson & Visser, 1997). The Boussinesq method focuses on the stress distribution of the external load (traffic) impact on the strata making up the road. The CBR test evaluates the strength of the respective or total

material compaction and reflects overall performance. Combining the CBR and Boussinesq permits a good haul road construction to be designed.

2.3.1 Boussinesq Method

The Boussinesq method plays an important role in geotechnical and road engineering. It is a linear elastic method. The original Boussinesq equations are applied for vertical point loads over homogeneous, isotropic, elastic half-space materials. As explained in the following four Equations (2-21), (2-22), (2-23) and (2-24) (Boussinesq, 1885), vertical, horizontal and shear stress and vertical displacement at any depth may be obtained.

Vertical stress

$$\sigma_z = \frac{3Q}{2\pi z^2} \left\{ \frac{1}{1 + \left(\frac{r}{z}\right)^2} \right\}^{\frac{5}{2}} \quad (2-21)$$

Horizontal stress

$$\sigma_r = \frac{Q}{2\pi} \left\{ \frac{3r^2 z}{(r^2 + z^2)^{\frac{5}{2}}} - \frac{1 - 2\nu}{r^2 + z^2 + z(r^2 + z^2)^{\frac{1}{2}}} \right\} \quad (2-22)$$

Shear stress

$$\tau_{rz} = \frac{3Q}{2\pi} \left\{ \frac{rz^2}{(r^2 + z^2)^{\frac{5}{2}}} \right\} \quad (2-23)$$

Vertical displacement

$$w = \frac{Q(1+\nu)}{2\pi E} \frac{1}{R} \left[\frac{z^2}{R^2} + 2(1-\nu) \right] \quad (2-24)$$

where $R^2 = x^2 + y^2 + z^2$, ν is the Poisson's ratio.

Florin (1959) and Newmark (1935) discussed a uniform load condition acting on a rectangular underfoot. The geometry of the rectangular area under a uniform load is shown in Figure 2-16 .

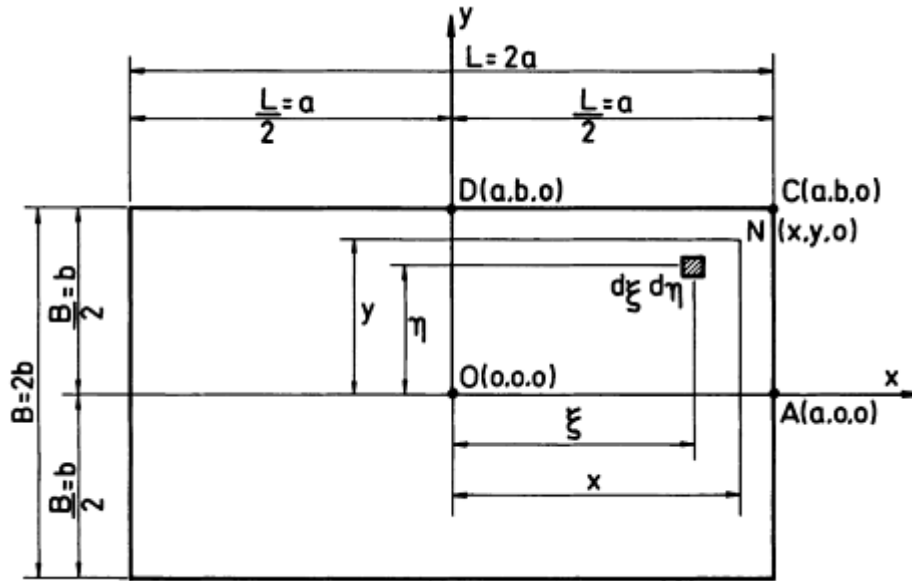


Figure 2-16 Geometry of a rectangular area

With the knowledge of differential and integral calculus, Equation (2-21) can be rewritten as Equation (2-25).

$$d\sigma_z = \frac{3pz^3 d\xi d\eta}{2\pi R^5} \quad (2-25)$$

$d\sigma_z$ is the elementary vertical stress at surface $d\xi d\eta$, and elementary force $dP = pd\xi d\eta$, where p is uniform pressure.

After a double integration of Equation (2-25), the vertical stress under a uniform area load at a depth of z is expressed in Equation (2-26).

$$\sigma_z = \frac{3pz^3}{2\pi} \int_{-a-b}^a \int_{-a-b}^b \frac{d\xi d\eta}{[(x-\xi)^2 + (y-\eta)^2]^{\frac{5}{2}}} \quad (2-26)$$

This introduces $m=L/B$, $n=z/B$, and the expression above becomes:

$$\sigma_z = \frac{p}{2\pi} \left[\frac{mn(1+m^2+2n^2)}{(1+n^2)(m^2+n^2)\sqrt{1+m^2+n^2}} + \operatorname{arctan} \frac{m}{n\sqrt{1+m^2+n^2}} \right] = \frac{p}{2\pi} I_z \quad (2-27)$$

The dimensionless coefficient I_z has been calculated for a specific ratio (L/B) by many investigators. The value of I_z can be achieved by table reference.

The corresponding displacement at the corner C (a,b,0) equals to

$$w = \frac{PB}{E} {}_c I_w \quad (2-28)$$

where ${}_c I_w$ is the displacement influence factor.

Schleicher (1926) proposed another equation to estimate displacement (Δz) beneath the corner of a rectangular area

$$\Delta z = \frac{PB}{\pi E} (1-\nu^2) \left[\lambda \ln \frac{1+\sqrt{1+\lambda^2}}{\lambda} + \ln(\lambda + \sqrt{1+\lambda^2}) \right] \quad (2-29)$$

$$\lambda = L/B \quad (2-30)$$

Joseph (2002) simplified and discerned through testing that the influence depth, D , represents the volume below an underfoot area directly affected by a surface load. It is a function of the footprint area of mining equipment. The relationship is given in Equation (2-31).

$$D = 3\sqrt{A} \quad (2-31)$$

Perloff (1976) derived the vertical stress distribution under a circular plate on the surface of an elastic half-space element. He identified that the stress was intensively concentrated at shallow depth and reduced in magnitude with increasing depths. Figure 2-17 shows the contours of vertical stress beneath the loading area. It exhibits a bulb shape, so called the 'Boussinesq bulb'. The size of the pressure bulb is proportional to the size of the loaded area. When the depth, Z , reaches 3 times of the diameter of the plate, there is only 15% stress left along the centerline of the plate.

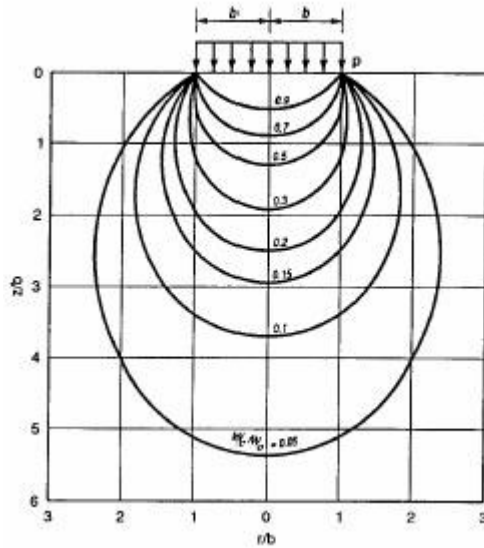


Figure 2-17 Boussinesq bulb under a circle area (after Perloff, 1976)

In the case of other shaped footing areas, “Boussinesq bulb” appears to be more slender for a square footprint shape one compared with a long continuous one, as illustrated in Figure 2-18.

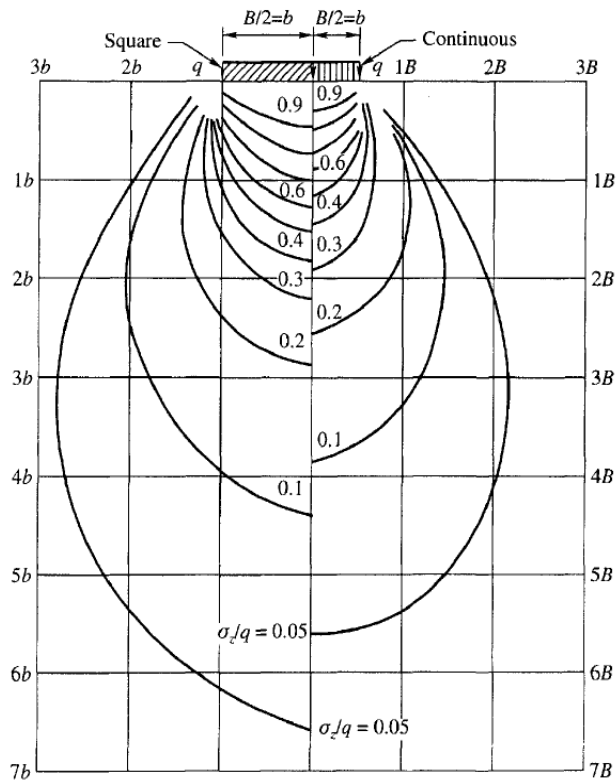


Figure 2-18 Boussinesq bulb under square and continuous area

2.3.2 California Bearing Ratio (CBR)

The California Bearing Ratio (CBR) is a compaction-penetration test applied to the surface of material and used to investigate the potential strength of subgrade, sub-base, and base materials. The CBR value derived from laboratory CBR Tests is a percentage of the penetration resistance of that material compared to that of a standard value for idealized crushed stone (set as 100%)(ASTM (2007) D1883).

A flexible haul road generally consists of four layers. They are wearing cap surface, base course, sub-base and subgrade from top to bottom. The construction material type and thickness of each layer differ by purpose and site availability. In terms of CBR, successive layers should be of higher value than the preceding layer.

Thompson & Visser (1997) suggest a limiting vertical strain value for different mine haul road categories, as present in Figure 2-19. In addition, the combined thickness of the wearing cap surface, base, and sub-base (needed when in-situ soil is weak) must be large enough to spread and distribute the stresses that are transmitted down through the subgrade to prevent excessive distortion or displacement of the subgrade. So the other layers' thicknesses are a function of applied load and CBR value (Sharif-Abadi & Joseph, 2010).

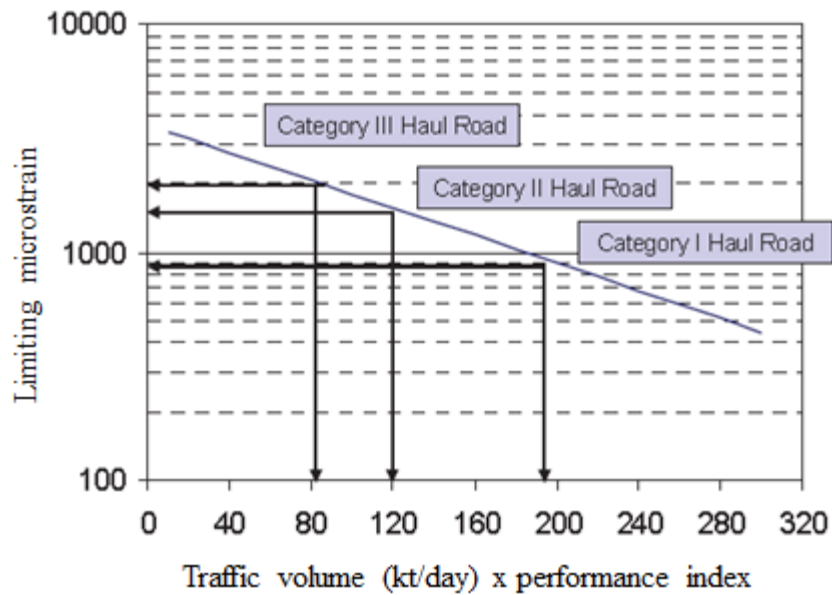


Figure 2-19 Haul road categories (after Thompson & Visser, 1997)

The California Bearing Ratio (CBR) cover-curve design method developed by Kaufman & Ault (1978) has been widely applied in mine haul road design. Figure 2-20 presents an updated version of the US Bureau of Mine (USBM) CBR design chart appropriate for wheel loads generated by typical 6-wheeled rear-dump trucks (Thompson, 2011). Figure 2-21 depicts the approximate resilient modulus of various soils types defined by the Unified Soil Classification (USCS) and AASHTO. Figure 2-20 and Figure 2-21 are comparable via effective modulus (resilient modulus). For example a 630 (t) GVW truck, driving on a road covered by one of silt (ML) or lean clay (CL) material, with a CBR value of about 8.5 % and resilient modulus of 69 MPa, indicated that the thickness of this cover base should be at least 1300 mm.

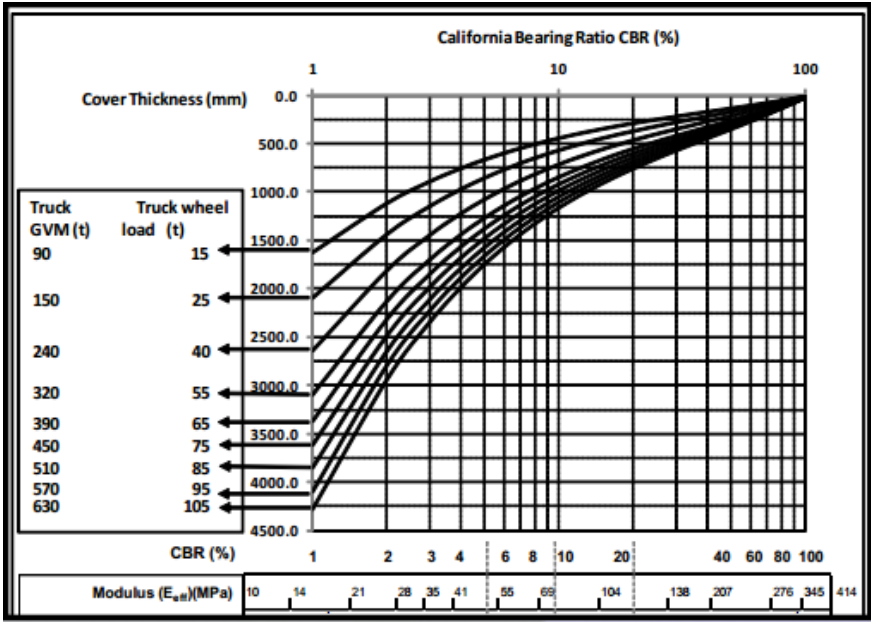


Figure 2-20 Ultra-class truck USBM CBR design chart (after Thompson, 2011)

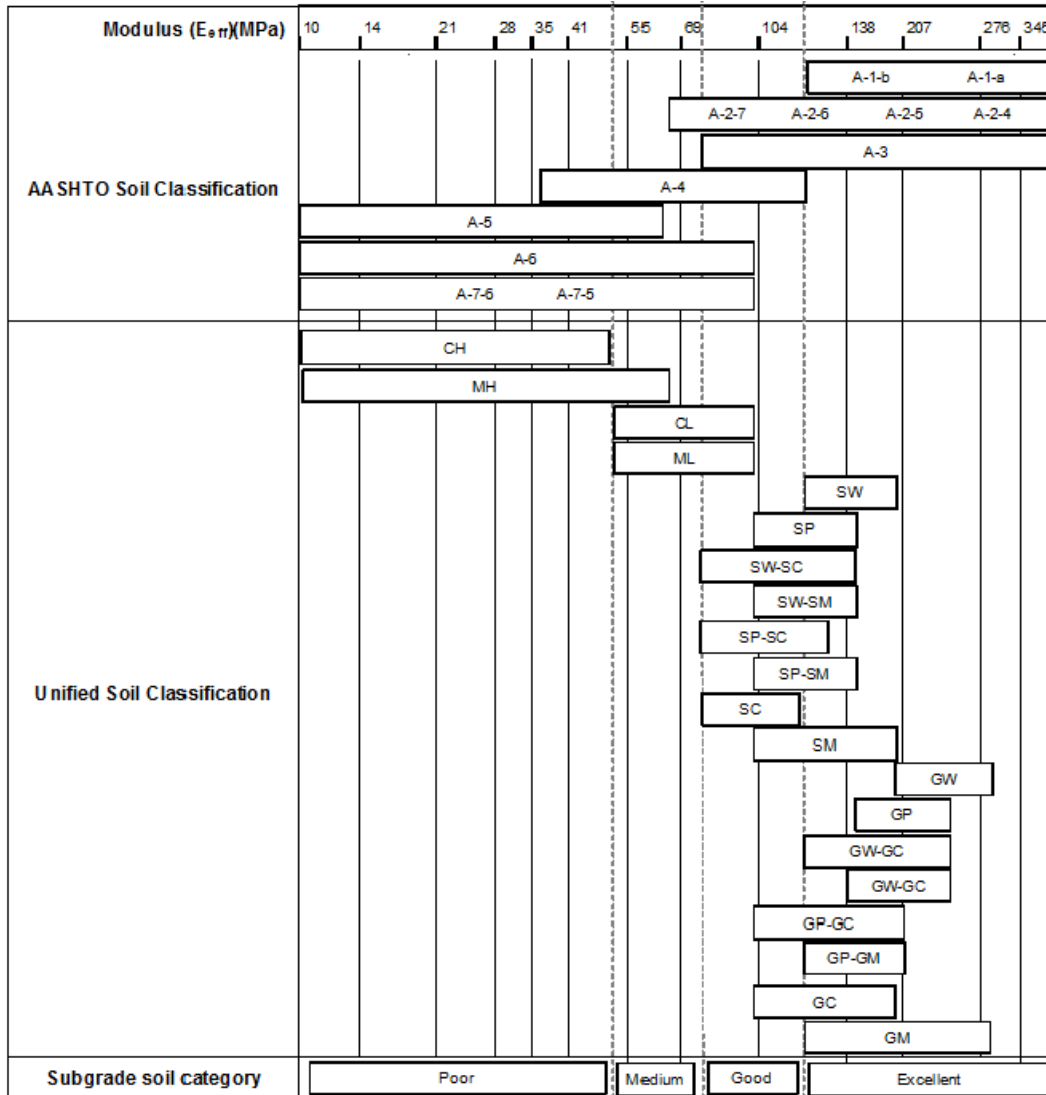


Figure 2-21 Approximate CBR values of various soils types accommodate with AASHTO and Unified Soil Classification (USCS) (after Thompson, 2011)

3 Shovel equilibrium and Ground pressure

Shovel stability not only has direct impact on structural life and safety of operators, but also impact ground deterioration, which will in turn aggravate shovel structural and mechanical fatigue failure; ultimately affecting the productivity and maintenance costs of mining. Given that downward spiral deterioration interaction, both shovel motion and ground response must be studied in parallel. The focus of this chapter is to understand shovel body balance and pressure distribution on a shovel track during digging activities.

3.1 Shovel equilibrium

In investigating shovel balance, static forces and moment equilibria are considered. A simplified schematic of a mining cable shovel is present in Figure 3-1. If the saddle block center (O) is selected as the pivot point, moment equilibria equations and force balance equations in the vertical y-axis direction of the entire shovel body are present in Equation (3-1) and (3-2). Nomenclature for the equations is described in Table 3-1.

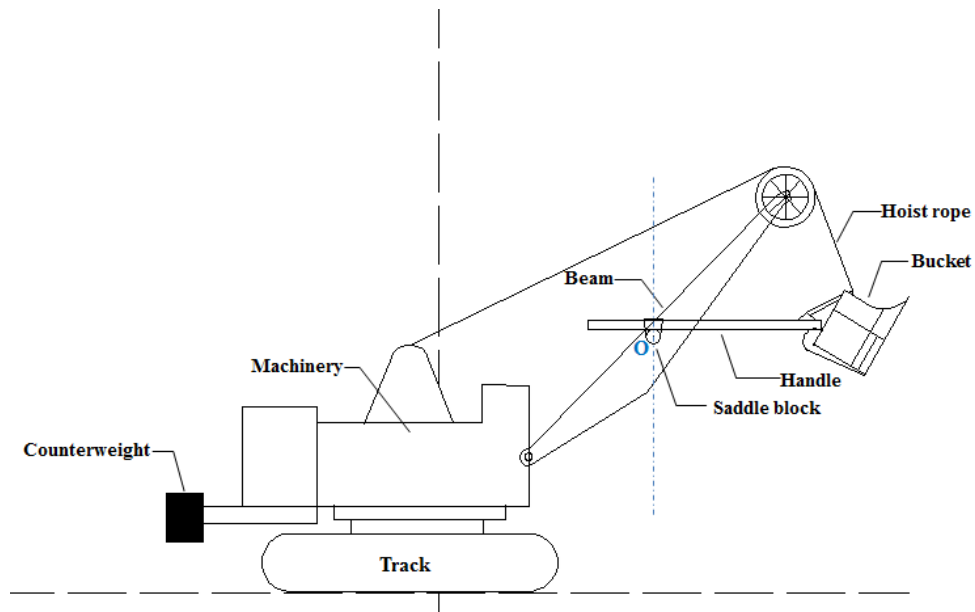


Figure 3-1 A simplified schematic of mining cable shovel

$$\sum M^{shovel} = 0$$

$$m_{machinery}g \cdot L_m + m_{counterweight}g \cdot L_c = m_{beam}g \cdot L_b + M_R + F_N \cdot L_N \quad (3-1)$$

$$\sum F_y^{shovel} = 0$$

$$F_N = m_{machinery}g + m_{beam}g + m_{counterweight}g + F_{Ry} \quad (3-2)$$

Table 3-1 Nomenclature in shovel balance analysis

$m_{machinery}g$	Weight of frame, track and machinery	L_m	Arm of $m_{machinery}g$
$m_{counterweight}g$	Weight of counterweight	L_c	Arm of $m_{counterweight}g$
$m_{beam}g$	Weight of beam	L_b	Arm of $m_{beam}g$
M_R	Moment of F_R		
F_R	Resistance from digging surface	L_R	Arm of F_R
F_{Ry}	Component of F_R on y-axis direction		
F_N	Ground Support Force	L_N	Arm of F_N

Considering a P&H 4100C BOSS mining shovel, dimensions and weights may be established for manufacture data, as provided in Table 3-2.

Table 3-2 Dimensions and weights for P&H 4100C BOSS mining shovel

$m_{machinery}$	725 (t)	L_m	7.5 (m)
$m_{counterweight}$	250 (t)	L_c	15.5 (m)
m_{beam}	115 (t)	L_b	4 (m)

In order to acquire the ground support force F_N and its acting point on shovel track, the resistance force (F_R) and moment (M_R) due to the digging surface reaction need to be estimated first. Selecting the shovel dipper system as the object, a free body diagram of a simplified shovel dipper system is shown in Figure 3-2. The moment equilibria equations and force balance equations in the

vertical y-axis direction of the shovel dipper system are illustrated in Equations (3-3) and (3-4). New nomenclature here is explained in Table 3-3.

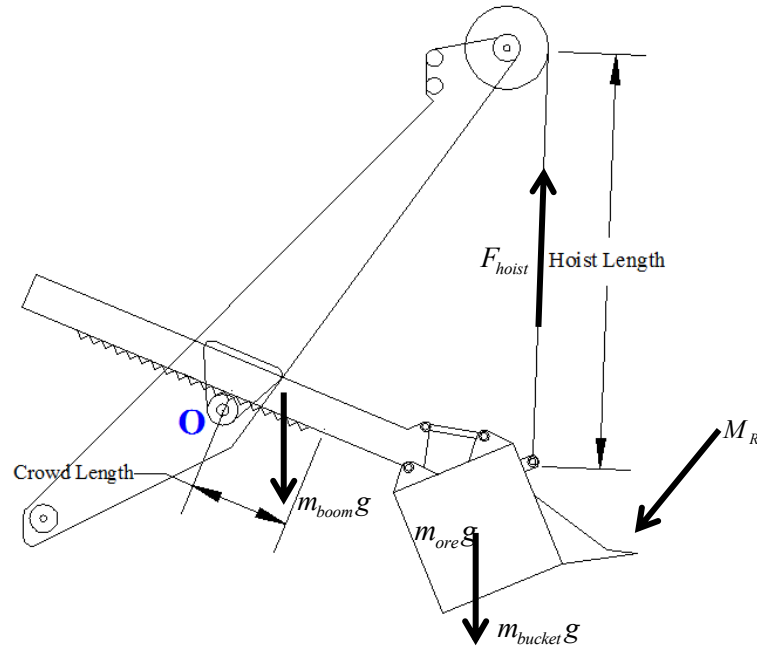


Figure 3-2 Free body diagram of a simplified shovel dipper system

$$\sum M^{dipper} = 0$$

$$F_{hoist} L_{hoist} + m_{handle} g \cdot L_{handle} = (m_{bucket} + m_{ore}) g \cdot L_{dipper} + M_R \quad (3-3)$$

$$\sum F_y^{dipper} = 0$$

$$F_{hoist_y} = m_{handle} g + (m_{bucket} + m_{ore}) g + F_{R_y} \quad (3-4)$$

Table 3-3 Nomenclature in dipper system balance analysis

F_{hoist}	Hoist force	L_{hoist}	Arm of F_{hoist}
$m_{handle} g$	Weight of handle	L_{handle}	Arm of $m_{handle} g$
$m_{bucket} g$	Weight of empty bucket	L_{dipper}	Arm of $m_{bucket} g$
F_{hoist_y}	Component of F_{hoist_y} on y-axis direction		
$m_{ore} g$	Weight of excavated ore in bucket		

3.1.1 Equilibrium of hoist and crowd system

The hoist force F_{hoist} is associated with the hoist working voltage (U_{Hoist}), current (I_{Hoist}) and velocity (v_{Hoist}) which may be collected from the shovels' electrical system. Equation (3-5) was used to find a value of F_{hoist} , where η_{Hoist} represents the power frictional impacted efficiency. 0.865 is recommended for P&H 4100C BOSS cable shovel discerned by Joseph (2002) from actual vs. estimated power derived force values. It is important to note that there are two hoist motors working in parallel.

$$F_{hoist} = \frac{2 \cdot U_{Hoist} \cdot I_{Hoist} \cdot \eta_{Hoist}}{v_{Hoist}} \quad (3-5)$$

The weight of the extended handle ($m_{handle}g$) varies as digging activity progresses (as crowd extends and contracts). Research has previously been performed to find $m_{handle}g$, L_{hoist} and L_{handle} utilizing the data from the shovel on-board systems. Simplified geometric relationships and calculation methods suggested by Shi (2007) and Lin (2014) are adopted in this thesis. A detailed approach is explained in Appendix I. Results with initial shovel on-board data for one sample duty cycle are shown in Table 3-4 and Figure 3-3 and 3-4.

Table 3-4 Example of results for hoist and crowd system

I(A)	U(V)	F_{hoist} (MN)	L_{hoist} (m)	$m_{handle}g$ (kN)	L_{handle} (m)
34	319	0.02	6.53	133.92	1.21
315	283	0.18	6.65	136.16	1.25
221	249	0.11	6.74	138.12	1.29
...
1808	584	2.11	13.32	276.34	4.42
1310	573	1.50	13.25	274.13	4.38

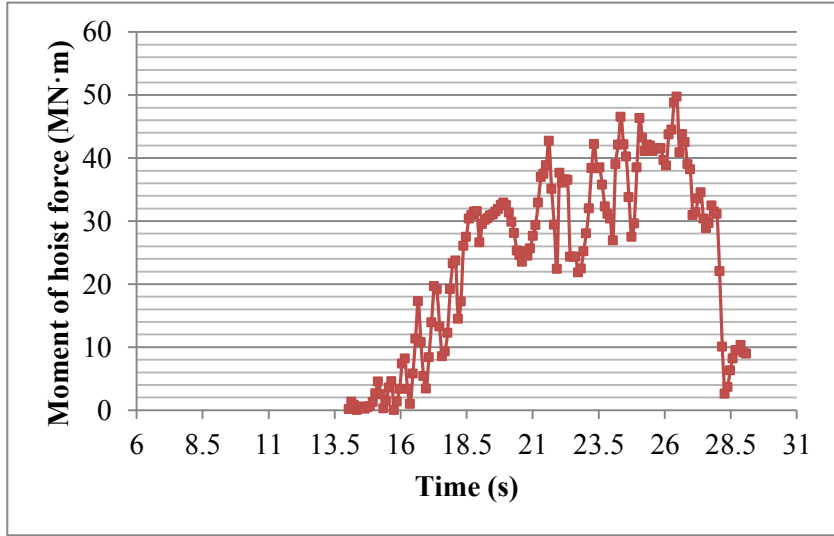


Figure 3-3 Moment of hoist force within one digging duty cycle

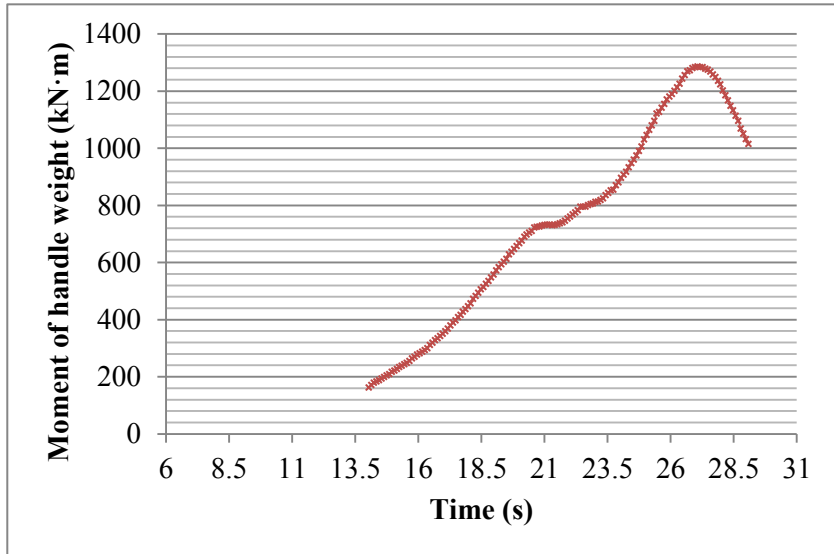


Figure 3-4 Moment of handle weight within one digging duty cycle

3.1.2 Equilibrium of dipper and digging-face system

The weight of dipper is given while ore weight and dipper position varies throughout digging duty cycle. The position of dipper can be estimated by the trajectory position at any instant. The elementary trajectory length is

$$dl = \sqrt{(x_{i+1} - x_i)^2 + (y_{i+1} - y_i)^2} \quad (3-6)$$

The elementary weight of ore excavated in the dipper is

$$dG_d = \rho g \cdot dl \cdot D \cdot d \quad (3-7)$$

where D is the dipper width (3.51 m for P&H 4100C BOSS cable mining shovel) and d is the depth of shovel teeth digging in the surface. Density ρ is $1.9 \times 10^3 \text{ kg/m}^3$ for at face oil sand. Alternatively, $(D \cdot d)$ in Equation (3-7) may be replaced by Equation (3-8), considering the productivity and efficiency of a shovel, assuming a fill factor of 95% (dipper capacity V is 48.4 m^3). Material swell factor is 1.3. Then

$$D \cdot d = \frac{V \times 0.95}{\int dl \times 3.51 \times 1.3} \quad (3-8)$$

Figure 3-5 includes sample data from the field for one digging trajectory.

L_{dipper} is calculated with the approach in Appendix II.

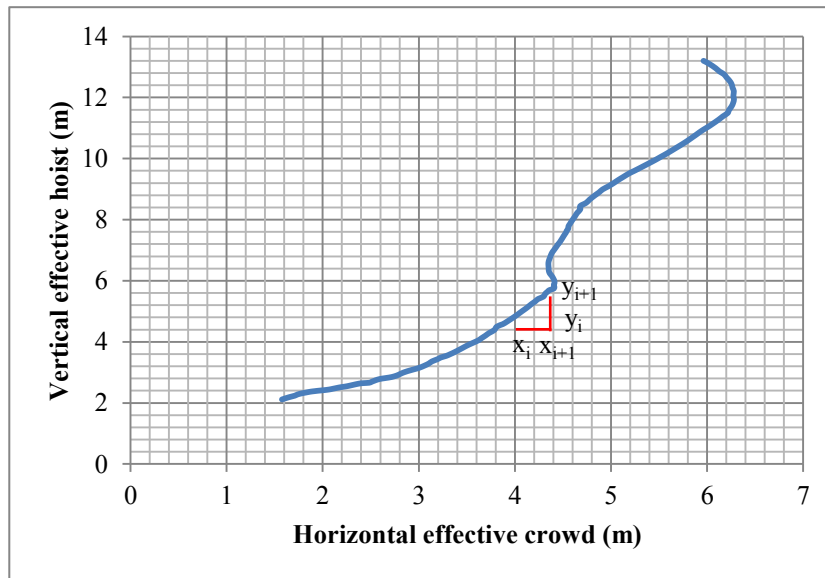


Figure 3-5 Shovel digging trajectory from field data

Accounting for the moment of the hoist and crowd system as well as the moment of dipper and ore weight, the moment of resistance from the digging surface and

the component resistance forces in the y-axis direction can be found via Equations (3-3) and (3-4). Table 3-5 is an example of results for a dipper versus digging-face system. The moment of resistance due to the digging-face is indicated in Figure 3-6.

Table 3-5 Example of results for dipper and digging-face system

$m_{ore}g$ (kN)	L_{dipper} (m)	x	y	dl	dG _d	M _R (kN · m)	F _{Ry} (kN)
5.26	0.85	1.58	2.11	0.10	5.25	-9.01	-117.19
9.42	1.03	1.65	2.19	0.08	4.17	1132.71	35.83
11.88	1.17	1.71	2.24	0.05	2.47	629.86	-37.70
...
653.51	12.27	6.02	13.11	0.16	8.52	24753.84	1541.43
659.25	12.21	5.96	13.20	0.11	5.74	25632.27	1604.60

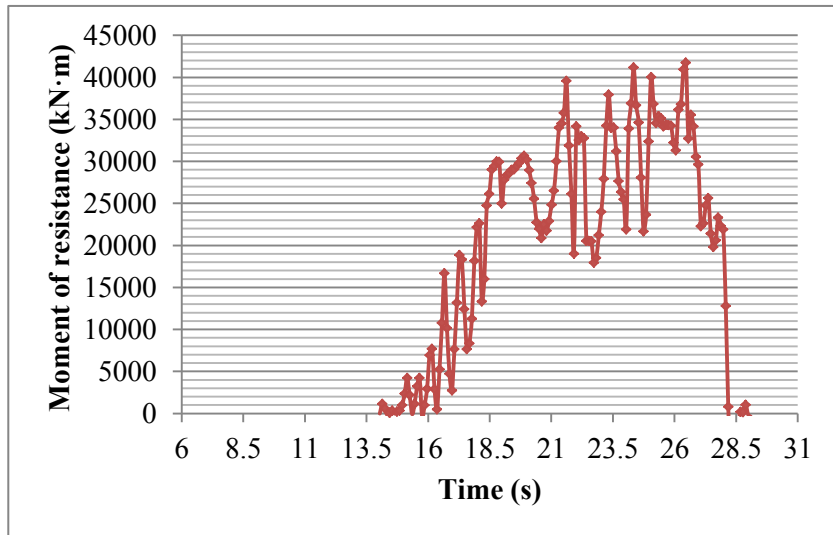


Figure 3-6 Moment of resistance from digging-face

3.2 Ground pressure

After determining the results of the moment of resistance and resistance forces in Table 3-5, Equations (3-1) and (3-2) may be used to determine the ground support

force (F_N). The track-ground contact substantially experiences pressure distribution along the interface. So F_N is converted to equivalent contact pressure proportional to the track-ground contact area. For a P&H 4100C BOSS cable shovel, the contact base load balanced area is 31.31 m^2 for each track with a length (L) of 8.92 m and width (B) of 3.51 m .

There are two possibilities of ground pressure distribution—triangle and trapezoidal.

Considering the track-ground contact area as a rectangular plane, with a side view as a line with length (L) of 8.92 m , x may be considered as the distance between any action point of F_N and the rotation axis of the shovel. A schematic reflecting this is shown in Figure 3-7.

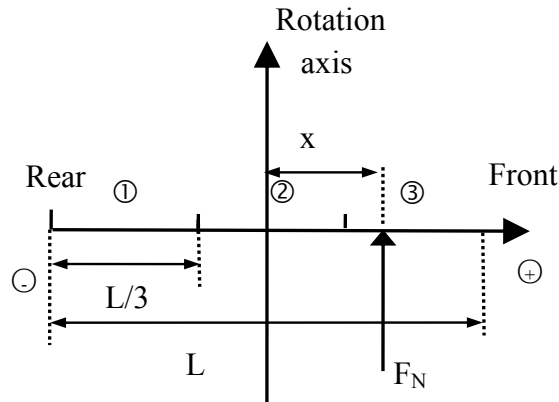


Figure 3-7 Schematic of shovel track side

If $x + L/2 \leq L/3$ or $x + L/2 \geq 2L/3$, F_N will be in region one or three, and the pressure distribution will be basically triangular in nature (as the equivalent force of a triangular distributed pressure acts on a point of the third length). Otherwise, $L/3 < x + L/2 < 2L/3$ and the total force is located in region 2, the pressure distribution is the trapezoidal.

In the case of a triangular distribution, if the maximum pressure is p_{\max} , the effective length L_x and ground force F_N can be expressed as Equations (3-9) and (3-10). A triangular distribution sketch is shown in Figure 3-8.

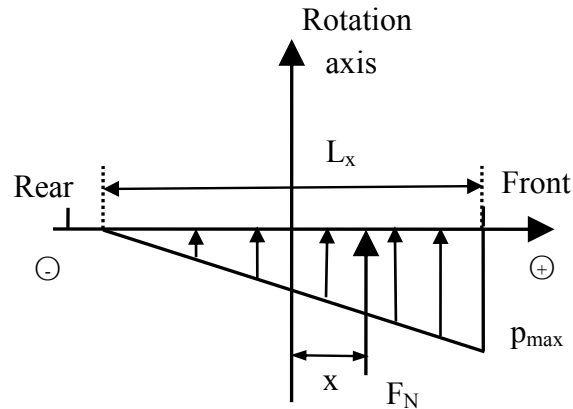


Figure 3-8 Schematic of triangular distribution

$$F_N = \frac{1}{2} p_{\max} \cdot L_x \cdot B \quad (3-9)$$

$$L_x = 3\left(\frac{L}{2} - x\right) \quad (3-10)$$

In the case of a trapezoidal distribution, pressures at the ends are p_1 and p_2 respectively. Figure 3-9 is a schematic of the pressure distribution for these cases.

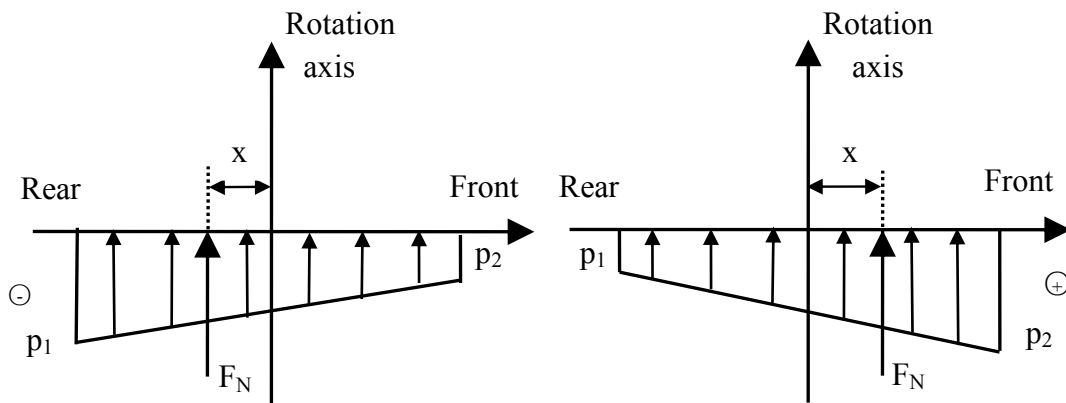


Figure 3-9 Schematic of trapezoidal distribution

Regardless p_1 or p_2 whichever is greater, equilibrium equations are the same, as noted by Equations (3-11) and (3-12).

$$F_N = \frac{1}{2}(p_1 + p_2) \cdot L \cdot B \quad (3-11)$$

$$F_N \cdot \left(\frac{L}{2} + x\right) = p_1 \cdot L \cdot \frac{L}{2} - \frac{1}{2}(p_1 - p_2) \cdot L \cdot \frac{2}{3}L \quad (3-12)$$

Table 3-6 provides an example of the ground pressure calculation parameters.

Table 3-6 Example of calculated ground pressure

$F_N(\text{kN})$	$M_{FN}(\text{kN}\cdot\text{m})$	$X(\text{m})$	$p_{\max}(\text{kPa})$	$p_1(\text{kPa})$	$p_2(\text{kPa})$
9889.02	-6655.28	-0.67	...	291.23	86.43
10042.03	-5513.57	-0.549	...	291.92	101.14
9968.50	-6016.42	-0.60	...	291.45	94.57
...
11547.63	18107.57	1.57	379.21
11610.80	18985.99	1.64	390.34

3.3 Results

In order to evaluate the track-ground contact pressure distribution during shovel dipper excavation operations, Matlab is used to exhibit ground pressure distribution along the shovel track (the Matlab code is provided in Appendix III).

Considering the digging trajectory (Figure 3-10), there are eight critical positions of dipper which are labeled as “tucked and about to engage”, “half-face digging 1”, “half-face digging 2”, “full-face digging”, “hard-face digging 1”, “hard-face digging 2”, “face release” and “carry high”. When the values of effective crowd and hoist are small, the shovel dipper is about to engage in. Where the data reflects shallow trends, the shovel is excavating harder material.

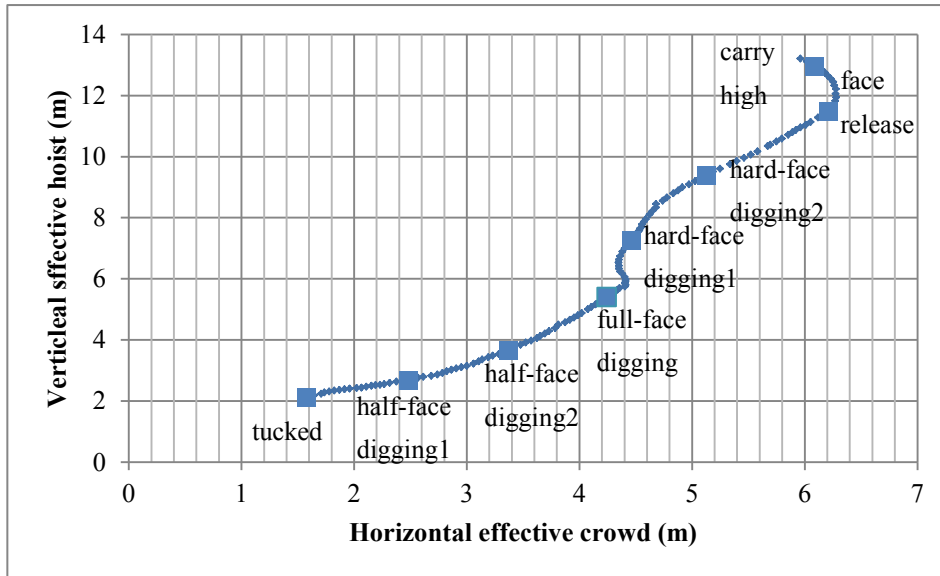


Figure 3-10 Digging trajectory with eight critical positions

Figure 3-11 is a snapshot of the ground pressure distribution along the shovel track for the eight dipper positions as discussed via the Matlab analysis. In the light of Figure 3-11

1. The maximum pressure is around 600 kPa, which occurs at the front of the track when half filling the dipper during digging hard surfaces and full dipper is about to release the digging face;
2. When the shovel dipper engages the digging face, the centre of gravity transfers from rear to front until the full-face digging condition is realized and the rear of track lifts off of the ground. Only two thirds of the track are then in contact with the ground;
3. When the shovel dipper is tucked, at half-face or free suspended carried to the dump position over a truck, the track pressure is approximately balanced;
4. The ground under the shovel track experiences most detrimental pitch motion during full-face digging, hard-face digging 1, 2 and face release;

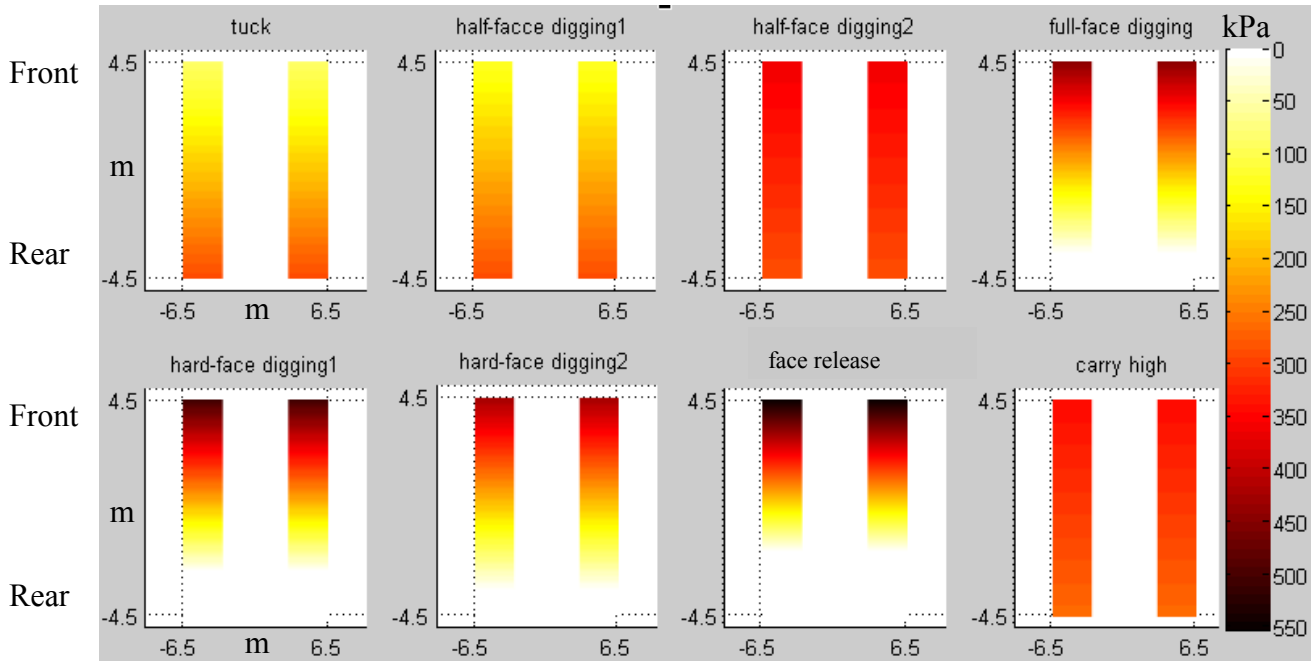


Figure 3-11 Ground pressure distribution along the shovel track for eight critical positions (units kPa)

The track-ground contact area is not always 31.31 m², hence the shovel track has been essentially divided into 6 portions (Figure 3-12). Of those, one or two typical track portions predominate. Pressure versus time graphs for different track portion have been plotted in Figure 3-13 (the Matlab code is provided in appendix IV).

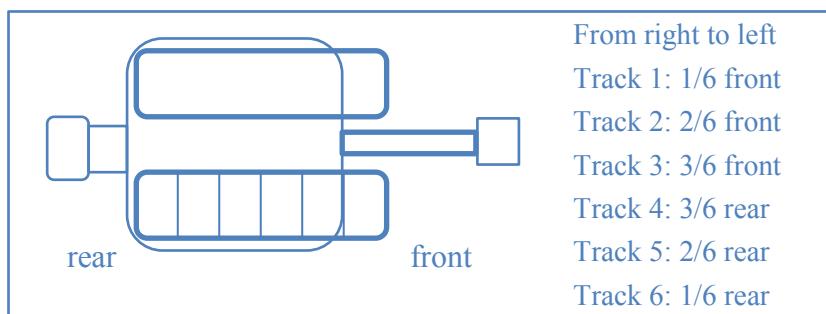


Figure 3-12 Shovel track allocation

It can be concluded that the track 1 (referred to as 1/6 front track) experiences shocks up to maximum pressure of 600 kPa varying intensely at an amplitude of 500 kPa. Tracks 2, 3 (referred to as 2/6 front and 3/6 front track respectively) and

tracks 4, 5, 6 (referred to as 3/6 rear, 2/6 rear and 1/6 rear track respectively) have similar amplitudes of 300 kPa, while the former has higher average pressures around 300 kPa, the latter have an average pressures of 200 kPa.

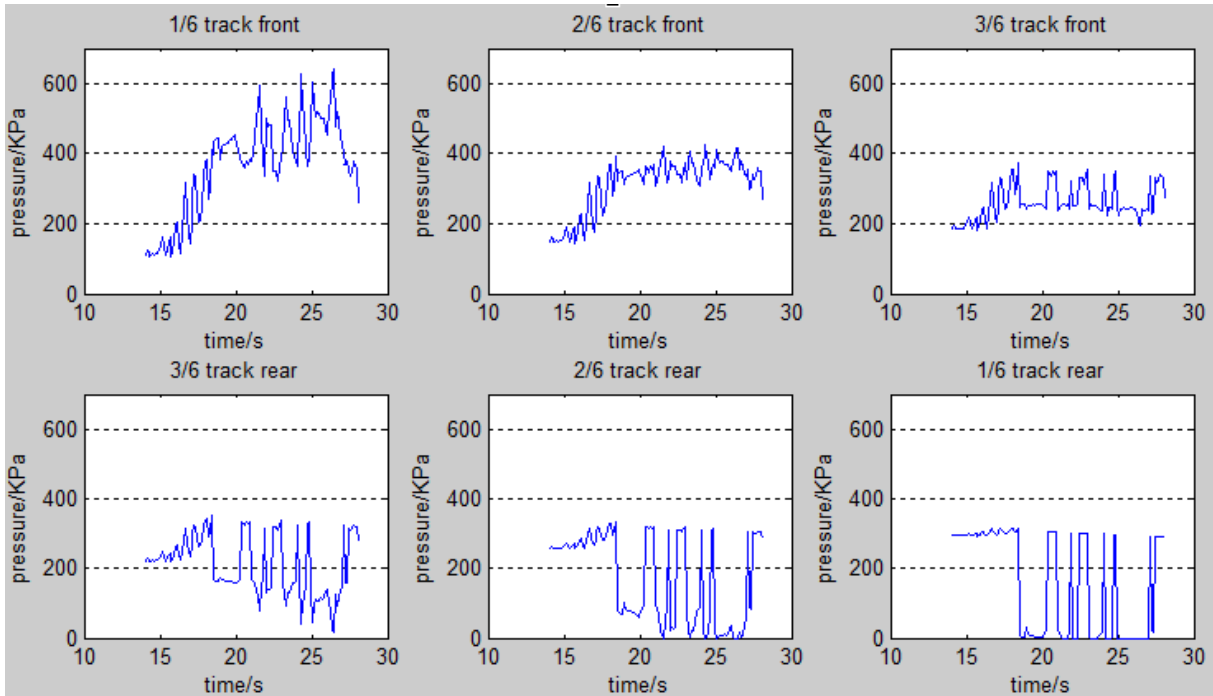


Figure 3-13 Pressure versus time for 6 specific track portions during excavating

It's also observed that the ground pressure modeled under the front and rear shovel tracks as seen in Figure 3-13, that the 1/6 track front and 1/6 track rear sub-graphs matched that of Sharif-Abadi and Joseph (2010), derived from field measurements.

4 California Bearing Ratio (CBR) Test

The chosen research material (broken dolomitic limestone) used in the laboratory tests was provided by Hammerstone Corporation. It is completely crushed and commonly available for the demands of the Athabasca region for over 50 years. Figure 4-1 shows the limestone sample used for the CBR tests. The broken dolomitic limestone hereafter will be referred to as “limestone”.

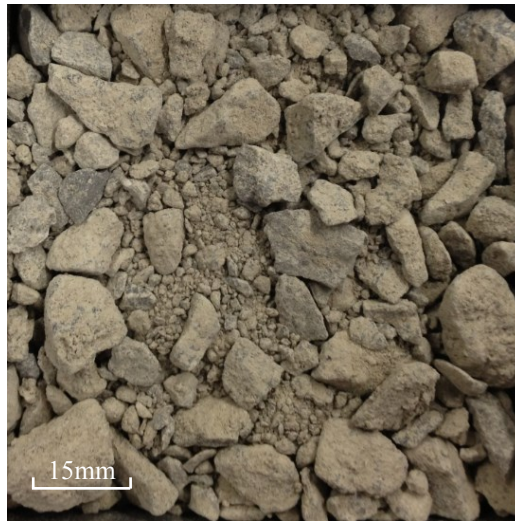


Figure 4-1 Crushed limestone used in laboratory tests

The CBR test was first used by the California Division of Highways in the 1920s and approved by American Society for Testing and Material (ASTM) in 1961. In evaluating the potential strength of research material as a haul road or pad construction material, the CBR test was conducted. A summary of test approach and results in the laboratory are explained below.

4.1 Apparatus and Procedure

First, limestone is compacted in a 6 inch mold to a specific state in accordance with Standard Test Methods for Laboratory Compaction Characteristics of Soil Using Standard Effort (ASTM (2012) D698).

Secondly, surcharge weights was placed on the specimen before applying the load using penetration piston with the rate of 0.05 in/min until 0.5 in or the maximum penetration load available for the machine was achieved. For details, see the Standard Test Method for CBR of Laboratory-Compacted Soils (ASTM (2007) D1883).

Finally, the load reading was recorded and used to create a load-penetration curve. In some instances, the curve may be concave upward initially due to surface irregularities. In such cases the zero datum was adjusted.

The loading apparatus is shown in Figure 4-2. Main components include the loading frame machine and a penetration measuring device. Mold (6 inches), spacer disk and compression tools such as impact ram were used for sample preparation.

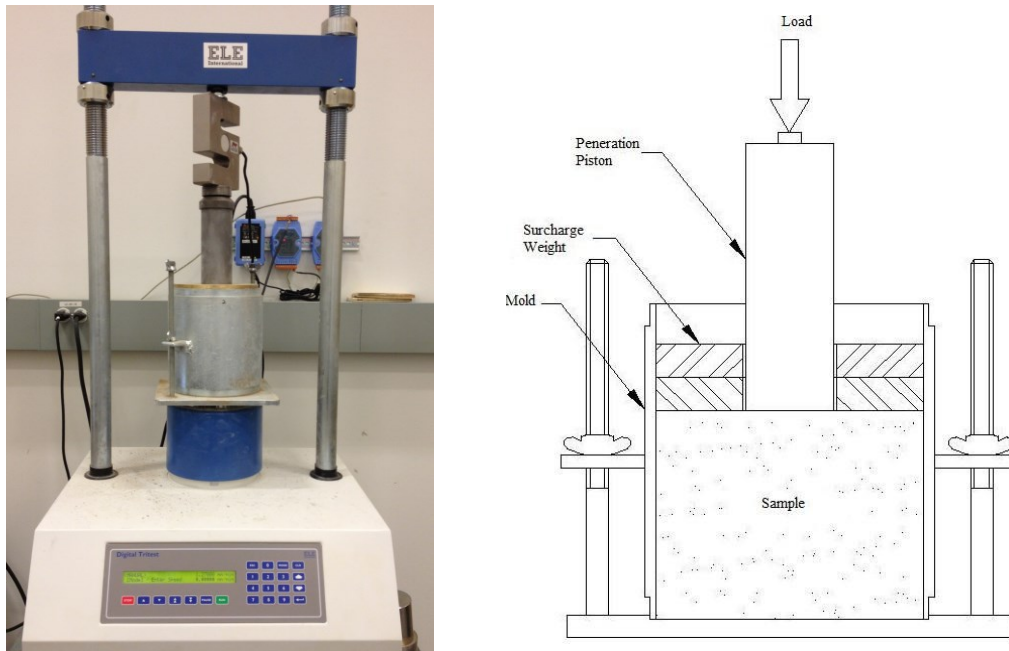


Figure 4-2 CBR loading apparatus

4.2 Results

CBR is expressed as the ratio of the load needed to penetrate 1 in or 2 in of the test material, compared to the load required to penetrate a standard of well-graded

crushed stone multiplied by 100 to give a percentage. The standard stress for crushed standard stone is 6.9 MPa and 10.3 MPa corresponding to 0.1 and 0.2 in penetration respectively. If the penetration observed was less than 0.2 in at the maximum stress, then Equation (4-1) was used to determine the CBR value. When the ratio at 0.2 in (5.08 mm) was greater than that at 0.1 in (2.54 mm), the test was rerun. If the test gave a similar result, Equation (4-2) was applied.

$$CBR_{0.1} = \frac{\sigma_{0.1}}{6.9} \times 100\% \quad (4-1)$$

$$CBR_{0.2} = \frac{\sigma_{0.2}}{10.3} \times 100\% \quad (4-2)$$

The average 0.1" CBR and 0.2" CBR measured values were both considered in the case of testing the laboratory limestone.

A sample CBR stress-deformation curve for the laboratory limestone is indicated in Figure 4-3. The effective stress is the linear portion after adjusting the zero point. As such the predominant parameters and results are listed in Table 4-1.

Table 4-1 Results of limestone CBR test

Offset	0.94 mm	Eff 0.1" $\sigma_{0.1}$ (MPa)	2.03	CBR 0.1"	29.42%
Eff 0.1"	3.48 mm	Eff 0.2" $\sigma_{0.2}$ (MPa)	4.06	CBR 0.2"	39.41%
Eff 0.2"	6.02 mm	Average σ_{avg} (MPa)	3.04	CBR avg.	35.40%

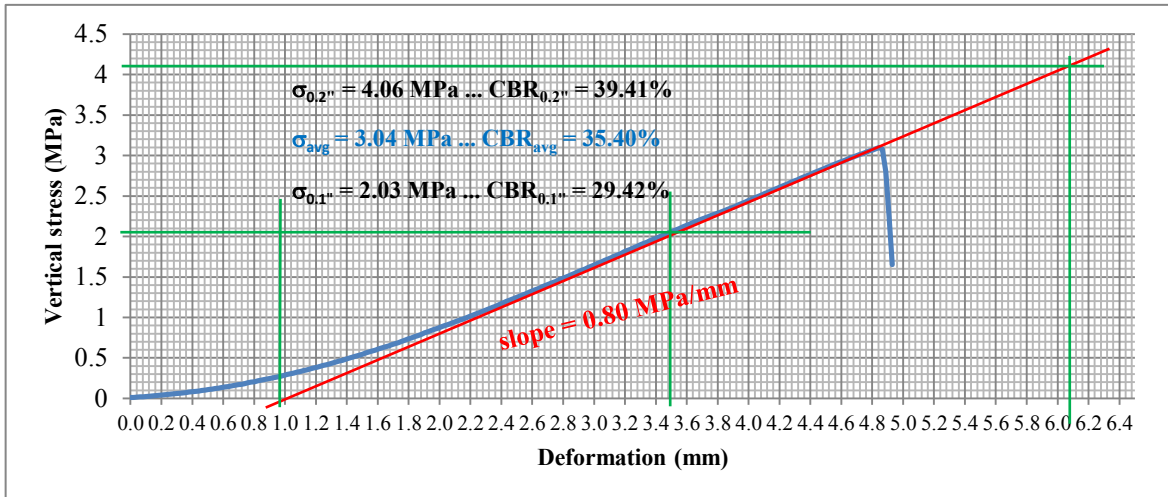


Figure 4-3 Vertical stress-deformation curve from limestone CBR test

4.3 Haul road design

An example is used here to show the application of laboratory limestone in haul road design. Critical parameters contained in a multi-layer haul road design are shown in Figure 4-4. E_i represents the resilient modulus of the i th layer; z and d are the depth and thickness respectively.

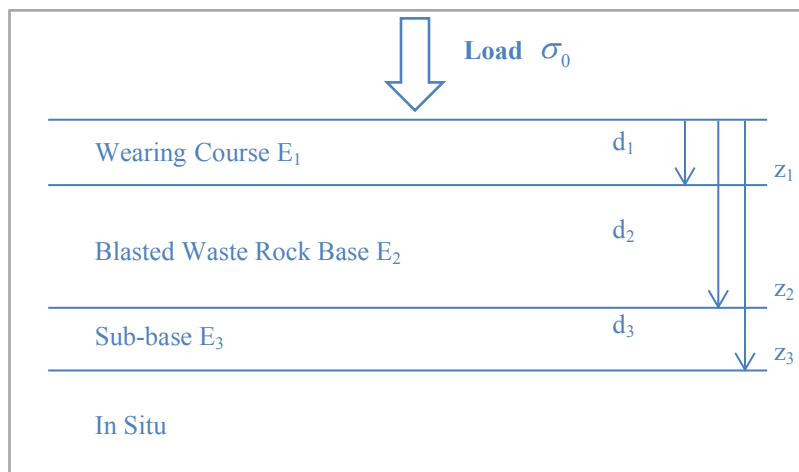


Figure 4-4 Multiple-layer haul road overview

A mining haul truck such as a Caterpillar 797B has a static tire-ground contact area of 1.4 m² where the normal payload with an acceptable (manufacturer) 20% overload results in a tire-ground interaction of 889.5 kPa per tire. The tire

footprint is more akin to a long continuous footing where the tire is in motion. So the “Boussinesq bulb” in literature review (see Figure 2-18) for a long continuous footing is more applicable in analysing a vertical stress distribution by depth under a truck tire. The results of the vertical stress distribution analysis by depth are summarized in Table 4-2. At about 3.5 times the square root of the tire area (4.14 m), the vertical stress is reduced to 15 percent (142.32 kPa). Therefore, the thickness of the material above the in-situ layer should be 4.14 m or more to protect the in-situ material (Joseph, 2002).

Table 4-2 Vertical stress with depth influence under long footing area

Depth (m)	Stress (kPa)	Influence factor	Depth vs. Width
0	889.50	1	0
0.59	756.07	0.85	0.5 B
1.18	622.65	0.7	1.0 B
1.78	453.64	0.51	1.5 B
2.37	311.32	0.35	2.0 B
2.96	231.27	0.26	2.5 B
3.55	173.45	0.195	3.0 B
4.14	142.32	0.16	3.5 B
4.73	104.07	0.117	4.0 B

The stress vs. depth curve is illustrated in Figure 4-5, where a correlation between the two is given by Equation (4-3).

$$\sigma = 857 \exp(-0.4z) \quad (4-3)$$

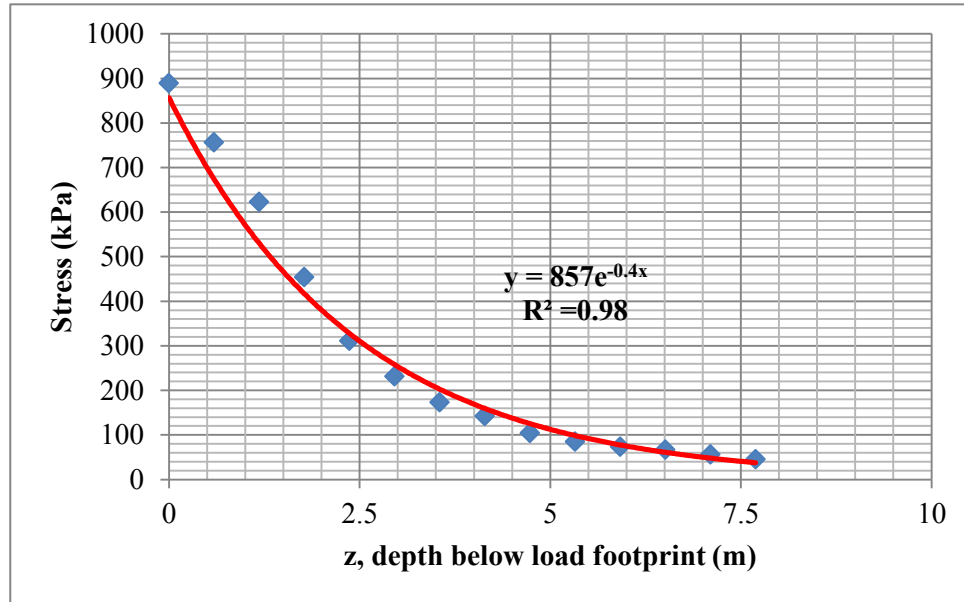


Figure 4-5 Stress versus depth below load footprint

The strain generated in each layer is a function of the material resilient modulus, which is directly proportional to any CBR test values. Among several empirical equations discussed in the literature review, Thompson’s equation was selected for compatibility (Equation (4-4)).

$$M_r = 17.63CBR^{0.64} \quad (4-4)$$

For the multi-layered haul road, Morgan, Tucker & McInnes (1994) and Thompson & Visser (1997) proposed a vertical compressive strain limit; 1750 $\mu\epsilon$ (microstrain) also used for this research. As illustrated in the literature review, a stronger material is used in successive upper layers of a road. Crushed rock material is extensively used as a wearing cap course in road construction (Thompson & Visser, 1997). The limestone crush in Northern Alberta is not as strong as that in United States, of which the CBR value can be 80%. If the laboratory limestone was considered for a wearing cap (CBR value is 35.4%), by varying the thickness of the wearing cap layer (z_1), the CBR value of base material may be targeted for an optimum thickness of any layer and a minimum

CBR for a base material allowing a limiting vertical strain to be maintained. The thickness of layers and the corresponding CBR values have been analyzed and provided in Table 4-3.

Table 4-3 Values of the critical parameters in the haul road construction design

Parameter index	Value	units	Parameter index	units	
Limiting strain	1750	$\mu\epsilon$	CBR		
E ₁ wear	172	MPa	35	%	
E ₂ base	138	MPa	25	%	
E ₃ sub-base	100	MPa	15	%	
z ₁	2.63	m	d ₁	2.63	m
z ₂	3.17	m	d ₂	0.54	m
σ_0	889.5	kPa			
σ_1	299	kPa			
σ_2	241	kPa			
ϵ_1	1744	$\mu\epsilon$			
ϵ_2	1743	$\mu\epsilon$			
z ₃	4.14	m	d ₃	0.97	m
σ_3	164	kPa	total depth	4.14	m
ϵ_3	1640	$\mu\epsilon$			

Maintaining a vertical strain in any layer below the 1750 microstrain limit indicated that the thickness of the limestone should be 2.63 m, in which case, preceding layers can be built with lower CBR value material (25% is strong enough) such as oil sand on a weaker sub-base with CBR less than 15%, which helps in the reduction of overall haul road construction cost. In other words, poorer quality mine waste material can be used.

From these initial analyses, the limestone used for this research was considered to have good load resistance capability and provided good strain resistance. It was

concluded that the laboratory limestone could be applied to build a haul road on weak in-situ conditions or a soft material sub-base.

5 Cyclic Plate Load Tests

Although cyclic plate load tests are time consuming, such tests provide mimicking condition most akin to a shovel track-ground loading system. Hence it was considered necessary to conduct cyclic plate load tests in the laboratory. Three plates of different dimensions were used to investigate a shovel track loading scenario with four cyclic loads applied at three different frequencies to imitate the rocking unload-reload motion of a shovel. Experimental details and results are presented in this chapter.

5.1 Specimens

The same limestone as used for the CBR tests was poured into the containment box with no compaction made in dry conditions. In mine haul road construction, compaction is one of the most critical processes, needed to achieve a high quality surface, performed until no “tracks” of compaction rollers can be seen after 10-15 passes (Thompson & Visser, 1997). However, the plate load test and following analysis deal with loose limestone beyond creating a level surface. This is done to evaluate performance from loose to compacted states.

In assessing material grain size composition, a grading sieve analysis was performed using 0.75, 0.5, 0.25, 0.125 and 0.075 inch sieves to define the particle distribution curve shown in Figure 5-1. The oversize particle sizes range from 12.7 to 24.9 mm. Grain size smaller than 2 mm presented 55 percent by weight.

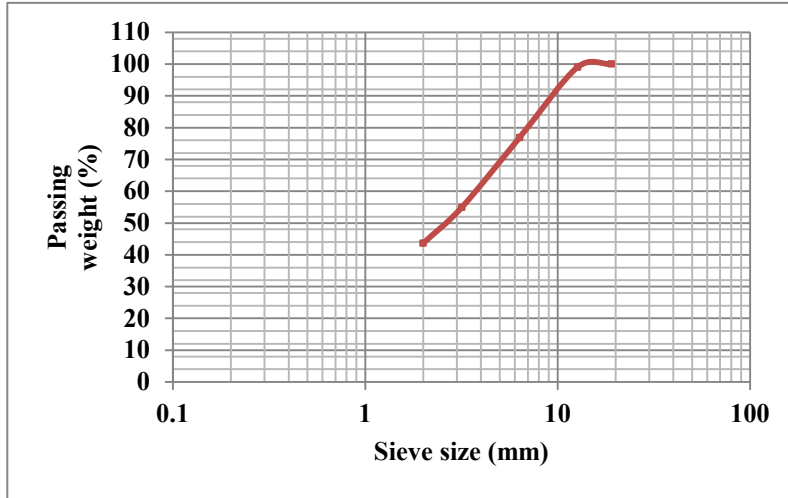


Figure 5-1 Size distribution curve for the limestone material

5.2 Scaling

The mean fragment size (d_{50}) of limestone used in field application is typically around 135 mm. The crushed limestone used in the laboratory tests has a d_{50} of 3 mm derived from the particle size distribution curve in Figure 5-1. This translated to a particle size scaling factor is 45 (135mm/3mm).

The contact track – ground base load balanced area for a P&H 4100C BOSS cable shovel is 31.31 m² per track for a track – ground contact length (L) of 8.92 m and width (B) of 3.51 m. An appropriate scaled laboratory plate area was then calculated via Equation (5-1)

$$SF = \frac{\sqrt{A_{actual}}}{\sqrt{A_{lab}}} \quad (5-1)$$

where SF is the scaling factor of 45, A_{actual} is shovel track-ground contact area, and A_{lab} is the ideal plate area that should be used in the laboratory test to directly mimic the actual shovel track in relation to the limestone crushed material. This translated into an ideal scaled plate area of 0.015 m². Based on this, three

dimensioned plates, spanning this contact area size were designed for the cyclic load tests with areas of 0.01, 0.02 and 0.04 m² respectively.

The L/W aspect ratio of the actual shovel track was 0.39. In an attempt to investigate the influence of loading plate shape as well as remain consistent with the actual shovel track size, the plates were designed as strip, rectangular and square shapes with aspect ratios of 0.325, 0.5 and 1 respectively.

Consequently, when applying loads in the scale cyclic plate load tests, the track – limestone contact pressure was kept the same as experienced by the actual shovel in field loading conditions, as analysed previously from field data.

Details of the experimental design are explained in the following sections.

5.3 Apparatus

5.3.1 MTS

The material Test System (MTS) is a hydraulic cyclic loading press to 250,000 lb capacity used to determine the performance and cyclic durability properties of high-strength materials. The servo hydraulic MTS is used to deliver cyclic forces to the three differently shaped and dimensioned plates used here for the cyclic plate load tests. The main components of MTS are shown in Figure 5-2.



1. High-accuracy Linear Variable Differential Transducer (LVDT)
2. Hydraulic Control
3. Hydraulic Grip Supply
4. Load Frame Base (T-Slot)
5. Precision Force Transducer (Actuator-mounted)
6. High-performance MTS Actuator

Figure 5-2 Diagram of MTS

Six hydraulic pumps each with 30 gpm flow provide 2046 liter/min flow to the actuator at the same time. The loading capacity is 1000 kN with a frequency maximum of 10 Hz. A load cell installed on the crosshead measures the load applied. A LVDT can sense displacement to 0.001mm and transfer signals to computer software to record displacement. The recording frequency was set at 20 Hz.

5.3.2 Box

The configuration of the metal box used to contain the limestone samples is shown in Figure 5-3. The outer length, width, and height are 0.61 m, 0.61 m, and 0.41 m respectively with wall thickness of 0.006 m. Length was designed at three times the loading plate longest side to minimise impact from the box wall . The depth was set deeper than two-thirds of the depth of influence. As per the literature review, the influence depth was $3\sqrt{A}$ (0.61 m). The dimensions of the box in minimising the effect of box edges provided a semi-infinite half-space which would be modeled (later chapter). The box was fixed on the load frame base of the MTS.

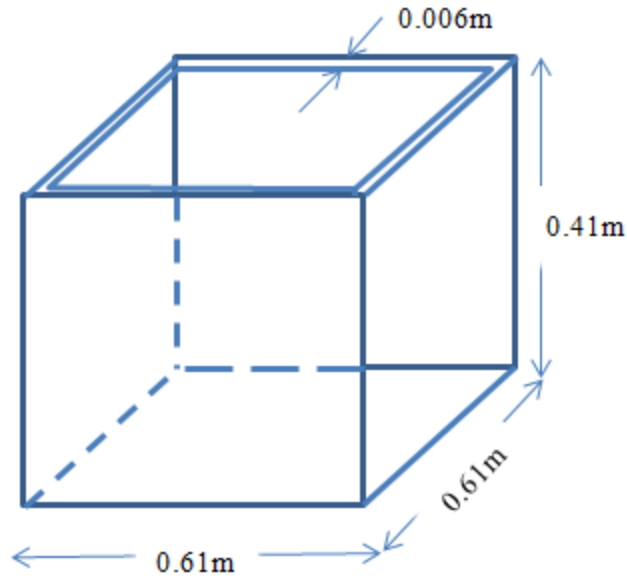


Figure 5-3 Configuration of steel box

5.3.3 Plates dimensions

The dimensions of three plates are listed in Table 5-1, with aspect ratios of 1, 0.5, and 0.325 for plates labelled 1, 2 and 3. The square plate (aspect ratio of 1) is more akin to the pad shape for an open-pit in-pit crusher, while the rectangular (aspect ratio of 0.5) and strip (aspect ratio of 0.325) plates are more comparable with shovel tracks and truck tire footprints. For testing, each plate was connected directly to the loading transducer of the MTS frame.

Table 5-1 Plates dimensions for cyclic plate load tests

Plate number (shape)	Plate1 (square)		Plate2 (rectangular)		Plate3 (strip)	
Units	inch	m	inch	m	inch	m
Length	8	0.20	8	0.20	8	0.20
Width	8	0.20	4	0.10	2.63	0.07
Area (m ²)	0.04		0.02		0.01	

5.4 Set up and Procedure

Before running the tests, some boundary condition parameters need to be set up. Based on the analysis of ground pressure under a shovel track shown in chapter 3, the cyclic load varies from 100 to 600 kPa. As loads are applied onto the loose material, 100 kPa only produces an initial compaction. So the load levels were set for a test range from 200 to 800 kPa by 200 kPa intervals. The entire loading cycle can be viewed in two parts: a ramp-up (initial loading) followed by a cyclic loading portion joint by a constant loading phase, as illustrated in Figure 5-4. It can be seen in Figure 3-13, that during initial loading, the pressure ramps up to a maximum load state at a rate of 8~15 kN/m. The loading rate used in the laboratory was investigated as 2.5, 8, and 15 kN/m. Loading frequencies of 0.016, 0.033, and 0.066 Hz correspond to 1 min, 30 seconds and 15 seconds cycle time, accounted for the fact that digging times vary from 30 to 45 seconds. Each plate then was tested for four load levels and three cyclic frequencies. With three plates, a total of 36 tests were thus conducted. The test procedure has conducted as follows

1. Divide the sample material into 36 piles;
2. Fill the containment box with a new limestone pile for each test;
3. Adjust the hydraulic system, allowing the plate to almost touch the surface of the material;
4. Run the system at a given frequency and loading rate and record the applied force and displacement experienced by the plate;
5. After 250 cycles, stop the machine, raise the plate and prepare the next run.

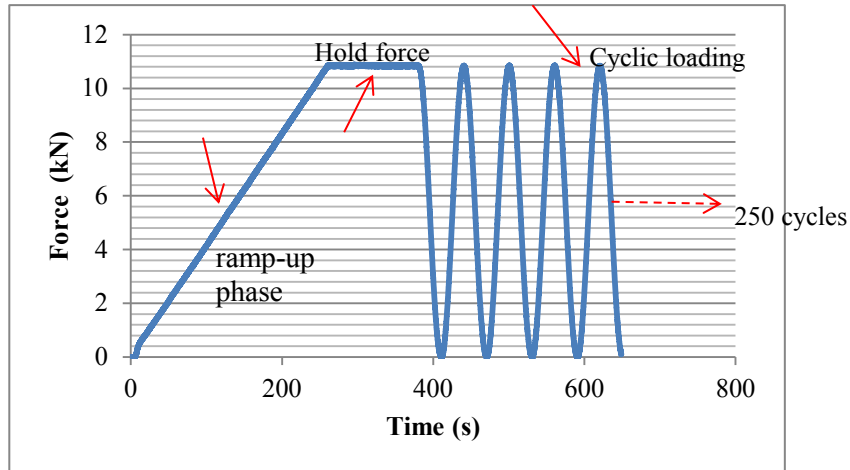


Figure 5-4 Force versus time during ramp-up, hold and 4 cycles for plate 3 at 800 kPa and 0.016 Hz

5.5 Results

The MTS system recorded force, deformation and time at 20 Hz. Taking the 800 kPa, 0.016 Hz cyclic loading test as an example: The test took 4 hours to complete 250 cycles regardless of ramp up phase, generating thousands of data points in the exported results. Data processing included identifying outlier points before plotting relationship, making it easier for trends or relationships to captured and analyzed for discussion in the following section. In this section, as an example, the results of plate 3 (strip shape) under 800 kPa at 0.016 Hz test are shown.

Figure 5-5 shows the full view of force-deformation curve (hereafter, reviewed as F-D curve). The following observations were made:

1. As predicted, when a force is initially applied to the limestone sample, 2kN load (150 kPa pressure for the strip plate, one fourth of the total load), almost half of total deformation is experienced. This is because the material dumped in the box with no compaction is compacted in the initial process. Barksdale (1972) discerned that the degree of compaction would affect the stiffness of a granular material. An increase in the degree of compaction results in a stiffness increment. In addition, there is no adhesion between limestone

particles; so when load initially applied, the stiffness is quite low. Deformation was generated relatively easily in this region named the pre-loading region;

2. After pre-loading and before cyclic loading, the F-D curve was close to linear; the slope of the F-D pre-loading curve will be discussed in a following chapter;
3. By number of cycles, the deformation per cycle decreased. In the graph this principle manifest as the curve became more intensive with progressive deformation;
4. Compared with the deformation occurred in the ramp-up phase, 250 loading cycles produced 15 mm total deformation, accounting for one third of the total deformation.

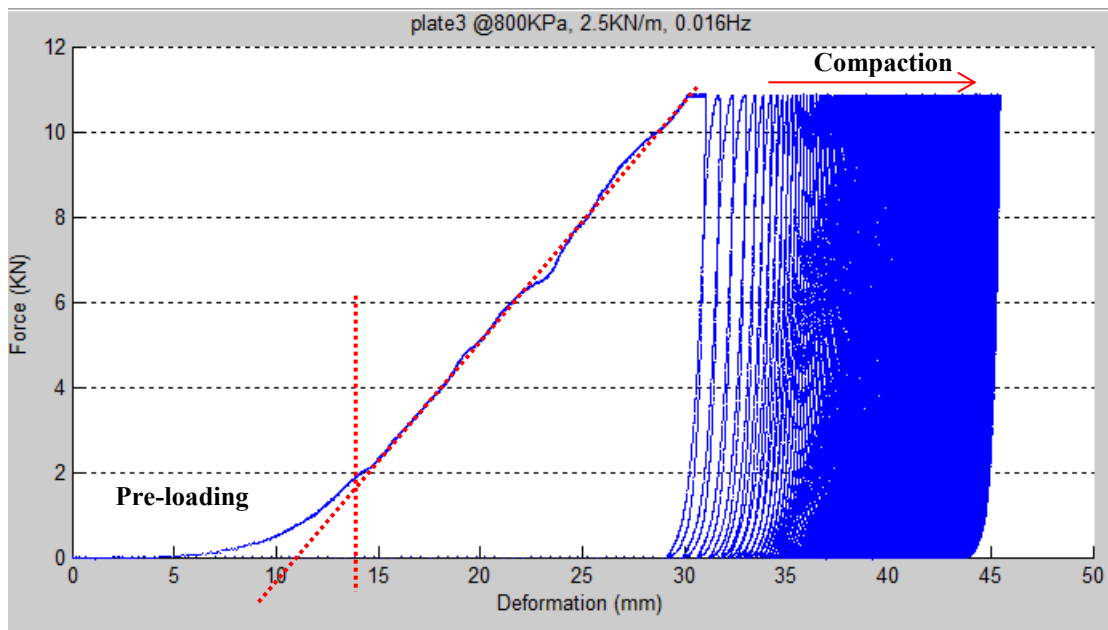


Figure 5-5 F-D curve for plate 3 at 800 kPa and 0.016 Hz

With increasing number of cycles, the unload-reload curves converge, so the F-D curve was magnified. First and last few cycles of the F-D curve are shown in Figure 5-6 and Figure 5-7 respectively.

For the first few cycles, the total deformation comprises elastic and plastic deformation components. As highlighted in literature review, δ_T is the pseudo-elastic deformation, expressed as Equation (5-2).

$$\delta_T = \delta_e + \delta_p \quad (5-2)$$

where $\delta_T, \delta_e, \delta_p$ are total deformation, elastic deformation and plastic deformation per cycle respectively. The elastic deformation is greater than its counterpart. The plastic deformation decreases with increasing number of cycles ($p_1 > p_2 > p_3$). For the last few cycles, the plastic deformation is already very small. Subsequent cyclic curves almost overlap previous ones as exhibited in Figure 5-7.

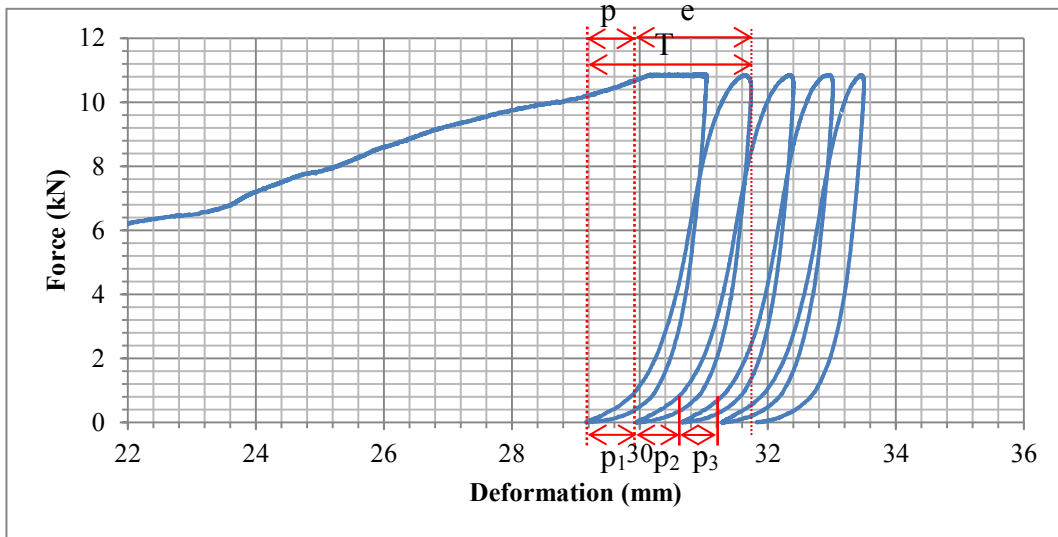


Figure 5-6 F-D curve for the first few cycles

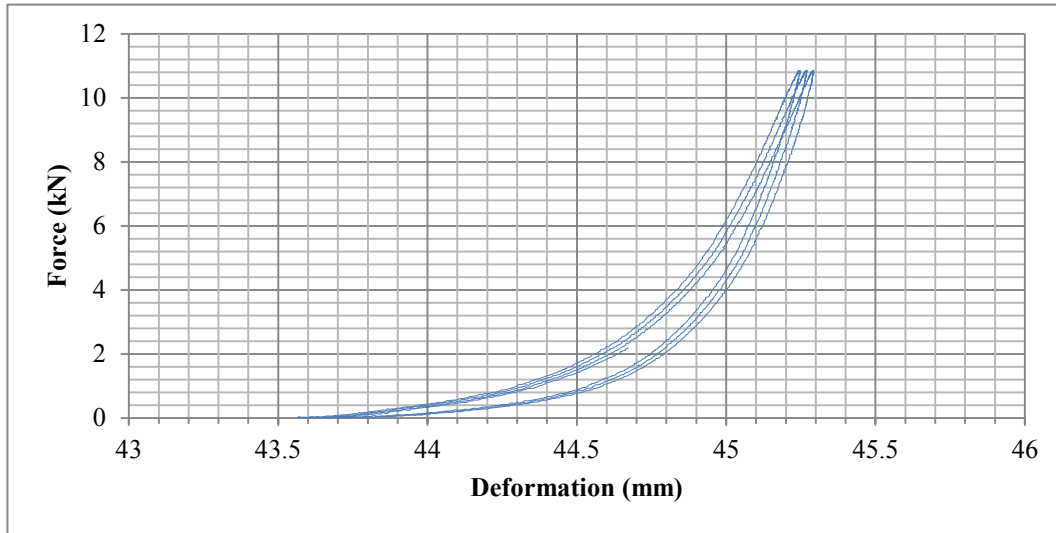


Figure 5-7 F-D curve for the last few cycles

For a better understanding of the material deformation path, a deformation-time curve (referred to as D-T curve thereafter) was plotted (Figure 5-8). After climbing to 30 mm in the ramp-up phase, deformation begins to take on a short wave cycle overall increasing under cyclic loading. If the data between “crest” and “trough” is ignored, the D-T curve has a more global view (Figure 5-9). Wave crests in Figure 5-8 represent total deformation points while trough represents irrecoverable deformation.

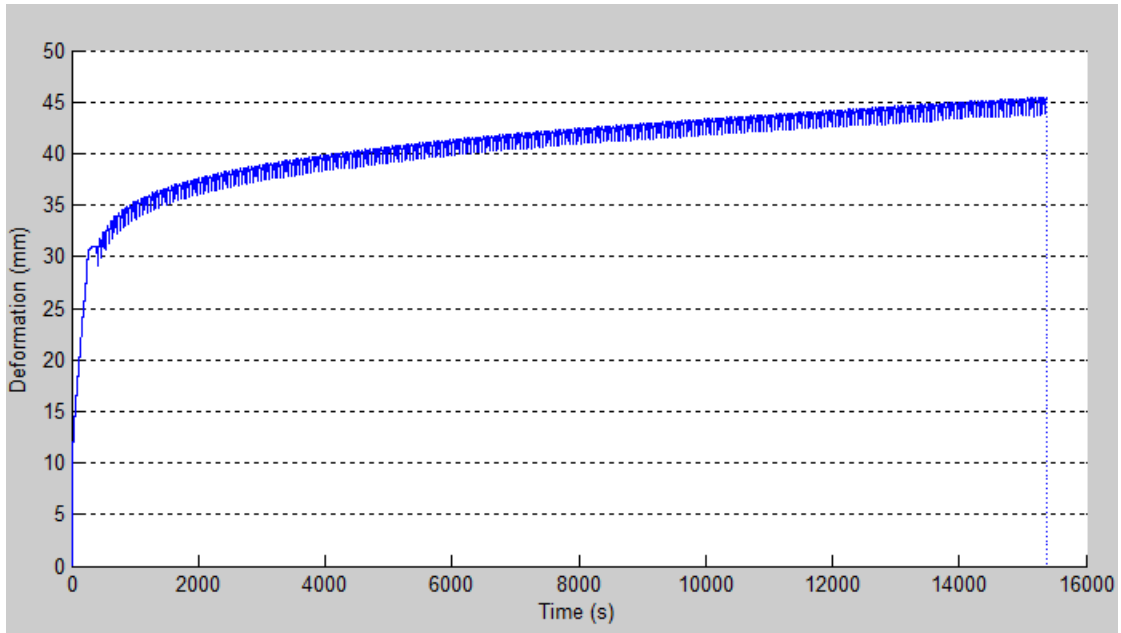


Figure 5-8 D-T curve of plate 3 for 800 kPa and 250 cycles

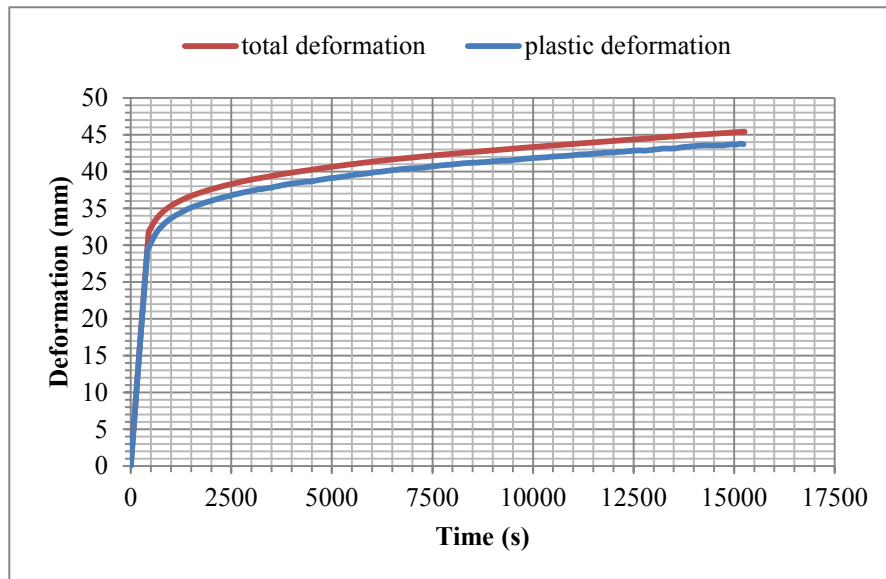


Figure 5-9 D-T curve of Figure 5-8 after screening points

Code used for the data analysis in Matlab are provided in Appendix V.

6 Discussion

On the basis of the results acquired from the cyclic plate load tests, the responses of the material in the monotonous loading phase and the cyclic loading phase are quite different. Distinct analytical methods were implemented for the different loading phases. In this chapter, the results of the initial loading and cyclic loading events are discussed separately.

6.1 Initial loading

Figure 6-1 illustrates the force-deformation curve of plate 3 under 200, 400, 600, 800 kPa cyclic load at the loading rate of 2.5 kN/m. After pre-loading, the curves ramp up linearly with the exception of 200 kPa test. This latter amount of load is just sufficient for pre-loading. The slopes of the three parallel red dashes in Figure 6-1 represent the same force stiffness for 400, 600 and 800 kPa. In order to normalize the effect of the plate area, the force stiffness was divided by plate area, which generates a pressure stiffness k , defined as stress per unit deformation (Sharif-Abadi, 2006; Sharif-Abadi & Joseph, 2010).

The area of plate 3 is 0.01 m^2 . So the pressure stiffness was discerned as $k = 42.1 \text{ kPa} / \text{mm}$. The force-deformation curves before cyclic loading were plotted in Figure 6-2 and Figure 6-3 for plate 2 and 1 respectively. Both plates exhibited similar characteristics. The areas of plates 2 and 1 are 0.021 m^2 and 0.041 m^2 respectively; generating pressure stiffness as of $k = 96.9 \text{ kPa} / \text{mm}$ and $k = 112.1 \text{ kPa} / \text{mm}$ respectively.

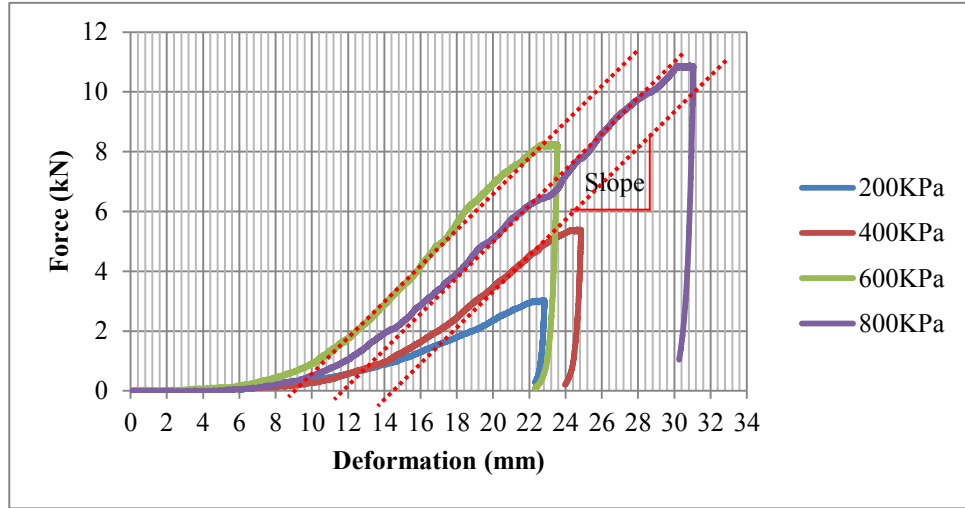


Figure 6-1 Force-deformation curve for plate 3 under 200, 400, 600, 800 kPa cyclic load

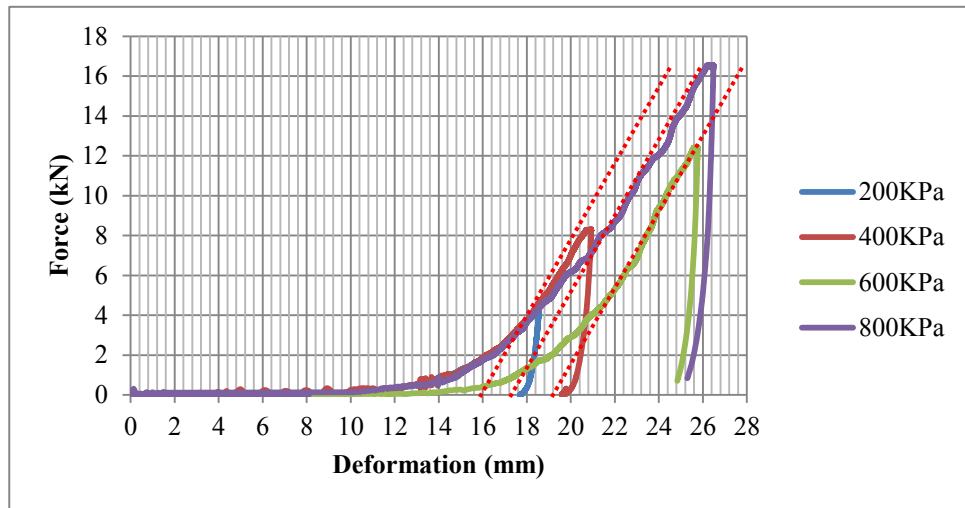


Figure 6-2 Force-deformation curve for plate 2 under 200, 400, 600, 800 kPa cyclic load

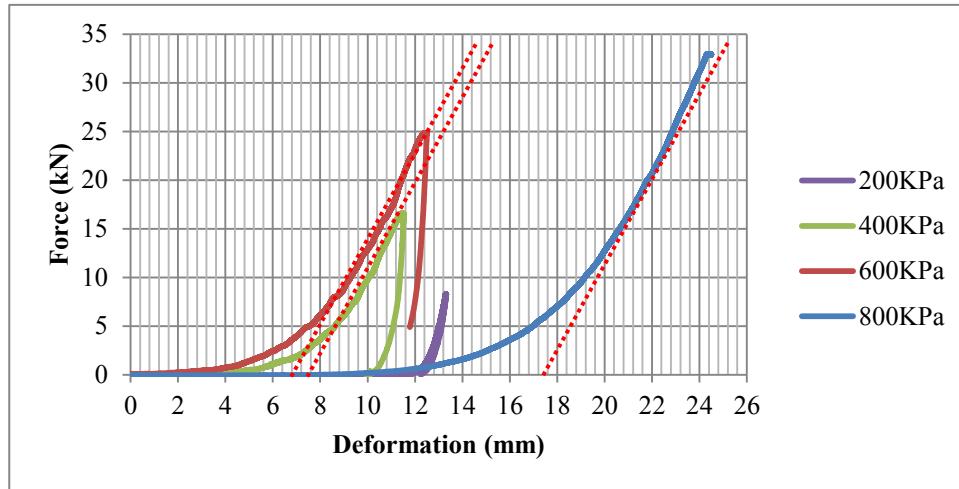


Figure 6-3 Force-deformation curve for plate 1 under 200, 400, 600, 800 kPa cyclic load

Although in considering pressure stiffness the plate areas were normalized, the pressure stiffness discerned was different by plate shape. With this in mind, the parameter of width over length ratio, $\frac{W}{L}$ (referred to as the aspect ratio in chapter 5.3.3) was brought into consideration and the relationship between pressure stiffness as a function of width over length ratio was explored. In addition, Table 6-1 summarize the pressure stiffness variation of the three plates investigated with different loading rate. Figure 6-4 provides a more visible view of the results.

Table 6-1 Pressure stiffness and width over length ratio of three plates

Plate description	W/L ratio	k (kPa/mm)		
		2.5 kN/m	8 kN/m	15 kN/m
Plate 1 (square)	1	111.12	116.79	120.43
Plate 2 (rectangular)	0.5	96.88	100.26	102.71
Plate 3 (strip)	0.328	42.07	47.54	51.55

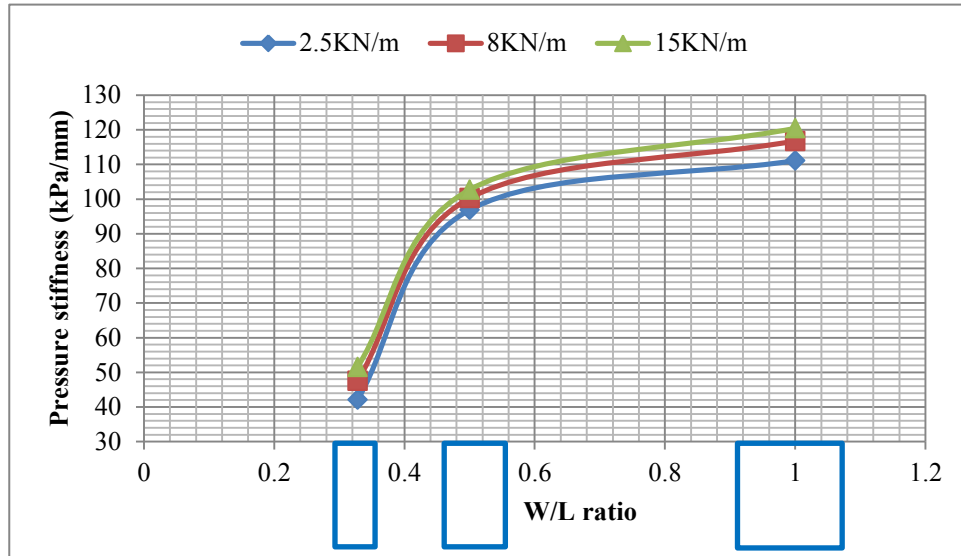


Figure 6-4 Pressure stiffness versus width over length ratio for three plates displayed as a function of loading rate

It appears that the higher the aspect ratio of the plate, the more difficult it is to generate deformed ground. This phenomenon is somewhat attributed to behavior of unbound limestone particles, their resistance to penetration, which will be corroborated in section 6.2.3.3. The shape of ultra-class mining equipment footprints become significant, impacting equipment maintenance and ground stability concerns. With an increase of loading rate, the pressure stiffness increases, but the difference is very small.

6.2 Cyclic loading

6.2.1 Stress-deformation response

6.2.1.1 Global stiffness variation

As mentioned before, the data collected in the cyclic loading phase was filtered to receive outlying data. Table 6-2 now shows an example of the “unload starting points” and “reload starting points” for plate 3 for 10.85 kN (800 kPa) cyclic load testing at 0.016 Hz frequency.

Table 6-2 Filtered data series during cyclic loading

Unload starting points			Reload starting points			Number of Cycles
Force	Displacement	Time	Force	Displacement	Time	
kN	mm	s	kN	mm	s	
10.85	31.64	440.64	-0.01	29.17	411.26	1
10.86	32.35	500.85	-0.03	29.95	471.42	2
10.86	32.96	560.91	-0.02	30.67	531.48	3
10.84	33.47	621.07	-0.01	31.29	591.29	4
10.85	33.86	680.43	-0.01	31.82	651.25	5
...
10.86	45.38	15141	-0.01	43.74	15111	246
10.86	45.40	15201	-0.00	43.79	15171	247
10.84	45.42	15262	0.01	43.71	15232	248

The global stiffness (k_g) in cyclic loading phase is defined as the ratio of stress to deformation between “unload starting points” and “reload starting points” per cycle. Expressed graphically, it is the secant slope of the stress-deformation curve between lowest and highest points per cycle.

Figure 6-5 shows that global stiffness increases with increasing number of cycles before converging to a constant value. For different cyclic loads, the converged constant value varies. This is because the stress-deformation curve of limestone is nonlinear (Gonzalez, Saleh, Ali & Gribble, 2007). Larger stress results in a larger secant slope. So stress increases exponentially with deformation, which can also be seen in Figure 5-6.

For the 200 kPa and 400 kPa loading cycles, several individual cycles (circled) show the global stiffness drops suddenly and then recovers. This phenomenon is more common for low load level curves. It is speculated that for relative low load

tests, deformation is usually small. Only the particles near the surface at the plate-ground contact area disturbed. In generating low lateral stresses, relative displacement occurs easily among limestone particles. In particle repositioning, the confining stress from the surrounding particles and the previously stable state disappears, leading to a stiffness decline. This “slip” then ceases and a new balance condition is established. Verification of this assumption is illustrated in section 6.2.3.3.

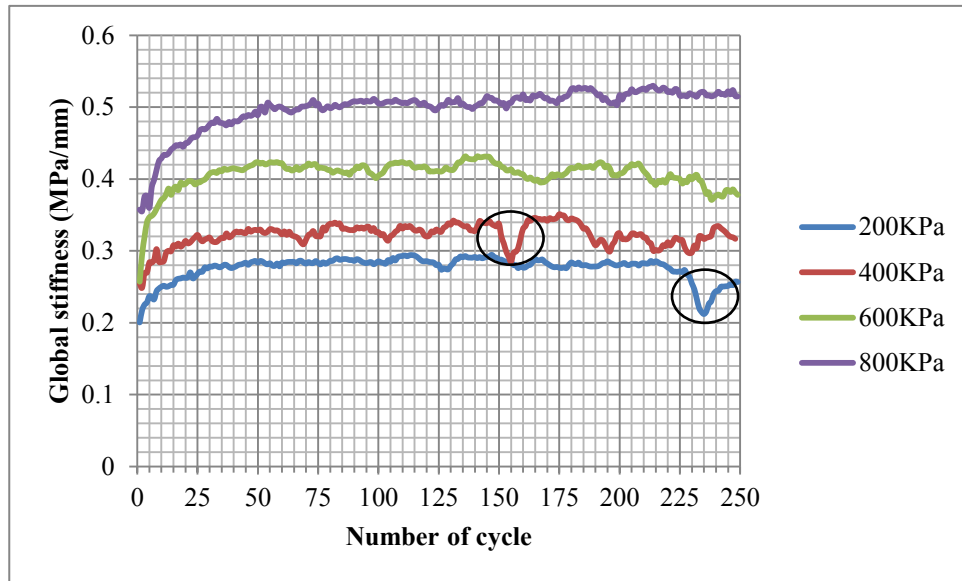


Figure 6-5 Global stiffness versus number of cycles for plate 2 at 200, 400, 600 and 800 kPa and 0.016 Hz frequency

Figure 6-6 indicates the effect of cyclic frequency on global stiffness. For a set cyclic load, the global stiffness converges independent of frequencies.

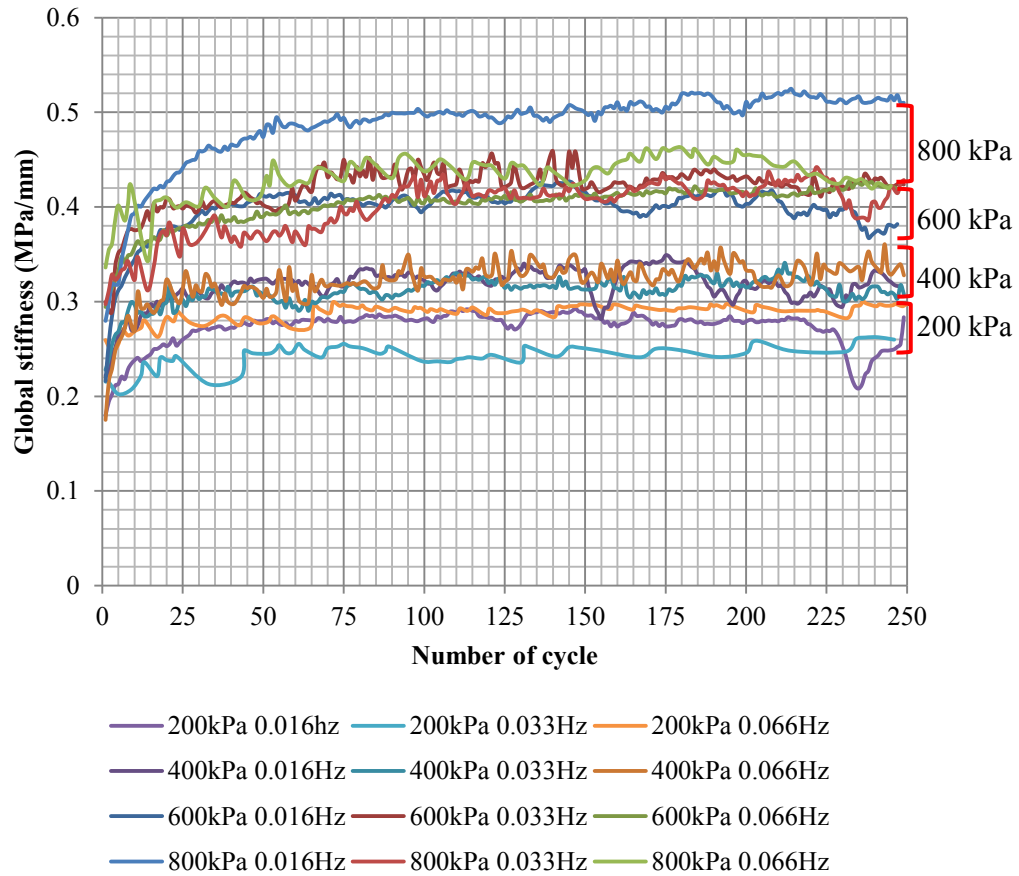


Figure 6-6 Global stiffness versus number of cycles for 4 load levels and 3 frequencies of plate 2

6.2.1.2 Resilient stiffness

Based on the previous analysis, the global stiffness converges to a constant value after several cycles. This value reflects the resilient ability of the broken material to resist external loads. It is hence called the “resilient stiffness (k_r)” in the research. To investigate resilient stiffness of laboratory limestone at any load level, nonlinear stress-deformation curves of limestone were evaluated as follows.

First, “resilient stiffness” at 200, 400, 600 and 800 kPa load levels were calculated. An average of the global stiffness after 150 cycles excluding (slip) “subsidence points” was deemed the resilient stiffness for a specific load level. Table 6-3 lists the values for the three plates and three frequencies tests.

Table 6-3 Resilient stiffness determination for three plates

plate 1			Stress level (MPa)			
			0.2	0.4	0.6	0.8
Resilient stiffness (MPa/mm)	Frequency (Hz)	0.016	0.189	0.270	0.340	0.402
		0.033	0.179	0.277	0.329	0.410
		0.066	0.177	0.262	0.334	0.412
	Max		0.189	0.277	0.34	0.412
Deformation (mm)			1.059	1.442	1.763	1.944
plate 2			Stress level (MPa)			
			0.2	0.4	0.6	0.8
Resilient stiffness (MPa/mm)	Frequency (Hz)	0.016	0.284	0.349	0.427	0.499
		0.033	0.221	0.341	0.417	0.442
		0.066	0.247	0.361	0.427	0.463
	Max		0.284	0.361	0.427	0.499
Deformation (mm)			0.705	1.109	1.405	1.603
plate 3			Stress level (MPa)			
			0.2	0.4	0.6	0.8
Resilient stiffness (MPa/mm)	Frequency (Hz)	0.016	0.366	0.294	0.507	0.498
		0.033	0.313	0.369	0.504	0.515
		0.066	0.247	0.450	0.478	0.575
	Max		0.366	0.450	0.507	0.575
Deformation (mm)			0.546	0.889	1.184	1.391

Second, given that stiffness is effectively independent of cyclic frequency, tests by frequencies were treated as parallel tests. The greater the resilient stiffness is, the closer the material approaches a stable state. Hence the maximum stiffness was selected.

Thirdly, assuming deformation commenced from a zero datum, deformation at 200, 400, 600 and 800 kPa was determined via Equation (6-1).

$$\delta = \sigma / k_r \quad (6-1)$$

where δ is deformation (mm) and σ is the applied stress (MPa). The results are reflected in Table 6-3.

Finally, the stress-deformation relationship is plotted, as shown in Figure 6-7.

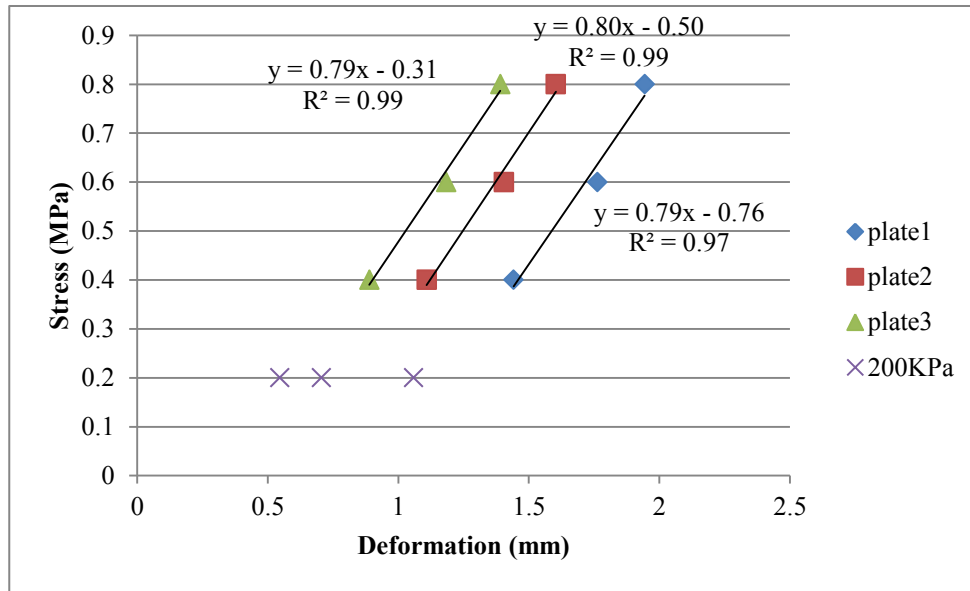


Figure 6-7 Stress-deformation curve approximated by resilient stiffness at different load level

Neglecting the points generated at 200 kPa stress (Figure 6-7) (i.e. eliminating the interference of near surface material low loading stress-deformation response), it is interesting to see that the stress-deformation curve is linear with a slope of 0.8 MPa/mm which is effectively the same for the three plates and equals the slope of the stress-deformation curve previously calculated in the CBR test. As reflected by this research, the cyclic plate load test is not only time consuming but also costly due to the requirement of a large quantity of material and laboratory apparatus, it is therefore much easier to conduct a basic and quick test like a CBR test. Therefore it can be concluded that laboratory test reflects the same pressure stiffness as seen by the accepted CBR, so we can use the laboratory results and CBR can be applied to predict resilient properties of crushed rock such as limestone under cyclic loading, by inverting the analysis above.

6.2.2 Deformation

Figure 6-8 provides a plot of total and plastic deformation respectively versus number of cycles for plate 3, at 0.066 Hz frequency and different loads. The trend of the curves is in general akin to a logarithmic form neglecting the initial deformation variations, the latter of which is a result of different initial loading. The material deforms more under higher load level application. The gap between total and plastic deformation (elastic deformation) remains essentially the same with increasing number of cycles and has a positive correlation with load level. For unbound broken materials, the rebound behavior is a result of confining stress induced deformation recovery which will be explained in section 6.2.3.3.

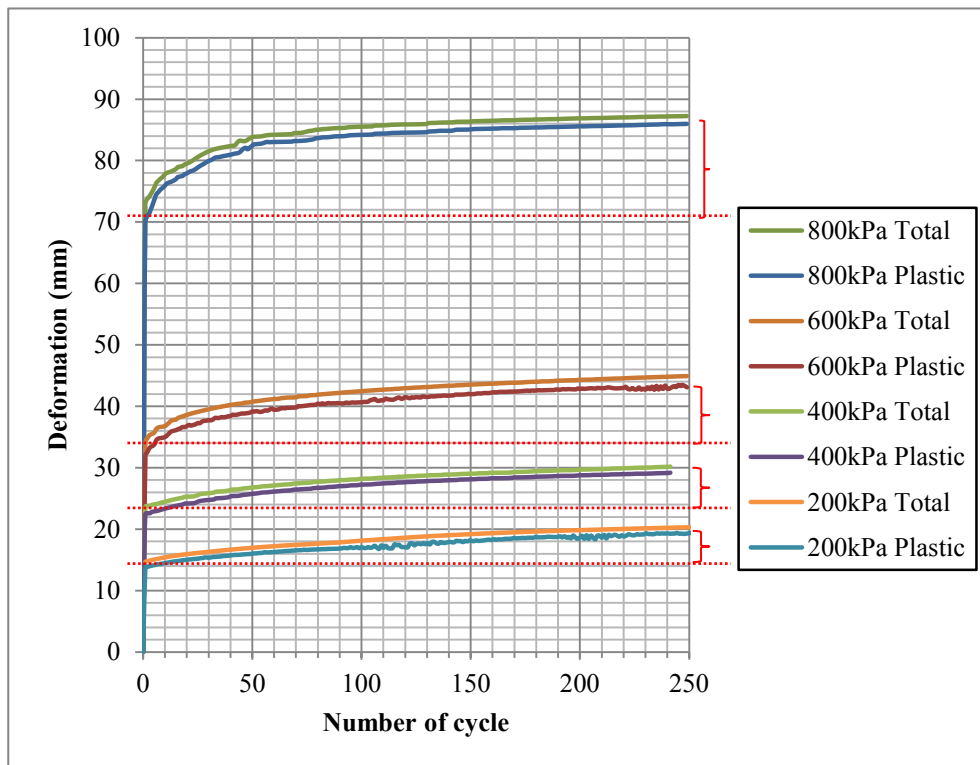


Figure 6-8 Deformation versus number of cycles for plate 3, 0.066 Hz under different load levels

The deformation versus number of cycles for plate 3 at 800 kPa by frequency is presented in Figure 6-9. Elastic deformation by frequency is essentially the same. This corroborates the previous analysis that resilient stiffness is independent of

frequency. However the effect of frequency on total deformation was not discernable from this graph.

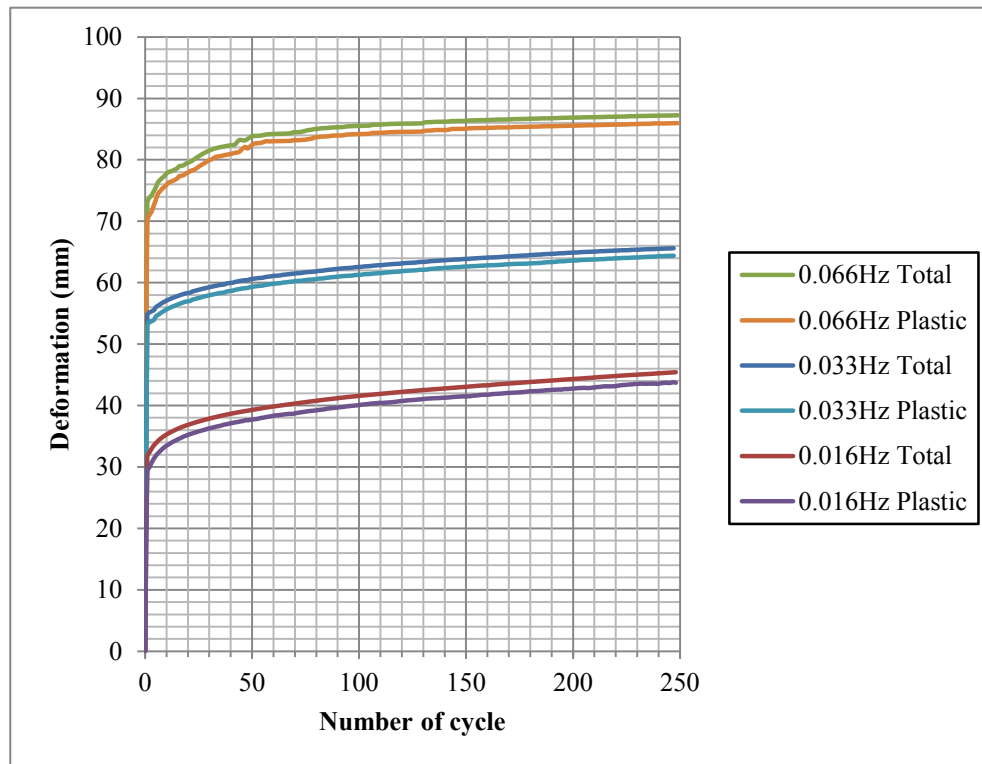


Figure 6-9 Deformation versus number of cycles for plate 3, 800 kPa at different frequencies

6.2.2.1 Plastic deformation per cycle

Plastic deformation generated per cycle decrements with increasing number of cycles, demonstrates that the material gradually approaches a relative stable state. Plastic deformation versus number of cycles for plate 1 under 200, 400 600 and 800 kPa stress at different frequencies is demonstrated in Figure 6-10. From this graph, there is no evidence to indicate at which frequency the plastic deformation converges more quickly. After around 100 cycles, unrecoverable deformation in each cycle for all tests is less than 0.05 mm.

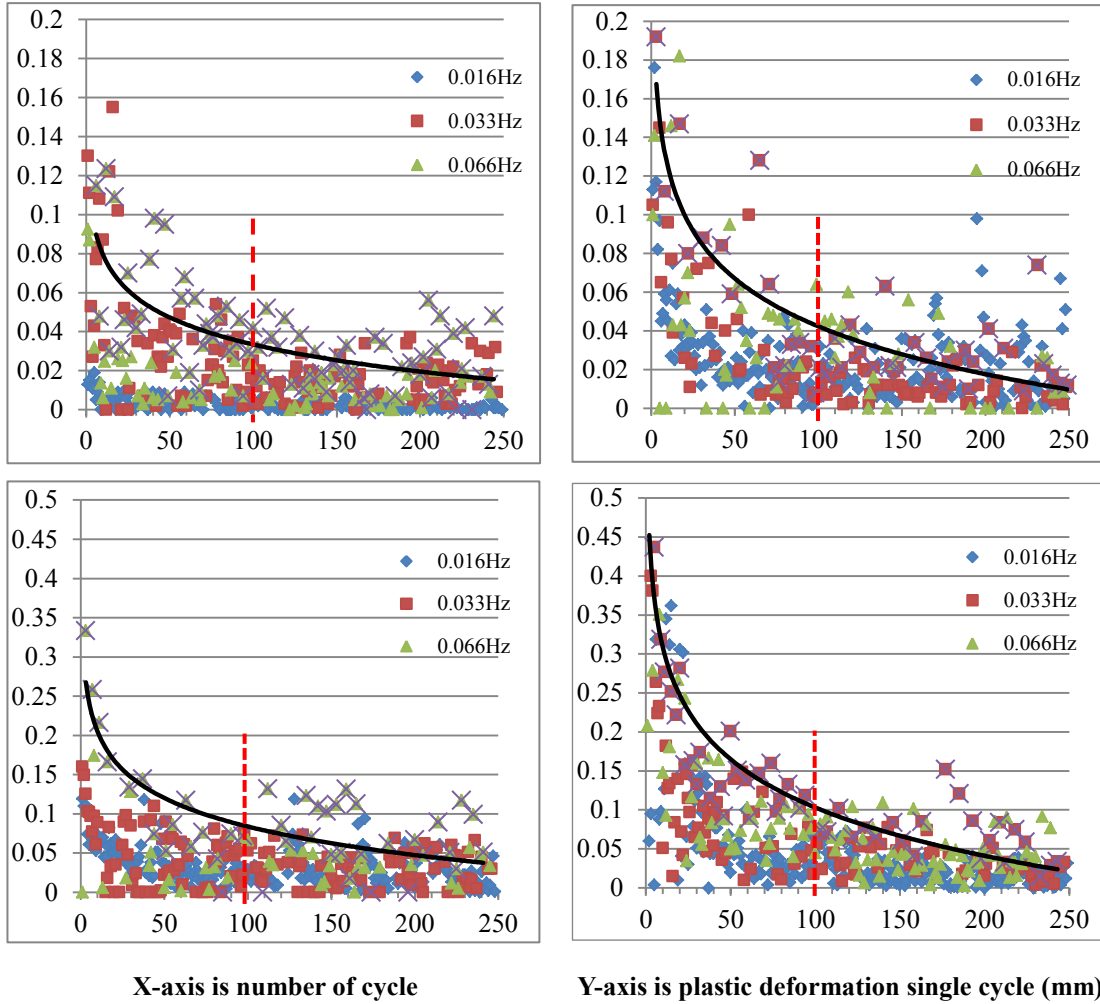


Figure 6-10 Plastic deformation per cycle versus number of cycles for plate 1 at different load and frequency conditions within an envelope of response

6.2.2.2 Total deformation versus number of cycles

The total deformation experienced is the sum of the accumulated plastic deformation and elastic deformation. It is evident from Figure 6-9 that there is little difference in elastic and plastic deformation for frequencies between 0.016 Hz and 0.066 Hz, the total deformation was considered independent of the effect of frequency variation. An average of total deformation by frequency versus number of cycles is generated below (Figure 6-11, Figure 6-12 and Figure 6-13). Furthermore, the zero datum was adjusted for comparison purposes.

A good correlation was found between total deformation (D_c) in the cyclic loading phase versus number of cycles (N). The equation may be expressed in Equation (6-2).

$$D_c = a \ln(N) - b \quad (6-2)$$

where a and b are coefficients and $N \geq 4$. The units of deformation (D_c) are millimetres.

In terms of plate 3, $\frac{W}{L}$ equals to 0.328; the ranges of coefficients a and b were $1.0812 \leq a \leq 2.7864$ and $1.8425 \leq b \leq 3.6777$.

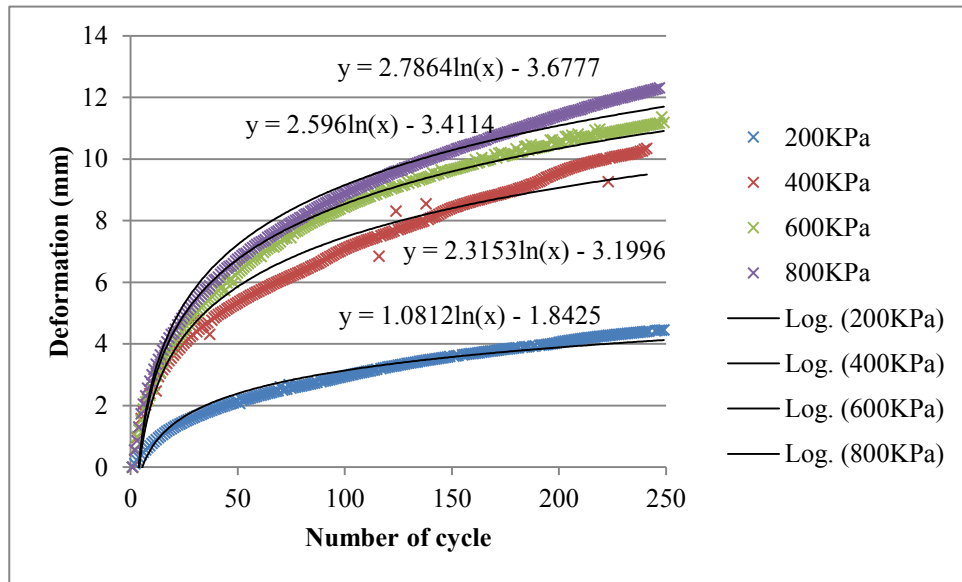


Figure 6-11 Deformation versus number of cycles for plate 3

For plate 2 whose width over length ratio ($\frac{W}{L}$) is 0.5; the ranges of coefficients a and b were $[0.8308, 2.6183]$ and $[0.9637, 3.5598]$.

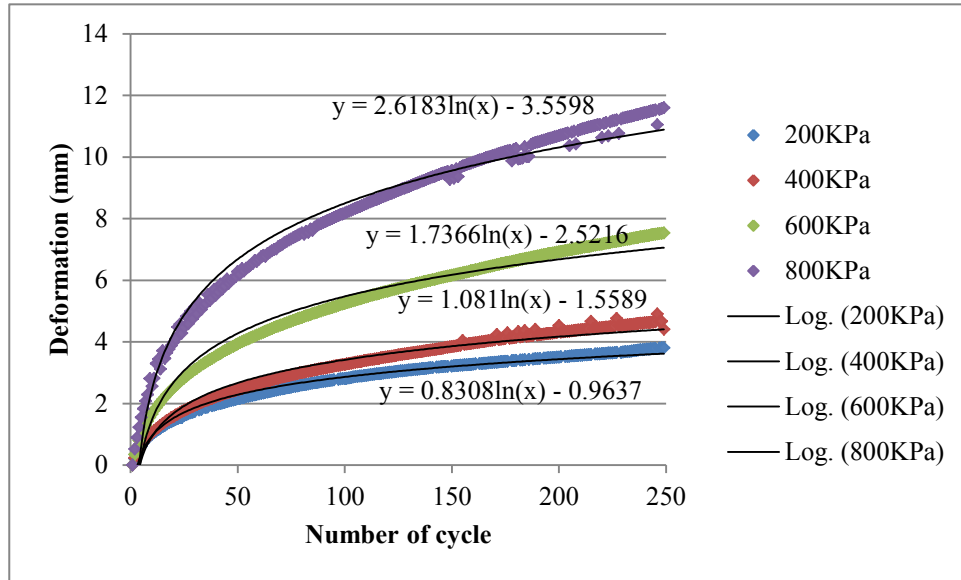


Figure 6-12 Deformation versus number of cycles for plate 2

For plate 1 with an aspect ratio of 1; coefficient a ranged from 0.4172 to 2.3032 and b varied from 0.6516 to 2.9428.

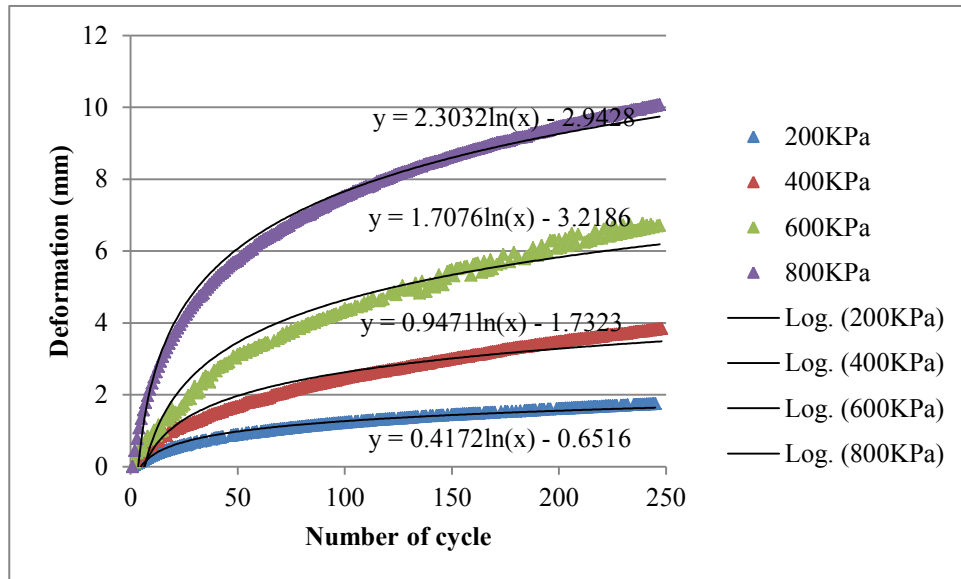


Figure 6-13 Deformation versus number of cycles for plate 1

6.2.2.3 Coefficient estimation

It is therefore understood that a and b are not only related to load level but also a function of plate shape. Furthermore, their correlations seem monotone, which is a multiple linear regression issue. Matlab was thus used to estimate a and b ,

demonstrated in Equation (6-3) and (6-4), where the confidence interval and statistical results are appended in Appendix VI.

$$a = 0.88 - 1.08\left(\frac{W}{L}\right) + 2.97(\sigma) \quad (6-3)$$

$$b = 1.17 - 1.04\left(\frac{W}{L}\right) + 3.8(\sigma) \quad (6-4)$$

It's worth noting that the unit of σ is MPa, therefore Equation (6-2) can be expressed as the expansion:

$$D_c = \left\{ 0.88 - 1.08\left(\frac{W}{L}\right) + 2.97(\sigma) \right\} \cdot \ln(N) + 1.04\left(\frac{W}{L}\right) - 3.8(\sigma) - 1.17 \quad (6-5)$$

6.2.2.4 Verification

Sample data was randomly selected to check the accuracy of the expression in Equation (6-5); plate 3 with an aspect ratio $\left(\frac{W}{L}\right)$ of 0.328 under 800 kPa cyclic loading conditions was selected. After 200 cycles, the deformation recorded by the MTS cyclic test frame was 10.413 mm as an average over three frequencies of loading tests. The outcome calculated using Equation (6-5) was 11.522 mm, such that relative error was 9.6%. So, although this outcome seems quite high, the magnitude of the error is relatively small, given that crushed rock tends to move under a plate loading in a somewhat random manner; it can be concluded with reasonable confidence that given a loading plate track footprint shape, the deformation may be predicted after N load repetitions of σ MPa through Equation (6-5).

6.2.3 FLAC3D Simulation

FLAC3D (Fast Lagrangian Analysis of Continua) is a numerical modeling code for static mechanical analysis of continuum in three dimensions. It utilizes a finite difference method to solve problems of materials such as stress state,

displacement and failure. Each element behaves according to a prescribed linear or nonlinear stress-strain law in response to applied forces and boundary restraints. Calculation cycles stop at a steady state solution (where maximum unbalance force is zero) has been achieved.

6.2.3.1 Assumption

There is no doubt that broken limestone is not continuous. While it does exhibit pseudo-elastic behavior after several unload-reload repetitions, which allows an elastic isotropic model in FLAC3D to be used to analyse the stress state and displacement. So the basic assumption is that material underneath plate area is homogeneous, isotropic and behaves in a pseudo-elastic manner after a few accumulated unload-reload cycles, as little irrecoverable deformation exists. Recognising that although the same material properties were used for the whole model (both for under the plate and around the plate area), only the area under plate was targeted of interest for further analysis. A more complete model would have been to use compatible properties under both the plate and surrounding the plate for all other elements.

6.2.3.2 Procedure

The procedure in FLAC3D to build a model and process the simulation are (1) generate a grid (2) define a constitutive model and assign parameter values (3) define the boundary and initial conditions and (4) compute the equilibrant state.

In the lab tests performed, both the box and plate were symmetric. A quarter test system was modeled to save calculation time. Interpreted as a “Boussinesq bulb” in the literature review, the stress was concentrated at shallow depth and reduced in magnitude with increasing depths. As a consequence, the grid in the Z axis was set as non uniform with a ratio of 1.2 broadening by depth. The walls of the box were set as fixed boundary conditions. Figure 6-14 shows the profile of the system

with fixed conditions and applied forces. The results of the simulation are shown for plate 3 under 800 kPa load. The FISH language was used to input a “user defined model” (UDM), created here for the simulation as attached in Appendix VII.

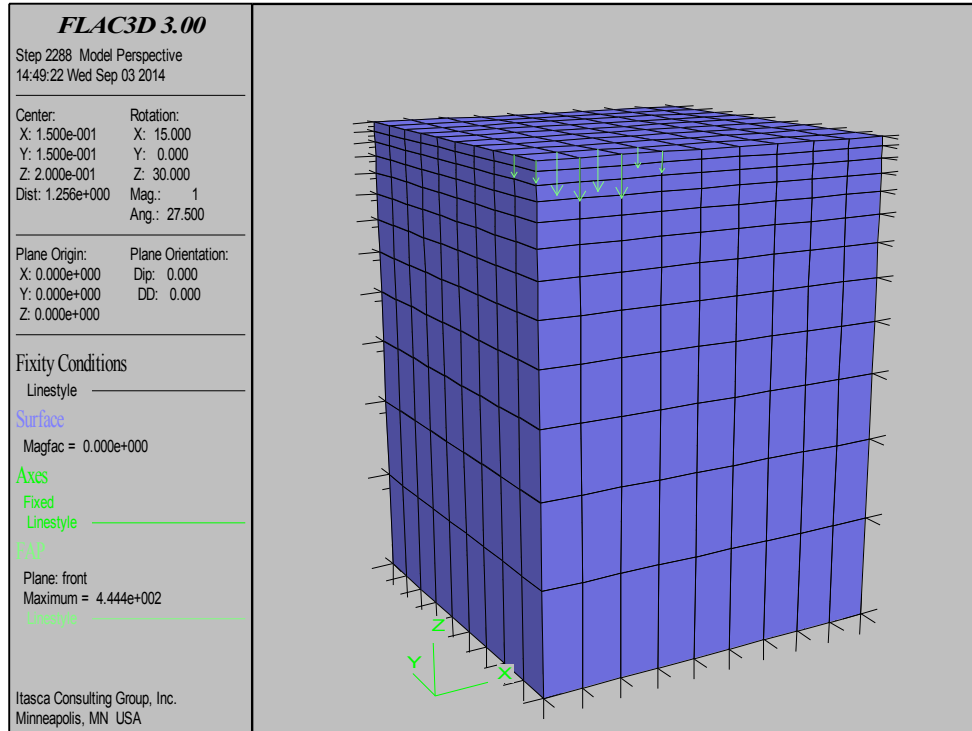


Figure 6-14 System profile in FLAC3D for plate 3 under 800 kPa

To define the pseudo-elastic model, a bulk modulus (K) and shear modulus (G) was defined. The resilient modulus (E_r) of limestone obtained from the CBR tests was 171.58 MPa. Adu-Osei, Little & Lytton (2001) suggested a Poisson’s ratio (ν) of 0.4 for unbound granular material. By using resilient modulus and Poisson ratio, a bulk modulus and shear modulus was calculated using Equations (6-6) and (6-7).

$$K = \frac{E}{3(1-2\nu)} \quad (6-6)$$

$$G = \frac{E}{2(1+\nu)} \quad (6-7)$$

Such that K is 285.97 MPa and G is 61.28 MPa. The model took 2287 steps to reach an equilibrium state. The maximum unbalanced force history is plotted in Figure 6-15.

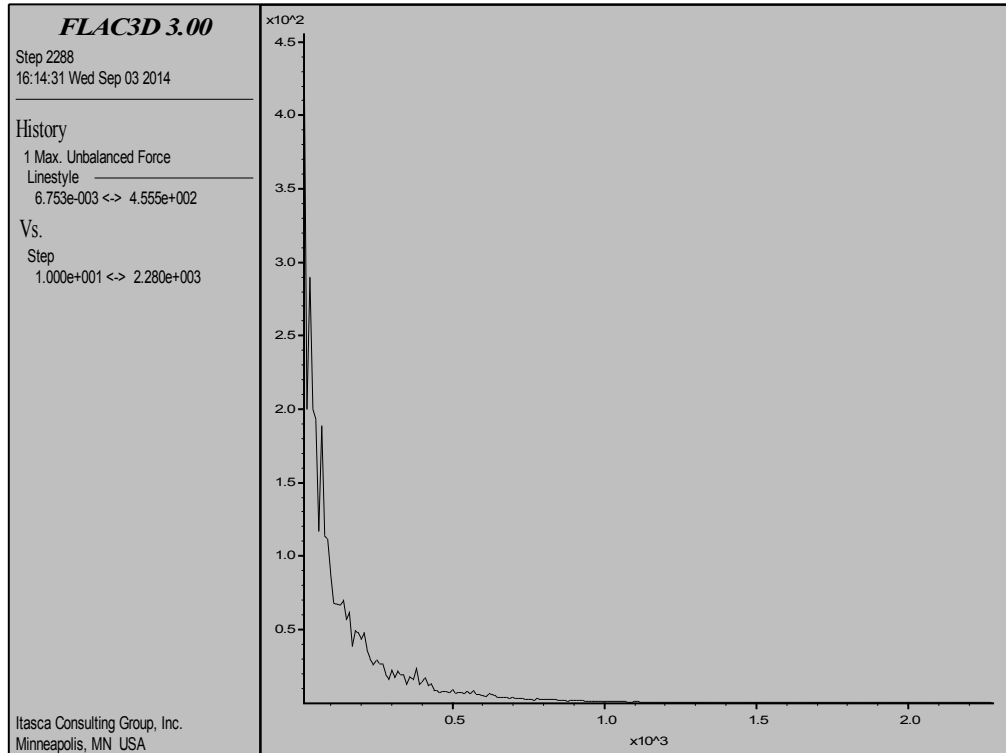


Figure 6-15 Maximum unbalance force history in FLAC3D for plate 3 under 800 kPa

6.2.3.3 Results and verification

Figure 6-16 shows the contours of vertical stress distribution under plate load. Figure 6-17 shows the contours of confining stress. Figure 6-18 shows the contours of Z-displacement. Figure 6-19 shows the contours of X-displacement magnitude and Figure 6-20 shows the contours of Y-displacement beneath the plate. These simulation results and explanations of previous speculation are summarized into five points:

1. The distribution of vertical stress satisfies “Boussinesq’s equation”, decreasing with increasing depth as is shown in Figure 6-16.
2. The confining stress contributes to material rebound deformation or elastic deformation δ_e when unloading activity present in Figure 6-17.
3. Particles at shallow depth move greater. This is the reason why the resilient stiffness under relative low loads is less stable.
4. Horizontal displacement happens primarily at the edge of the plate. Near surface, horizontal displacement is negative while with increasing depth, it becomes positive. This means that particles at shallow surface spread outwards while at deeper layers moves inwards, which is revealed in Figure 6-19 and Figure 6-20.
5. Consequently, shorter widths of plates allow less particles to flow back to complement upper interspace. This is the reason why pressure stiffness varies under different shapes of plate.

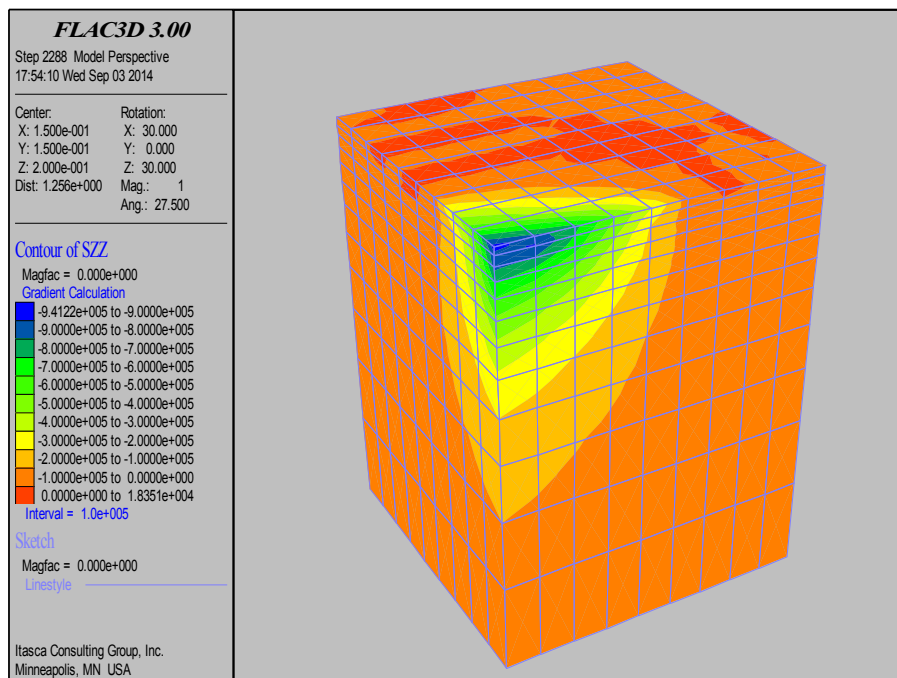


Figure 6-16 Contours of vertical stress distribution under plate load

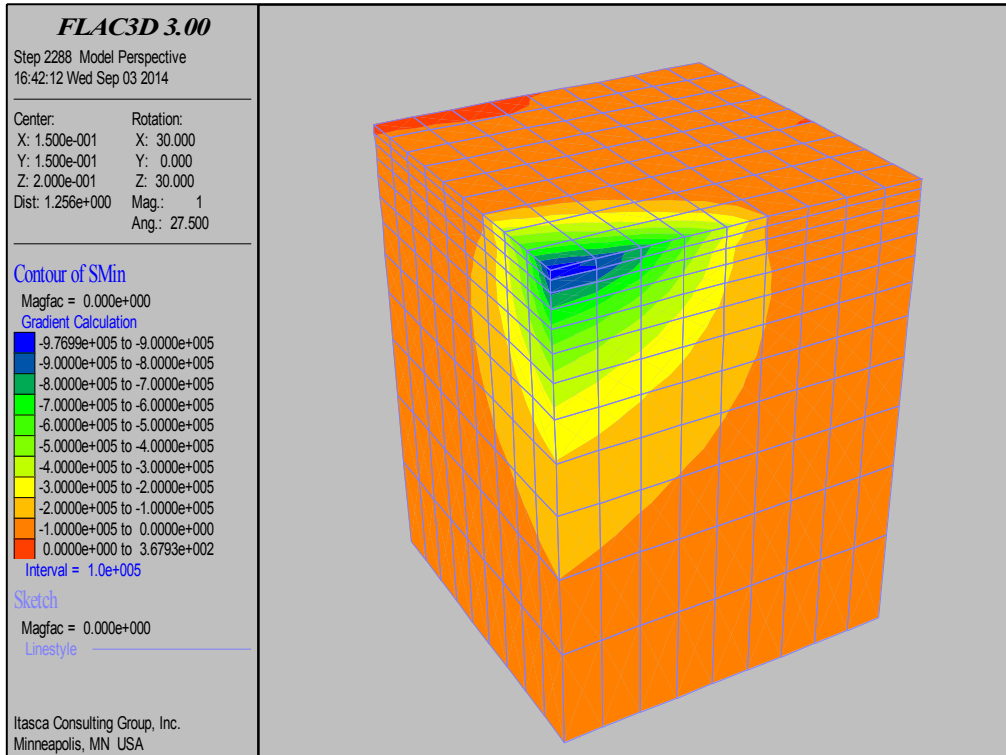


Figure 6-17 Contours of Confining stress

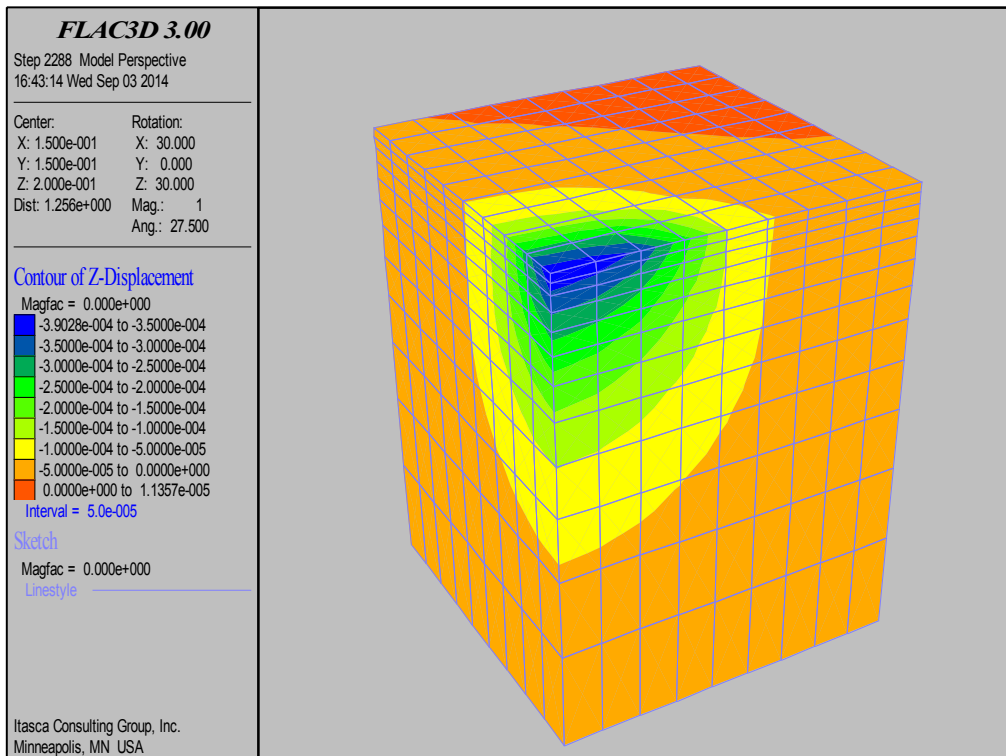


Figure 6-18 Contours of Z-displacement

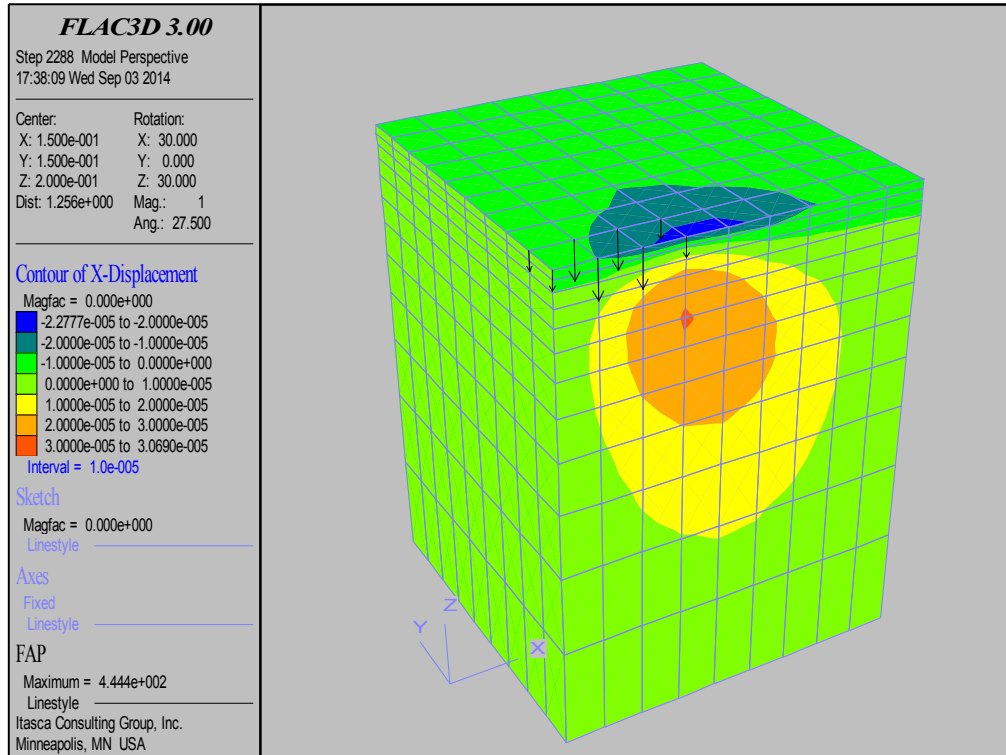


Figure 6-19 Contours of X-displacement magnitude

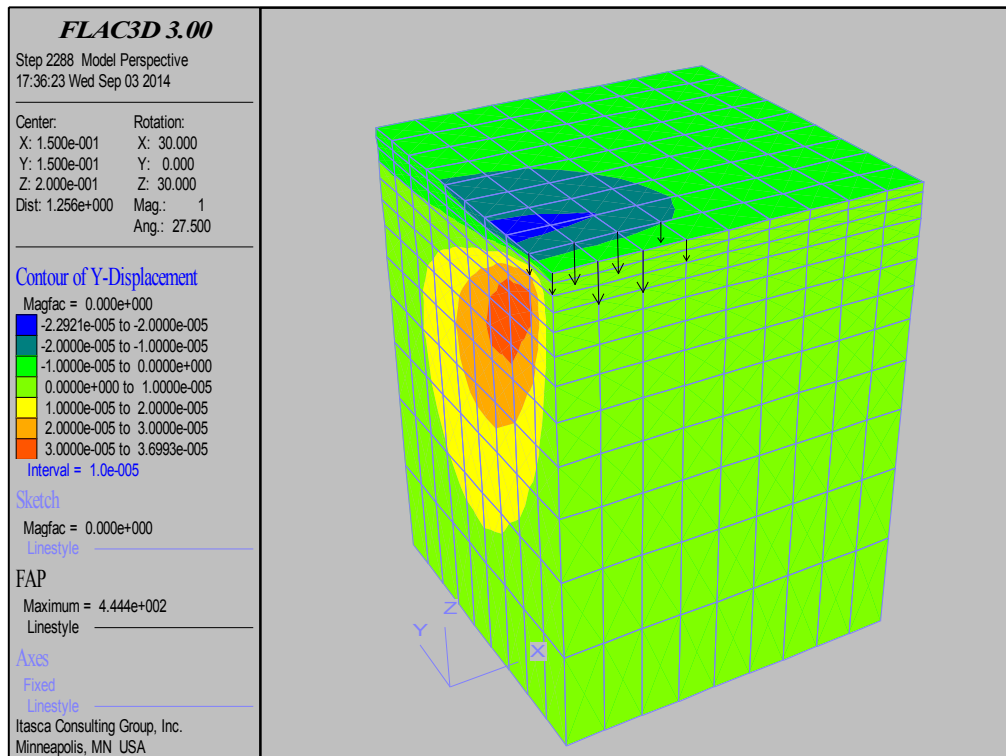


Figure 6-20 Contours of Y-displacement magnitude

6.3 Material surface conditions after loading cycles

Material surface conditions under plates after cyclic loading tests have been photographed. It is interesting to see that the sidewalls of impressions generated by sinking plate are not vertical. There is a slope resulting in a greater settlement than the plate area, as presented in Figure 6-21. This is because particles next to a plate will slip down towards the previously occupied defined plate area when a plate is unloaded.



Figure 6-21 Material surface condition after cyclic loading by strip plate

It is also observed that initially larger particles float on the top of fines while after cyclic loading they more lie in the middle (Figure 6-21). As claimed in the literature review that with increasing fines content, interlock between particles reduces and stiffness decreases. Although fines content doesn't change during cyclic loading, limestone chips are compacted and excess fines forced out which leads to a higher interlock and greater stiffness.

Individual particle breakage appears under cyclic plates, as seen in Figure 6-22.



Figure 6-22 Particle breakage after unload-reload

6.4 Application to shovel loading conditions

In chapter 3, a shovel track was separated into six parts. The load condition under six positions of a track is summarized in Table 6-4.

Table 6-4 Load condition of six track portions during one shovel digging cycle

Track index	W/L ratio	Initial loading P (kPa)	Cyclic loading (kPa)
1	0.42	100	500
2	0.42	140	260
3	0.42	170	230
4	0.42	200	200
5	0.42	300	300
6	0.42	300	300

To get the initial pressure stiffness with respect to a track portion aspect ratio of 0.42, the pressure stiffness versus width over length ratio for various plate shapes during initial loading phase in section 6.1 again is adopted. The pressure stiffness of a 0.42 ratio plate is 86 kPa/mm.

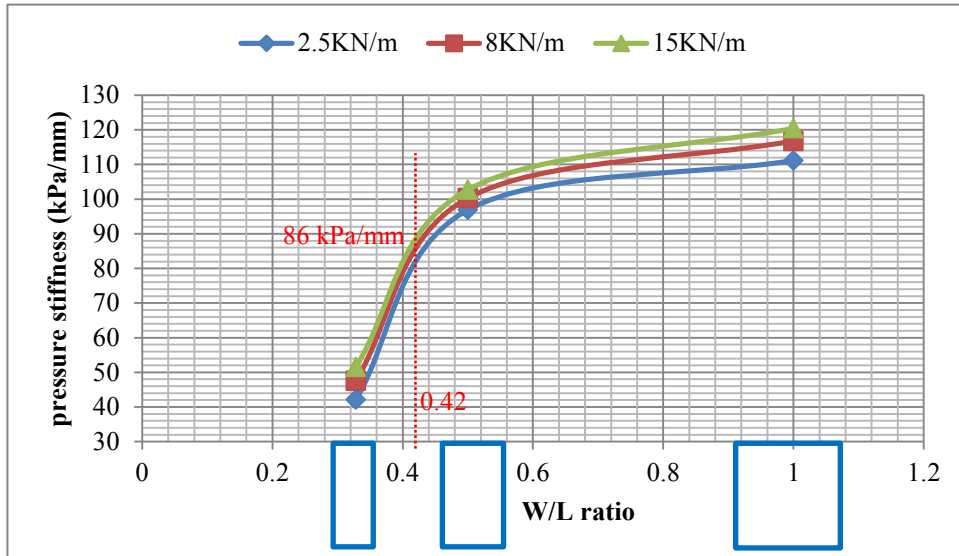


Figure 6-23 Determination of pressure stiffness during initial loading for shovel track

The total deformation is a sum of the initial deformation and cyclic deformation (Equation (6-8), (6-9)).

$$D_T = D_I + D_C \quad (6-8)$$

$$D_T = \frac{P}{k} + a \ln(N) - b \quad (6-9)$$

where D_T , D_I and D_C are total, initial and cyclic deformation respectively ($N \geq 4$).

The relevant parameters and coefficients are summarised in Table 6-5.

Table 6-5 Values of parameters and coefficients in determining total deformation of ground under a shovel track

Track index	W/L ratio	Initial stiffness k (kPa/mm)	Coefficient for cyclic phase	
			a	b
1	0.42	86	1.9114	2.6332
2	0.42	86	1.1986	1.7212
3	0.42	86	1.1095	1.6072
4	0.42	86	1.0204	1.4932
5	0.42	86	1.3174	1.8732
6	0.42	86	1.3174	1.8732

A three-dimensional graph is illustrated in Figure 6-24 to depict the ground deformation under a shovel track as number of cycles increase. As the shovel track is considered inflexible, none of the six parts can move individually. Raw data was combined to create a smooth deformation surface. Spline interpolation was used in Matlab, where the “M-file” is provided in Appendix VIII. It can be concluded that

1. The 3D figure visibly indicates that shovel face activity indeed causes shovel rocking back and forth.
2. Due to rocking motion, ground underlying the ends of the track deforms soonest
3. Deformation is accumulated and progresses from the end of track-ground contact towards the center of the footprint with increasing number of cycles.
4. Track-ground contact area deteriorates dramatically, which confirms that which Joseph (2002) proposed, “a crown” of ground will be developed beneath a shovel track.
5. As simulated in the FLA3D model, without generating confining stress, the unbound limestone easily moves laterally with excess loading. It is also

noticed in the laboratory tests that particles surrounding the plate will easily move during unloading activity. So “the crown” is less stable for broken limestone. In another word, the shovel has greater stability (i.e. it sinks rather than rocks on “the crown”) and less detrimental damage will occur to the shovel structure.

6. For a given deformation limit for shovel operating condition, the number of digging cycles before relocating shovel position could then be decided by operations.

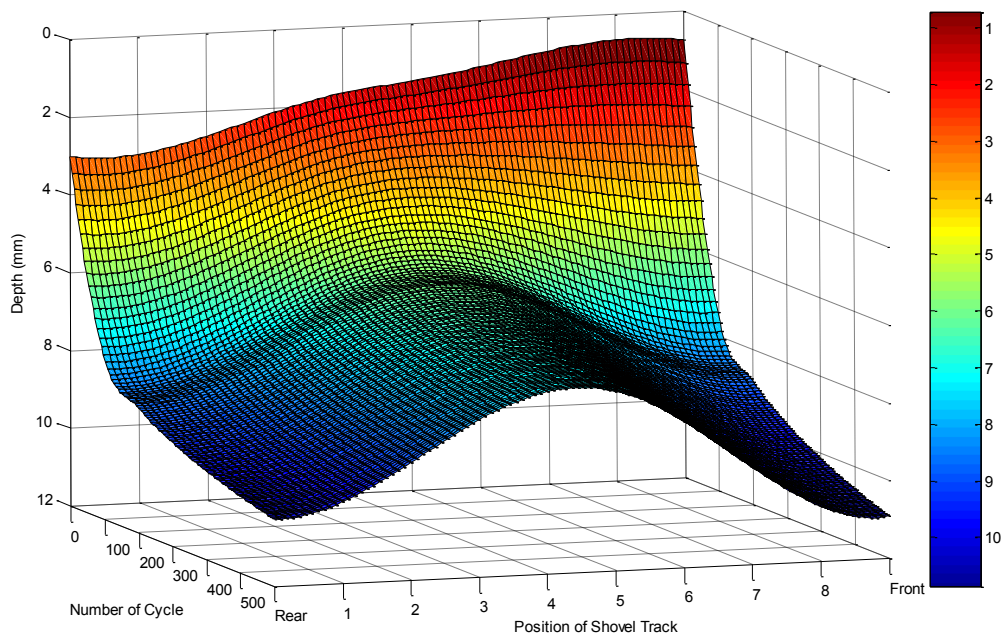


Figure 6-24 Ground deformation under shovel track with increasing number of cycles

Given that Figure 6-24 shows that less than 12 mm of maximum deformation under a shovel track ensues after 250 cycles, this suggests that a contacted pad of limestone under a shovel track would provide a good base for operational activity.

7 Conclusion

The objective of the thesis is to study the behavior of crushed limestone as a bearing ground material under an active mining shovel performing cyclic loading operation, and to predict the deformation after several duty cycles with respect to stability of a rigid piece of mining equipment and its structural life; as well as investigate the applicability of the investigated limestone crush material as a cap for a multi-layer mining surface on a weak in-situ zone such as oil sand.

7.1 Results summary

The pressure distribution underneath a shovel track during digging operations has been investigated. The most detrimental rocking motion occurs when the dipper engages full face digging and then releases from digging face. During this period, the front of shovel track experiences a maximum pressure (approximately 600 kPa) load-unload activity, while the rear of the track lifts from the ground resulting in a contact area of only two thirds of the entire track length. The front and rear region of track in six track segments essentially cycle the ground surface with amplitudes of 500 kPa and 300 kPa respectively.

In evaluating the potential strength of the limestone crush material targeted as a cap for a haul road or the mining surface, a CBR test was carried out. In a multi-layer haul road system, 2.63 m laboratory limestone with CBR value of 35.4 % can be built on a lower CBR value material (i.e. 15 % is strong enough) to provide a sustainable and less costly road construction.

Cyclic plate load tests were conducted in the lab at different loads and frequencies with three shaped plates to mimic shovel loading conditions on ground material. Performance of the limestone crush material was analysed.

In an initial loading phase, the pressure stiffness of the limestone was affected by the shape of the plate. The larger the aspect ratio of the plate, the higher stiffness the material displayed.

Under cyclic loading conditions, a global stiffness increased with number of cycles before converging to a constant value, which is a function of the cyclic load. The resilient stiffness (k_r) regardless of plate shape was established as 0.8 MPa/mm which is consistent with the slope of the stress-deformation curve from the CBR test. Therefore, CBR can be used to estimate a resilient stiffness of broken material. It is also observed that regardless of the global stiffness or resilient stiffness, it is independent of cyclic frequency between 0.016 Hz and 0.066 Hz.

The total deformation δ_T generated within one single cycle (or pseudo-elastic deformation (δ_{ps})) consists of elastic and plastic components. Plastic deformation reduced to less than 0.05 mm after 100 cycles and the elastic portion remained effectively unchanged.

There is a good correlation between the total deformation (D_c) generated by unload-reload and number of cycles (N), with respect to plate shape ($\frac{W}{L}$) and cyclic load (σ) shown to be expressed as

$$D_c = \left\{ 0.88 - 1.08\left(\frac{W}{L}\right) + 2.97(\sigma) \right\} \cdot \ln(N) + 1.04\left(\frac{W}{L}\right) - 3.8(\sigma) - 1.17$$

A simulation of the static plate loading test in FLAC3D based on assumptions of a homogeneous isotropic and pseudo-elastic material property for laboratory

limestone, after sufficient load repetitions are applied, indicated the deformation and stress distribution in a material volume and particle flow rules. It showed that particles at shallow footing move outwards while deep-seated particles flow towards the center of a void.

For actual shovel loading conditions and material properties under cyclic loading, ground deformation under a shovel track after several dig duty cycles was predicted. A three dimensional graph of ground deformation along a shovel track with increasing number of cycles was plotted. Conclusions were made that the deformation is accumulated and progresses from the end of track-ground contact towards the center of the track underfoot, which leads to “a crown” shape ground developing. For the crushed limestone investigated, “the crown” was shown to collapse rather than be maintained and as such less detrimental damage could prospectively be applied to a shovel frame. In addition, if a specific deformation limit is assigned to a shovel working zone, the number of cycles on a given limestone crush pad before shovel relocation may be predicted.

7.2 Contributions to knowledge and industry

The expression $D_c = \left\{ 0.88 - 1.08\left(\frac{W}{L}\right) + 2.97(\sigma) \right\} \cdot \ln(N) + 1.04\left(\frac{W}{L}\right) - 3.8(\sigma) - 1.17$

allowed an estimation of limestone crush material deformation under cyclic loading by shovel tracks. The parameters may then be evaluated for other material types that could be used for under-track pad material. The work showed that the CBR test may also be used to estimate cyclic plate load test performance via common pressure stiffness, which in the case of limestone, was 0.8 MPa/mm.

The work in this thesis permits mining operators to better gauge the stability of pad surfaces for shovels, in pit crushers and other tracked equipment. This leads to improved machine performance on more stable ground and less maintenance, both of which generate lower operational cost.

8 Future work

The material used in the research was discrete and dry. In the field, precipitation is inevitable which will change the water content of the material. So the influence of water content on the properties of crushed limestone need to be considered in the future.

Actually the behavior of broken limestone is very complicated. It exhibits both elastic and plastic properties simultaneously. The software (FLAC 3D) used to indicate particle flow considered homogeneous and continuous material simulation. However the limestone crush is discrete and particle sizes range from very small fines to large limestone chips. FLAC 3D was only applied to the cyclic loading phase after the material had experienced several unload-reload repetitions and had reached a relative stable state. For a more widely applicable simulation, discrete element methods (DEM) need to be considered, which can better model the characteristics of the material particles and give more reliable simulation results. DEM Software like PFC is considered worth investigating for the application in the future.

References

1. Adu-Osei, A., Little, D.N. & Lytton, R.L. (2001). Structural characteristics of unbound aggregate bases to meet AASHTO 2002 design requirements: interim report (No. ICAR-502-1).
2. Agarwal, J. (2010). Cyclic load-deformation performance of oil sand. (M.Sc., University of Alberta (Canada)).
3. Sharif-Abadi, A.D. & Joseph, T.G. (2010). Oil sand deformation under cyclic loading of ultra-class mobile mining equipment. *Journal of Terramechanics*, 47(2), 75-85.
4. ASTM (2007) D1883: Standard test method for CBR (california bearing ratio) of laboratory-compacted soils. West Conshohocken, PA, USA. ASTM International.
5. ASTM (2012) D698: Standard test methods for laboratory compaction characteristics of soil Using Standard effort (12 400 ft-lbf/ft³ (600 KN-m/m³)). West Conshohocken, PA, USA. ASTM International.
6. Barksdale, R.D. (1972). Laboratory evaluation of rutting in base course materials. Paper presented at the Third International Conference on the Structural Design of Asphalt Pavements, Grosvenor House, Park Lane, London, England, Sept. 11-15, 1972.
7. Boussinesq, J. (1885). Application des potentiels à l'étude de l'équilibre et du mouvement des solides élastiques: principalement au calcul des déformations et des pressions que produisent, dans ces solides, des efforts quelconques exercés sur une petite partie de leur surface ou de leur intérieur: Mémoire suivi de notes étendues sur divers points de physique, mathématique et d'analyse / Paris: Gauthier-Villars.

8. Brown, S. (1996). Soil mechanics in pavement engineering. *Geotechnique*, 46(3), 383-426.
9. Sharif-Abadi, A.D. (2006). Cyclic performance of soft ground. (Ph.D., University of Alberta (Canada)).
10. Earl, R. & Alexandrou, A. (2001). Deformation processes below a plate sinkage test on sandy loam soil: Experimental approach. *Journal of Terramechanics*, 38(3), 153-162.
11. Farrar, M.J., & Turner, J.P. (1991). Resilient Modulus of Wyoming Sub-grade Soils (No. MPC Report No. 91-1).
12. Florin, V.A. (1959). Fundamentals of soil mechanics. Stroyizdat, Mos-Cow/Leningrad (in Russian).
13. Gonzalez, A., Saleh, M., Ali, A. & Gribble, M. (2007). Nonlinear finite element modeling of unbound granular materials. Paper presented at the Advanced Characterisation of Pavement and Soil Engineering Materials-Proceedings of the International Conference on Advanced Characterisation of Pavement and Soil Engineering Materials, 1 523-532.
14. Gudishala, R. (2004). Development of Resilient Modulus Prediction Models for Base and Subgrade Pavement Layers from in Situ Devices Test Results (Doctoral dissertation, Louisiana State University).
15. Hardin, B. O. & Drnevich, V. P. (1972). Shear modulus and damping in soils. *Journal of the Soil Mechanics and Foundations Division*, 98(7), 667-692.
16. Heukelom, W. & Klomp, A. (1962). Dynamic testing as a means of controlling pavements during and after construction. Paper presented at the International Conference on the Structural Design of Asphalt Pavements, 203(1)

17. Hicks, R. G. & Monismith, C. L. (1971). Factors influencing the resilient response of granular materials. Highway Research Record.
18. Huurman, M. (1997). Permanent deformation in concrete block pavements. Delft University of Technology, Delft, the Netherlands.
19. Ishihara, K. (1996). Soil behaviour in earthquake geotechnics. Oxford Science Publication.
20. Jian, Z. & Xiaonan, G. (2000). Study on strain softening in saturated soft clay under cyclic loading. China Civil Engineering Journal, 2000, 33 (5): 75 - 82. (in Chinese)
21. Joseph, T.G. (2001). OsEIP year end progress report. James Progitin International Ltd. 16pages, Syncrude Canada Ltd.
22. Joseph, T.G. (2002). OsEIP: The oil sands-equipment interactions program. CIM Bulletin, 95(1064), 58-61.
23. Joseph, T.G. (2003). Large mobile mining equipment operating on soft ground. Paper presented at the Proceedings of the 18th International Mining Congress and Exhibition of Turkey–IMCET, 10-13.
24. Joseph, T.G., Sharif-Abadi, A., & Shi, N. (2003). A broken material approach to modeling oil sand under dynamic load. Paper presented at the Calgary, CAMI Conference.
25. Joseph, T.G., & Barron, K. (2003). The post-failure characteristics of rock. CIM Bulletin, 96(1070), 66-74.
26. Joseph, T. G., & Hansen, G. W. (2002). Oil sands reaction to cable shovel motion. CIM Bulletin, 95(1064), 62-64.
27. Kaufman, W.W., & Ault, J.C. (1978). Design of surface mine haulage roads: A manual. Department of the Interior, Bureau of Mines.

28. Kondner, R.L. (1963). A hyperbolic stress-strain formulation for sands. Northwestern University.
29. LeKarp, F., Isacsson, U. & Dawson, A. (2000). State of the art. I: Resilient response of unbound aggregates. *Journal of Transportation Engineering*, 126(1), 66-75.
30. Li, D. & Selig, E.T. (1994). Resilient modulus for fine-grained subgrade soils. *Journal of Geotechnical Engineering*, 120(6), 939-957.
31. Lin, Z. (2014). Abrasive wear of shovel teeth in oil sand (Unpublished M.Eng.thesis). University of Alberta.
32. Luzia, R., Picado-Santos, L. & Pereira, P. (2008). Mechanical behaviour of two crushed materials used in Portuguese UGL.
33. Masing, G. (1926). Eigenspannungen und verfestigung beim messing. Paper presented at the Proceedings of the 2nd International Congress of Applied Mechanics, 100 332-335.
34. Matasovic, N. & Vucetic, M. (1993). Cyclic characterization of liquefiable sands. *Journal of Geotechnical Engineering*, 119(11), 1805-1822.
35. Morgan, J., Tucker, J. & McInnes, D. (1994). A mechanistic design approach for unsealed mine haul roads. Paper presented at the 17th Arrb conference, gold coast, Queensland, 15-19 August 1994; proceedings; volume 17, part 2.
36. Nakagawa, K. & Soga, K. (1995). Nonlinear cyclic stress-strain relations of soils. Paper presented at the Third International Conference on Recent Advances in Geotechnical Earthquake Engineering and Soil Dynamics (1981: April 2-7; St. Louis, Missouri).

37. Newmark, N.M. (1935). Simplified computation of vertical pressures in elastic foundations. University of Illinois--Engineering Experiment Station--Circular, v 33(n 24, 4), 19p.
38. Ni, S., Siddharthan, R.V. & Anderson, J. G. (1997). Characteristics of nonlinear response of deep saturated soil deposits. Bulletin of the Seismological Society of America, 87(2), 342-355.
39. Perloff, W.H. & Baron, W. (1976). Soil mechanics. Principles and Applications. The Ronald Press Company, New York.
40. Qian, Y., Han, J., Pokharel, S. K. & Parsons, R.L. (2011). Determination of resilient modulus of subgrade using cyclic plate loading tests. Paper presented at the Geotechnical Special Publication, (211 GSP) 4743-4751.
41. Ramberg, W. & Osgood, W.R. (1943). Description of stress-strain curves by three parameters. National advisory committee for aeronautics.
42. Sawicki, A. & Swidzinski, W. (1995). Cyclic compaction of soils, grains and powders. Powder Technology, 85(2), 97-104.
43. Schleicher, F. (1926). Kreisplatten auf elastischer unterlage; theorie zentralsymmetrisch belasteter kreisplatten und kreisringplatten auf elastisch nachgiebiger unterlage, mit anwendungen der theorie auf die berechnung von kreisplattenfundamenten und die einspannung in elastische medien Berlin, J. Springer.
44. Shi, N. (2007). A new approach to improving cable shovel dipper design for cutting soft rock and soils. (Ph.D., University of Alberta (Canada)).
45. Sweere, G.T. (1990). Unbound granular bases for roads (Doctoral dissertation, Technische Universiteit Delft).
46. Thom, N. & Brown, S. (1988). The effect of grading and density on the mechanical properties of a crushed dolomitic limestone. Paper presented at

- the Australian Road Research Board (ARRB) Conference, 14th, 1988, Canberra, 14(7).
47. Thompson, R.J. & Visser, A. (1996). Towards a mechanistic structural design method for surface mine haul roads: Technical paper. *Journal of the South African Institution of Civil Engineering* 38(2), 13-20.
 48. Thompson, R. J. (2011). Higher payloads and autonomous operations need roads designed for structural strength. *WOMP Building Better Haul Roads*, vol 05.
 49. Thompson, R.J. & Visser, A. T. (1997). An introduction to the integrated design of surface mine haul roads. *International Journal of Surface Mining, Reclamation and Environment*, 11(3), 115-120.
 50. Transportation Officials (1993). *AASHTO guide for design of pavement structures*, 1993 AASHTO.
 51. Trombley, N. (2001). Vital information management system. Co-Op Work Term Presentation at Syncrude Canada Ltd. 24 Slides.
 52. Uzan, J. Characterization of Granular Material. In *Transportation Research Records* 1022. 1985. Washington DC: Transportation Research Board.
 53. Wohlgemuth, P. (1997). Structural fatigue cracking failure trends (M.Eng.thesis, University of Alberta). 42 pages.
 54. Yohannes, B., Hill, K. & Khazanovich, L. (2014). Mechanistic modeling of unbound granular materials. *International Journal of Pavement Engineering*, v15 (No. 7), 584-598.

Appendix I-Geometric approach for shovel hoist and crowd system equilibrium

Calculation of L_{hoist}

In an attempt to illustrate a geometric relationship, critical points on a shovel dipper system are marked (see Figure 1). The saddle block center is represented by O. The furthest hinge on the dipper is notated as A. P is center of the sheave (pulley). A_4 is the tangency point of the sheave through A. OA_3 is the extended crowd length. Essential angles and other auxiliary points are indicated in Figure 1.

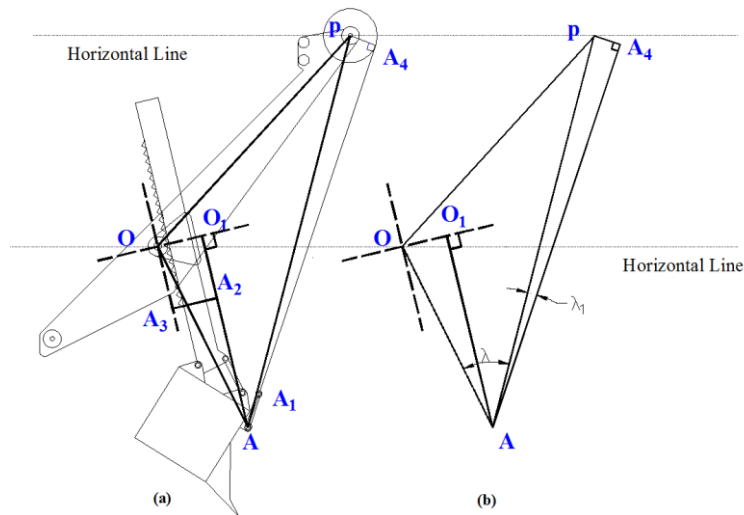


Figure 1 Geometric schematic of shovel hoist system (after Lin, 2014)

The hoist length, L_{hoist} can be determined via Equation (0-1), (0-2), (0-3) and (0-4).

$$L_{hoist} = OA \cdot \sin(\lambda + \lambda_1) \quad (0-1)$$

$$OA = \sqrt{(O_1A_2 + A_2A)^2 + OO_1^2} \quad (0-2)$$

$$\lambda = \arccos\left(\frac{OA^2 + AP^2 - OP^2}{2OA \cdot AP}\right) \quad (0-3)$$

$$\lambda_1 = \arctan\left(\frac{PA_4}{AA_1 + A_1A_4}\right) \quad (0-4)$$

$$AP = \sqrt{PA_4^2 + (AA_1 + A_1A_4)^2} \quad (0-5)$$

Considering the P&H 4100C BOSS mining shovel, its dimensions and angles are fixed, as provided in Table 1.

Table 1 P&H 4100C BOSS mining shovel specification (1)

Sign	Description	Dimension (m)
OO ₁	Distance between saddle block and the line through hinge A and parallel to crowd handle.	1.78
A ₂ A	The rest distance of O ₁ A except crowd extension	7.11
PA ₄	Radius of sheave	1.11
AA ₁	Distance between two hinges	2.22
OP	Length of boom beyond saddle block	15.4
O ₁ A ₂	Equal to OA ₃ (length of crowd extension)	real time data
A ₁ A ₄	Length of hoist rope	real time data

Calculation of $m_{handle}g$ and L_{handle}

Assuming the crowd as a uniform weight by geometric shape, then $m_{handle}g$ (weight of extended handle) can be calculated using Equation (0-6)

$$m_{handle}g = 380.79 \times \frac{L_{handle}}{12.44} \quad (0-6)$$

where 380.79 (kN) is the total weight of dipper handle, 12.44 (m) is the entire handle length. A schematic of the hoist and crowd system is illustrated in Figure 2. H is the centroid of the extended dipper handle. A_5 is the hinge nearest to the handle on the dipper.

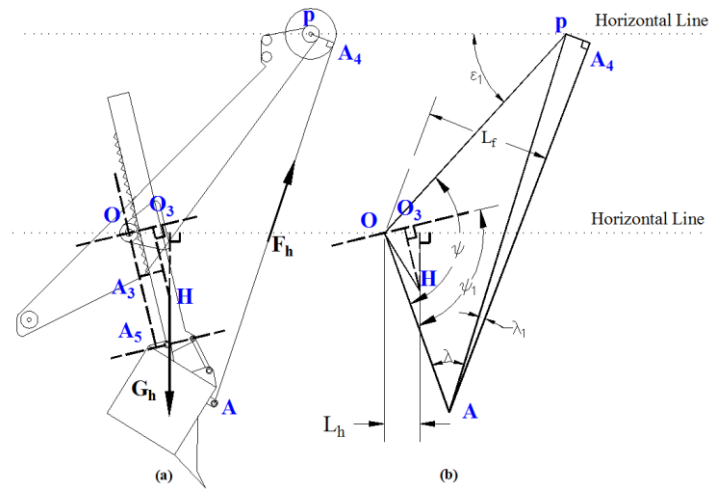


Figure 2 Geometric schematic of shovel boom system (after Lin, 2014)

The geometric relationships are provided by Equations from (0-7) to (0-14).

Dimensions of specific length and angle are listed in Table 2.

Table 2 P&H 4100C BOSS mining shovel specification (2)

Sign	Description	Dimension (m)
A_3A_5	The rest distance of OA_5 except crowd extension	2.67
OO_3	The distance between saddle block to O_3H	0.89
ε_1	Beam angle	42°

$$L_{handle} = OA_3 + A_3A_5 \quad (0-7)$$

$$OH = \sqrt{(OO_3)^2 + (O_3H)^2} \quad (0-8)$$

$$O_3H = \frac{L_{handle}}{2} \quad (0-9)$$

$$\angle xOH = \angle O_3OH - \alpha \quad (0-10)$$

$$\angle O_3OH = \arctan\left(\frac{O_3H}{OO_3}\right) \quad (0-11)$$

$$\alpha = \psi_1 - \beta = \psi_1 - (\psi - \varepsilon_1) \quad (0-12)$$

$$\psi = \arccos \frac{OA^2 + OP^2 - AP^2}{2OA \cdot OP} \quad (0-13)$$

$$\psi_1 = \arctan \frac{O_1A_2 + A_2A}{OO_1} \quad (0-14)$$

Appendix II-Geometric approach for the shovel dipper and digging-face system equilibrium

Calculation of L_{dipper}

Figure 3 is a geometric schematic of the shovel dipper and digging-face with auxiliary points and angles. The centroid of the dipper is B.

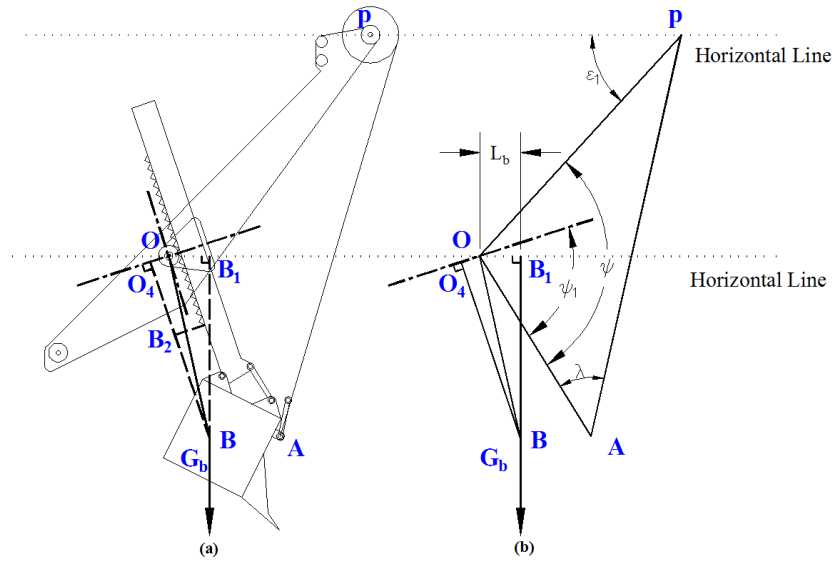


Figure 3 Geometric schematic of shovel bucket and digging-face system (after Lin, 2014)

Equations (0-1), (0-2), (0-3) demonstrate the geometric relationships to get L_{dipper} .

$$L_{dipper} = OB \cdot \cos \angle B_1OB \quad (0-1)$$

$$OB = \sqrt{(O_4B_2 + B_2B)^2 + OO_4^2} \quad (0-2)$$

$$\angle B_1OB = \pi - \alpha - \arctan\left(\frac{O_4B_2 + B_2B}{OO_4}\right) \quad (0-3)$$

where O_4B_2 is the crowd extension from the on-board system. BB_2 and OO_4 are fixed values of 6.22 m and 0.35 m respectively for the P&H 4100C BOSS mining shovel and α is the same angle as depicted in Appendix I.

Appendix III-Matlab code for Figure 3-11

```
[X,Y]=meshgrid(-6.5:0.1:6.5,4.5:-0.1:-4.5)
Ptri=xlsread('shovel.xls','track stress distribution','B3:B142')
Ptra=xlsread('shovel.xls','track stress distribution','C3:D142')
X1=xlsread('shovel.xls','track stress distribution','I3:I142')
u=1
for i=[1,20,40,61,83,106,126,139]
    if X1(i)==0
        z=linspace(Ptra(i,2),Ptra(i,1),91)
        zz(:,i)=z'
    else
        z(1:X1(i))=linspace(Ptri(i),0,X1(i))
        z((X1(i)+1):91)=zeros(1,91-X1(i))
        zz(:,i)=z'
    end
    [Z1,Z]=meshgrid(1:1:36,zz(:,i))
    Z(:,37:1:95)=meshgrid(zeros(1,59),1:1:91)
    [Z2,Z(:,96:1:131)]=meshgrid(1:1:36,zz(:,i))
    subplot(2,4,u),surf(X,Y,-Z)
    set(gca,'xtick',[-6.5 6.5],'ytick',[-4.5 4.5])
    if u==1
        title('tuck')
    end
    if u==2
        title('half-facce digging1')
    end
end
```

```
if u==3
title('half-face digging2')
end
if u==4
title('full-face digging')
end
if u==5
title('hard-face digging1')
end
if u==6
title('hard-face digging2')
end
if u==7
title('face release')
end
if u==8
title('carry high')
end
colormap('hot')
shading interp
view(0,90)
u=u+1
end
```

Appendix IV-Matlab code for Figure 3-13

```
X1=xlsread('shovel.xls','track stress distribution','I3:I142')
Ptri=xlsread('shovel.xls','track stress distribution','B3:B142')
Ptra=xlsread('shovel.xls','track stress distribution','C3:D142')
for i=1:size(Ptra,1)
    P1(i,:)=linspace(Ptra(i,2),Ptra(i,1),91)
end
for i=1:size(Ptri)
    P2(i,(1:X1(i)))=linspace(Ptri(i),0,X1(i))
    P2(i,((X1(i)+1):91))=zeros(1,(91-X1(i)))
end
P=P1+P2
t=xlsread('shovel.xls','track stress distribution','A3:A142')
PP(:,1)=sum(P(:,1:16),2)
PP(:,2)=sum(P(:,17:31),2)
PP(:,3)=sum(P(:,32:46),2)
PP(:,4)=sum(P(:,47:61),2)
PP(:,5)=sum(P(:,62:76),2)
PP(:,6)=sum(P(:,77:91),2)
PPP=[PP(:,1)/15,PP(:,2)/14,PP(:,3)/14,PP(:,4)/14,PP(:,5)/14,PP(:,6)/14]
u=1
for i=1:size(PPP,2)
    plot(t,PPP(:,i))
    xlabel('time/s')
    ylabel('pressure/KPa')
    title('portion pressure')
```

```
axis([10 30 0 700])
```

```
figure
```

```
end
```

***Appendix V-Matlab code for data screening in cyclic
plate load tests***

```
X=data(:,1);Y=data(:,2);Z=data(:,3)           % data is database that MTS
exports
% X is Deformation Y is Force Z is time;
IndMax=find(diff(sign(diff(X)))<0)+1;
peak=data(IndMax,:);
IndMax1=find(diff(sign(diff(peak(:,1))))<0)+1;
peak1=peak(IndMax1,:);
IndMax2=find(diff(sign(diff(peak1(:,1))))<0)+1;
peak2=peak1(IndMax2,:);
IndMin=find(diff(sign(diff(X)))>0)+1;
bottom=data(IndMin,:);
IndMin1=find(diff(sign(diff(bottom(:,1))))>0)+1;
bottom1=bottom(IndMin1,:);
IndMin2=find(diff(sign(diff(bottom1(:,1))))>0)+1;
bottom2=bottom1(IndMin2,:);
```

***Appendix VI-Estimation of coefficients in Equation (6-2)
and confidence intervals in Matlab***

$$X = \begin{pmatrix} 1 & 0.328 & 0.8 \\ 1 & 0.328 & 0.6 \\ 1 & 0.328 & 0.4 \\ 1 & 0.328 & 0.2 \\ 1 & 0.5 & 0.8 \\ 1 & 0.5 & 0.6 \\ 1 & 0.5 & 0.4 \\ 1 & 0.5 & 0.2 \\ 1 & 1 & 0.8 \\ 1 & 1 & 0.6 \\ 1 & 1 & 0.4 \\ 1 & 1 & 0.2 \end{pmatrix} \quad A = \begin{pmatrix} 2.7864 \\ 2.596 \\ 2.3153 \\ 1.0812 \\ 2.6183 \\ 1.7366 \\ 1.081 \\ 0.8308 \\ 2.3032 \\ 1.7076 \\ 0.9471 \\ 0.4172 \end{pmatrix} \quad B = \begin{pmatrix} 3.6777 \\ 3.4114 \\ 3.1996 \\ 1.8425 \\ 3.5598 \\ 2.5216 \\ 1.5589 \\ 0.9637 \\ 2.9428 \\ 3.2186 \\ 1.7323 \\ 0.6516 \end{pmatrix}$$

`a=regress(A,X)`

`[a,aint,r,rint,stats]=regress(A,X,0.05)`

`b=regress(B,X)`

`[b,bint,r,rint,stats]=regress(B,X,0.05)`

$$a = \begin{pmatrix} 0.8751 \\ -1.082 \\ 2.972 \end{pmatrix} \quad b = \begin{pmatrix} 1.1722 \\ -1.0414 \\ 3.8047 \end{pmatrix}$$

95% confidence intervals for the coefficient estimates of a

$$\begin{pmatrix} 0.21801 & 1.5322 \\ -1.7914 & -0.37317 \\ 2.0683 & 3.876 \end{pmatrix} \text{ Correlation coefficient is } 0.88.$$

95% confidence intervals for the coefficient estimates of b

$$\begin{pmatrix} 0.066 & 2.278 \\ -2.234 & 0.152 \\ 2.284 & 5.326 \end{pmatrix} \text{ Correlation coefficient is } 0.80.$$

Appendix VII-FLAC 3D language for simulation

```
gen zone brick p0 0,0,0 p1 0.3,0,0 p2 0,0.3,0 p3 0,0,0.4 size 9,9,12 ratio 1,1,0.8
plot surf
model elastic
prop bulk=2.8597e8 shear=6.128e7
fix x range x -0.01 0.01
fix x range x 0.29 0.31
fix y range y -0.01 0.01
fix y range y 0.29 0.31
fix z range z -0.01 0.01
apply szz=-800000 range z 0.39 0.41 x -0.01 0.1026 y -0.01 0.0333375
hist unbal
hist zone smin 0,0,0.38
hist zone smin 0,0,0.35
hist zone smin 0,0,0.3
hist zone smin 0,0,0.2
solve
```

Appendix VIII-Matlab code for Figure 6-24

```
x=[0.75,2.25,3.75,5.25,6.75,8.25]
xx=linspace(0,9,91)
y=linspace(0,600,7)
[Y,X]=meshgrid(y,xx)
for i=1:size(y,2)
    z=[-(300/86+1.32*log(y(i)+3)-1.87)
    -((300/86+1.32*log(y(i)+3)-1.87)+(200/86+1.32*log(y(i)+3)-1.87))/2
    -((200/86+1.32*log(y(i)+3)-1.87)+(200/86+1.02*log(y(i)+3)-1.49))/2
    -((200/86+1.02*log(y(i)+3)-1.49)+(150/86+1.17*log(y(i)+3)-1.68))/2
    -((150/86+1.17*log(y(i)+3)-1.68)+(100/86+1.91*log(y(i)+3)-2.63))/2
    -(100/86+1.91*log(y(i)+3)-2.63)]
    pp=spline(x,z)
    Z(:,i)=ppval(pp,xx)
end
surf(Y,X,Z)
xi=linspace(0,9,100)
yi=linspace(0,600,100)
[YI,XI]=meshgrid(yi,xi)
ZI=interp2(Y,X,Z,YI,XI,'cubic')
surf(YI,XI,ZI)
xlabel('Number of Cycle'); ylabel('Position of Shovel Track'); zlabel('Depth
(mm)')
h = colorbar
set(h,'YTickLabel',{10,9,8,7,6,5,4,3,2,1})
set(gca,'xtick',[0,100,200,300,400,500])
```

```
set(gca,'yticklabel',{'Rear',1,2,3,4,5,6,7,8,'Front'})
```

```
set(gca,'zticklabel',{12,10,8,6,4,2,0})
```